NI

NASA Contractor Report 165846

EXPERIMENTAL STUDY OF DELTA WING LEADING-EDGE DEVICES FOR DRAG REDUCTION AT HIGH LIFT

Thomas D. Johnson, Jr. and Dhanvada M. Rao

OLD DOMINION UNIVERSITY
Norfolk, Virginia 23508

NASA Grant NGR 47-003-052
February 1982

National Aeronautics and
Space Administration

Langley Research Center
Hampton, Virginia 23665

EXPERIMENTAL STUDY OF DELTA WING LEADING-EDGE DEVICES FOR DRAG REDUCTION AT HIGH LIFT

Thomas D. Johnson, Jr. and Dhanvada M. Rao
Old Dominion University

SUMMARY

Future fighter aircraft requirements specify efficient supersonic cruise and high-g maneuverability at high lift. The slender delta wing meets the first requirement but has large lift-induced drag increments at high lift. One method to alleviate the drag is to control the flow at the wing leading edge (LE) by means of small LE devices, so as to maintain locally attached flow to higher angles of attack and thus increase the level of aerodynamic thrust.

The devices selected for evaluation were the fence, slot, pylon-type vortex generator (VG), and sharp leading-edge extension (SLEE). These devices were tested on a 60° flatplate delta (with blunt LE) in the Langley Research Center (NASA) 7- by 10-Foot High-Speed Tunnel at low speed and to angles of attack of 28°. Balance and static pressure measurements were taken.

The results indicate that all the devices had significant drag reduction capability and improved longitudinal stability while a slight loss of lift and increased cruise drag occurred.

TABLE OF CONTENTS

Page

LIST OF SYMBOLS

AF	balance axial force, uncorrected
b	wing span
BL	boundary layer
C_A	axial force coefficient, Axial force/$q_\infty S$
C_{A_o}	axial force coefficient at $\alpha = 0^o$
C_D	drag coefficient, Drag force/$q_\infty S$
C_{D_o}	drag coefficient at $\alpha = 0^o$
CG	center of gravity
C_L	lift coefficient, Lift force/$q_\infty S$
C_m	pitching-moment coefficient, Pitching moment/$q_\infty bS$
C_N	normal-force coefficient, Normal force/$q_\infty S$
C_p	pressure coefficient, $p - p_\infty/q_\infty$
C_S	suction-force coefficient, Suction force/$q_\infty S$
C_T	aerodynamic thrust force coefficient, $-(C_A - C_{A_o})$
$C_{T,LCL\ PRESS}$	local thrust force coefficient, pressure derived
$C_{T,TOT\ PRESS}$	total thrust force coefficient, pressure derived
F	fence
L/D	lift-to-drag ratio
LE	leading edge
L-SLEE	low sharp leading-edge extension
M-SLEE	mid sharp leading-edge extension
PD	percent drag reduction, $(C_D - C_{D,BW}/C_{D,BW})100$

q_∞	free-stream dynamic pressure
R_{LER}	Reynolds number based on wing LE radius
S	wing reference area
s	suction parameter, ζ/ζ_o
SLEE	sharp leading-edge extension
U_∞	free-stream velocity
VG	pylon-type vortex generator
x	chordwise distance of static pressure orifice from wing LE
α	angle of attack, deg
α_D	α for which onset of LE separation occurs
$\Delta C_{A,BAL}$	$C_A - C_{A_o}$
ζ	thrust parameter, $C_T \cos\alpha / C_N \sin\alpha$
ζ_o	theoretical thrust parameter for a 60^o thin flat plate delta
η	fraction of semispan, 2y/b
η_s	boundary between attached and separated flow
Λ	sweep angle
ϕ	VG toe-in angle, towards wing apex

LIST OF TABLES

LIST OF FIGURES

I. INTRODUCTION

This section presents a brief overview of the development and characteristics of delta wing aircraft, a literature survey on drag reduction devices that could possibly offset high levels of induced drag (which is characteristic of this planform), and concludes with a discussion of the present investigation.

1.1 DELTA WING CONCEPT

The delta wing concept evolved during the 1930's as aerodynamicists began challenging the problems of supersonic flight (ref. 1). German efforts resulted in the production of the Messerschmitt ME-163 Komet interceptor aircraft which had a tailless swept-wing configuration. In 1943, a German aeronautical scientist by the name of Lippisch designed the Li P13a which was to be a ramjet-powered supersonic aircraft having a 60° swept true delta planform. A glider was built in this configuration and was to be used for low-speed manned flight tests; however, American troops captured the glider in 1945 before it was completed. It was redesignated DM-1 and subsequently tested at the Langley Research Center (refs. 2 and 3). The DM-1 will be discussed further in the next section in regard to a wing leading-edge modification intended to improve maximum lift and stability.

In 1945, R. T. Jones of the then Langley Memorial Aeronautical Laboratory published wind-tunnel test results on a slender delta wing which indicated that compressibility effects would be less than for a conventional wing (ref. 4). The following year Convair won the

competition for the development of a supersonic interceptor aircraft. Wind-tunnel tests indicated that the initial design (viz., 45° swept wing) had poor low-speed characteristics. These problems were corrected by filling in the trailing-edge gap until a true delta wing was formed. Further study revealed that high-speed performance would be enhanced by sweeping the wing leading edge further back to 60°. This research led to the XF-92A testbed delta aircraft and eventually to the production of the F-102, F-106, and B-58 aircraft.

The advantages of thin highly swept delta planforms are high drag divergent Mach number, reduced supersonic wave drag, and the capability to operate at high angles of attack due to increased lift generated by wing leading-edge "vortex flow". The principal disadvantage is the large drag-due-to-lift at angle of attack caused by the loss of leading-edge suction due to flow separation. These characteristics limit high-g transonic maneuver performance because the excess engine thrust available must be used to balance the induced drag.

Future fighter aircraft requirements specify efficient supersonic cruise for survivability and high-g maneuvering flight for air combat at high subsonic/transonic speeds. The low aspect ratio delta wing is the logical choice to meet these requirements if the lift induced drag could be alleviated. One method to achieve drag reduction would be to control the flow at the wing leading edge so as to maintain attached flow to higher angles of attack and thus offset the lift induced drag by increased levels of aerodynamic thrust, i.e., leading-edge suction. An alternative method to generate aerodynamic thrust would be to have a

small vortex act on the forward face of the wing leading edge with flow reattachment further aft.

Pursuing the concept of leading-edge flow control, a literature survey was conducted for devices that had potential for controlling flow separation on highly swept leading edges.

1.2 LITERATURE SURVEY

This survey was based on two characteristics of delta wings: aerodynamic forces act primarily at the leading edge and wing leading-edge flow separation occurs at low angles of attack. This eliminated attached flow devices such as leading-edge flaps and slots. The survey did reveal that considerable research had been conducted on "fixed" leading-edge devices - principally to alleviate/correct longitudinal instability of swept-wing aircraft. The following paragraphs discuss the devices selected for evaluation.

The bulk of the material surveyed pertained to fences specifically designed as fixes for longitudinal problems and not for drag reduction, even though a lower drag was sometimes indicated at the higher angles of attack. A typical report stated that longitudinal instability was alleviated, but goes on to add that "fences were also effective in reducing the drag-due-to-lift of the basic configuration" (ref. 5). These were upper surface fences (evaluated on a F-102 delta scale model) which were later modified by adding a wraparound projection at the wing leading edge; this configuration linearized the pitching moment and lift curves, and also reduced the drag of the basic model (ref. 6). These fences were flight tested at transonic speeds on a JF-102A aircraft configured with a conical cambered wing. Analysis of pressure measurements

indicated that flow separation typical of plane delta wings was delayed to higher angles of attack. In addition, the cambered leading edge was effective in distributing the low pressure over a greater frontal area and thus increasing aerodynamic thrust (ref. 7).

From this survey, it appeared that fences in combination with a blunt leading edge offered possibilities for achieving significant drag reduction.

Another device, called underwing leading-edge vortex generator, was evaluated at transonic speeds on a scale model of the TF-8A aircraft (equipped with supercritical wings) to determine their effect on longitudinal stability characteristics. It was reported that the vortex generators delayed pitch-up to higher angles of attack, and at the higher lift levels, the drag was reduced (refs. 8 and 9). Similar results were obtained in Sweden on a blunt 60° delta model at low speed using small wraparound wing leading-edge vortex generators. In multiple arrangements, these devices delayed pitch-up by 5° angle of attack and reduced drag by 10 percent; however, lift was reduced slightly in the mid angle-of-attack range (ref. 10).

Another type of pylon vortex generator, reported in reference 11 and called "vortilon", was positioned below the wing and aft of the flow stagnation line so that its influence on leading-edge flow would be delayed until approaching stall conditions. This device was effective in improving the longitudinal characteristics of the DC-9 aircraft with no detrimental effect on cruise performance.

From this information, it was concluded that leading-edge vortex generators had a potential for drag reduction at high angles of attack - worthy of further investigation.

The notch (hereafter referred to as slot) is another rather novel device that has been tried as a leading-edge flow manipulator to improve longitudinal stability. Reference 12 reports that multiple slots, as evaluated on a thin 45° swept-wing model, improved longitudinal stability at moderate angles of attack and provided a small reduction in drag, although at the expense of some lift. It is interesting to note that the pre-production F-106 aircraft had two pairs of fences (similar to the F-102) which were later replaced by a pair of slots and appropriately called "aerodynamic fences".

Based on this scanty information, multiple slots were perceived as having sufficient drag reduction potential to warrant testing.

The last device selected for this investigation was suggested by a fix to the DM-1 glider mentioned earlier (ref. 2). To increase maximum lift, the DM-1 researchers decided to force separation (to gain vortex lift) by attaching a small sharp strip to the wing leading edge starting at the apex and extending to the mid-semispan. This modification increased the maximum lift coefficients of the DM-1 from 0.60 to 1.01 and had negligible effect on the drag at low lift.

It was concluded from the test report that this simple device had a unique capability to control the leading-edge flow - and it was thought that a sharp extension, if properly positioned, would have an equally favorable effect on drag.

Based on the information gathered from the literature survey, an aerodynamic research program was initiated to investigate certain basic aspects of the drag-reduction capability of fences, slots, vortex generators, and sharp leading-edge extensions. The next section presents an overview of the factors influencing this program.

1.3 PRESENT INVESTIGATION

The purpose of this investigation was two-fold: (1) to generate sufficient data to quantify the drag-reduction capabilities of fixed leading-edge devices, and (2) to clarify their aerodynamic mechanisms. Since the devices were expected to perform (and perhaps even to function) differently when tested in multiples, with varying geometries and spanwise positions, and also in combinations of different types of devices, it was deemed desirable to conduct this study at low speed to achieve economy of wind-tunnel time.

Several factors influenced the wind-tunnel model design. First, the decision for low-speed testing eliminated the need for an expensive high-q qualified metal model. Secondly, since the primary interest was in flow control at the wing leading edge, it was decided that a simple flat plate model would suffice, and thirdly, to achieve drag reduction by controlling leading-edge suction would require a blunt leading edge for which little information is available. Based on these factors, a wooden flat plate cropped delta with three sets of constant cross-section wing leading edges (beveled, thin semi-elliptic, and thick semi-elliptic with static pressure orifices) was designed and constructed. Both the thin and thick semi-elliptic leading edges had chordwise slots which served two purposes: (1) to hold the fences and vortex generators

in position, and (2) to function as a device when open. The other three devices were constructed of thin flat plate aluminum which facilitated device design changes during testing, i.e., a new set of devices could be constructed in about 2 hours. The beveled wing leading edge was evaluated to establish a baseline for the thin semi-elliptic leading edge.

Geometric variables for the fences and vortex generators were limited to a reasonable number for the ensuing parametric studies. The family of chordwise fences were symmetric with the wing leading edge and had geometric parameters of height, length, and distance from the wing leading edge. The family of vortex generators extended below and ahead of the wing leading edge and had design parameters of sweep angle (down from the plane of the wing) and toe-in angle (towards the wing apex). The slot geometry was unaltered because of their secondary role of providing attachment for the thin flat plate fences and pylon-type vortex generators.

In its original configuration, the DM-1 had a low maximum lift coefficient which was partly attributed to attached flow, viz., the large thickness ratio and leading-edge radius prevented flow separation at the wing leading edge, and consequently, the development of vortex lift. In the present investigation, it was expected that flow separation would occur naturally on the wind-tunnel model at moderate angles of attack; however, it was thought that if a sharp extension would force earlier separation - and was able to maintain the resulting vortex (low pressure) along its length just ahead of the wing - then significant drag reduction would be gained.

The chord of the sharp leading-edge extension (SLEE) was scaled to that tested on the DM-1 and was positioned further out the span where it was expected to function at a lower angle of attack. The SLEE was tested in the plane of wing symmetry (as was done on the DM-1) and also in the plane of the wing lower surface - where it was reasoned that by allowing the vortex to operate on more frontal area, additional aerodynamic thrust would be generated.

The first phase of the test program involved an exploratory investigation of the four types of devices on the thin semi-elliptic leading edge. Ninety test runs were made during this phase which evaluated the geometries, positions, and multiplicity of devices and established a data base. From this information, the best device in each family was selected for phase two testing on the pressure instrumented thick semi-elliptic leading edge. The balance and pressure data collected during this phase added to the data base and was used to evaluate leading-edge radius effects and to gain a better understanding of the aerodynamic mechanisms associated with the devices.

It must be emphasized that the present investigation was a parametric study of simple fixed position leading-edge devices and that no attempt was made to optimize the design of the devices. However, this study does provide the data base from which an optimization program could be developed.

The data presented in this thesis are in graphical form - the tabulated data are contained in reference 13.

II. RESEARCH MODELS AND LEADING-EDGE DEVICES

Descriptions of the models and leading-edge devices used for this investigation are presented in this section.

2.1 RESEARCH MODELS

2.1.1 60° Delta (Tests 47 and 51)

This wooden model of cropped-delta planform was provided with two pairs of leading edges of constant cross-section: semi-elliptic and wedge. The semi-elliptic leading edges had six chordwise slots at the 25, 37.5, 50, 62.5, 75, and 87.5 percent semispan positions to hold the devices (i.e., fences and pylon-type vortex generators). A balsa-wood housing on top of the wing covered the six-component balance. A drawing of the model is shown in figure 1 and other pertinent data are presented in Table 1.

2.1.2 60° Delta (Test 63)

The model described above was modified for Test 63. It had thicker semi-elliptic leading edges (twice the thickness previously tested) with slots at the 25, 37.5, 50, 62.5, and 75 percent semispan positions. The right-hand leading edge was instrumented with chordwise rows of static pressure orifices at the 20, 33, 45, 57, 70, and 82 percent semispan positions (see ref. 13 for orifice coordinates). The balance and scanivalve (see Table 1 for limits) were mounted on the upper and lower surfaces, respectively, and each covered with an aluminum fairing. An aluminum plate was attached to the lower surface to cover the static pressure tubing. This model is presented in figure 2 with pertinent data contained in Table 1.

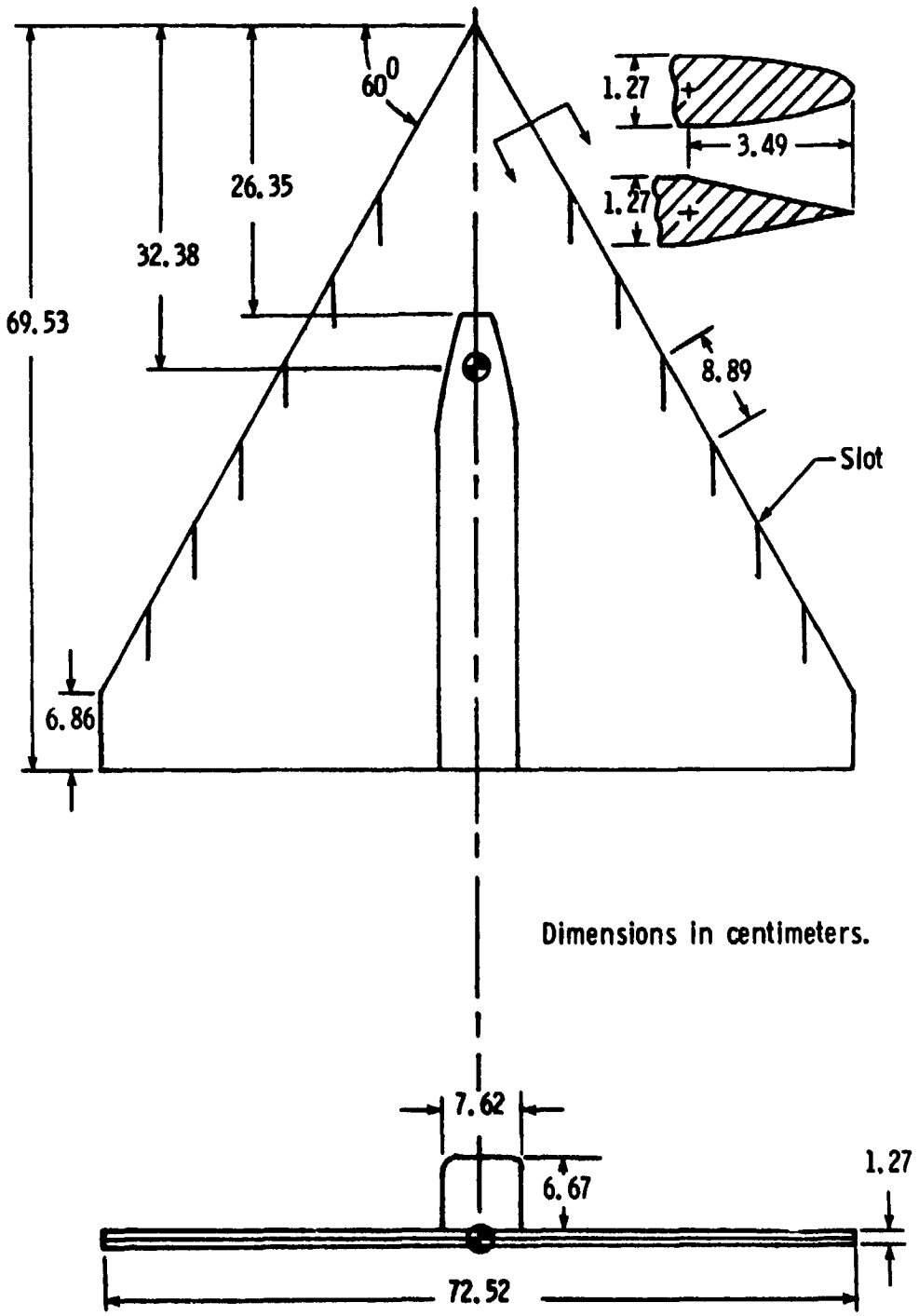

Figure 1. - Details of model used for Tests 47 and 51.

Table 1

Model Characteristics, Test Conditions, and Data Measurement Capabilities

Characteristics	Thin Wing Test 47/51	Thick Wing Test 63
Model		
Sweep angle	60°	60°
Wing area, cm^2	2765	3264
Span, cm	72.5	72.4
Reference chord, cm	46.4	50.9
Aspect ratio	1.90	1.61
Taper ratio, percent	9.87	18.16
Leading-edge radius, cm	0.117	0.231
Boundary-layer transition trip, chordwise, cm (60 grit) (ref. 14)	3.0	none
Moment reference center, cm		
x, from apex	32.38	32.38
z, from upper surface	-0.635	-0.635

Test Conditions	Thin Wing	Thick Wing
Mach number	0.20	0.16
Reynolds number, based on reference chord	2.3×10^6	2.0×10^6

Measurements	
Balance	
Normal force	2669 ± 13.34 N
Axial force	222 ± 1.11 N
Side force	1334 ± 6.67 N
Pitching moment	113 ± 0.56 J
Rolling moment	34 ± 0.17 J
Yawing Moment	68 ± 0.34 J
Pressure Transducer	35000 ± 172 N/m^2

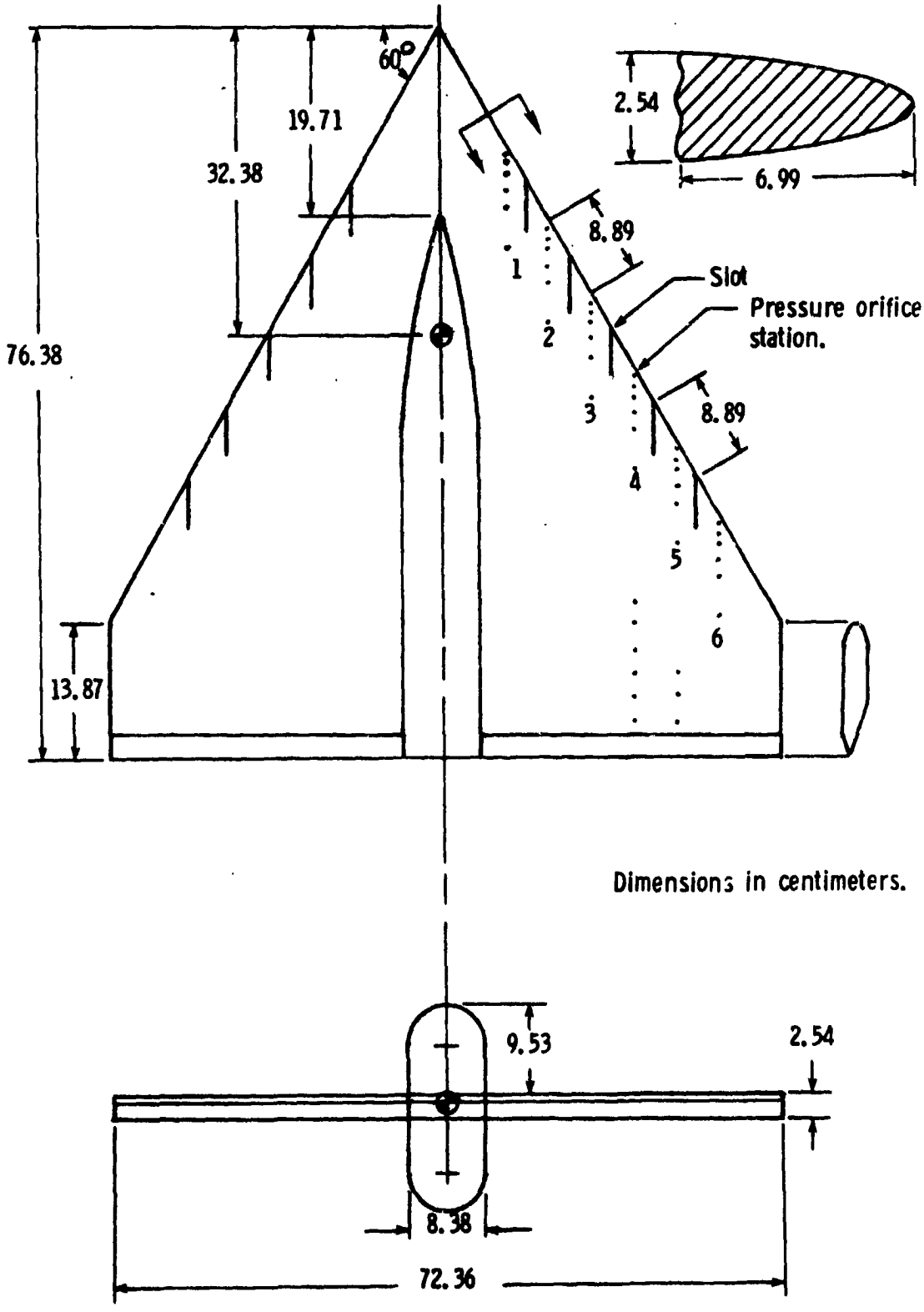

Figure 2. - Details of model used for Test 63.

2.2 LEADING-EDGE DEVICES

2.2.1 Open Slots

The wing leading-edge slots were nominally 5.1 cm in length chordwise and 0.089 cm in width for all tests. These slots, the same as used to hold the devices, were sealed when not in use.

2.2.2 Fences

Figure 3 presents the geometry and dimensions of the fences tested on both sets of semi-elliptic wing leading edges. This family of leading-edge devices was made from flat plate aluminum stock and held in position by the slots.

2.2.3 Pylon-Type Vortex Generators (VG)

The geometry and dimensions of this family of d ices are shown in figure 4. The dimensions of these devices were kept constant for all tests. With the exception of vortex generator (VG) number 3, these devices were flush with the wing upper surface starting at the wing leading-edge apex. VG 4 and VG 6 had a 10° inboard toe-in angle while VG 5 had a 20° inboard toe-in angle (relative to the wing chord line). These devices also were constructed of thin aluminum and held in position by the slots.

2.2.4 Sharp Leading-Edge Extensions (SLEE)

When fastened to the lower surface of the wing, these 0.1-cm thick aluminum devices projected ahead of and parallel to the leading edges (fig. 5). The mid-position (M-SLEE) was symmetric with respect to the wing leading edge while the low position (L-SLEE) was in the plane ot the wing lower surface. Note that the fences when tested in combination with the L-SLEE were moved forward in the slots to match the SLEE leading edge.

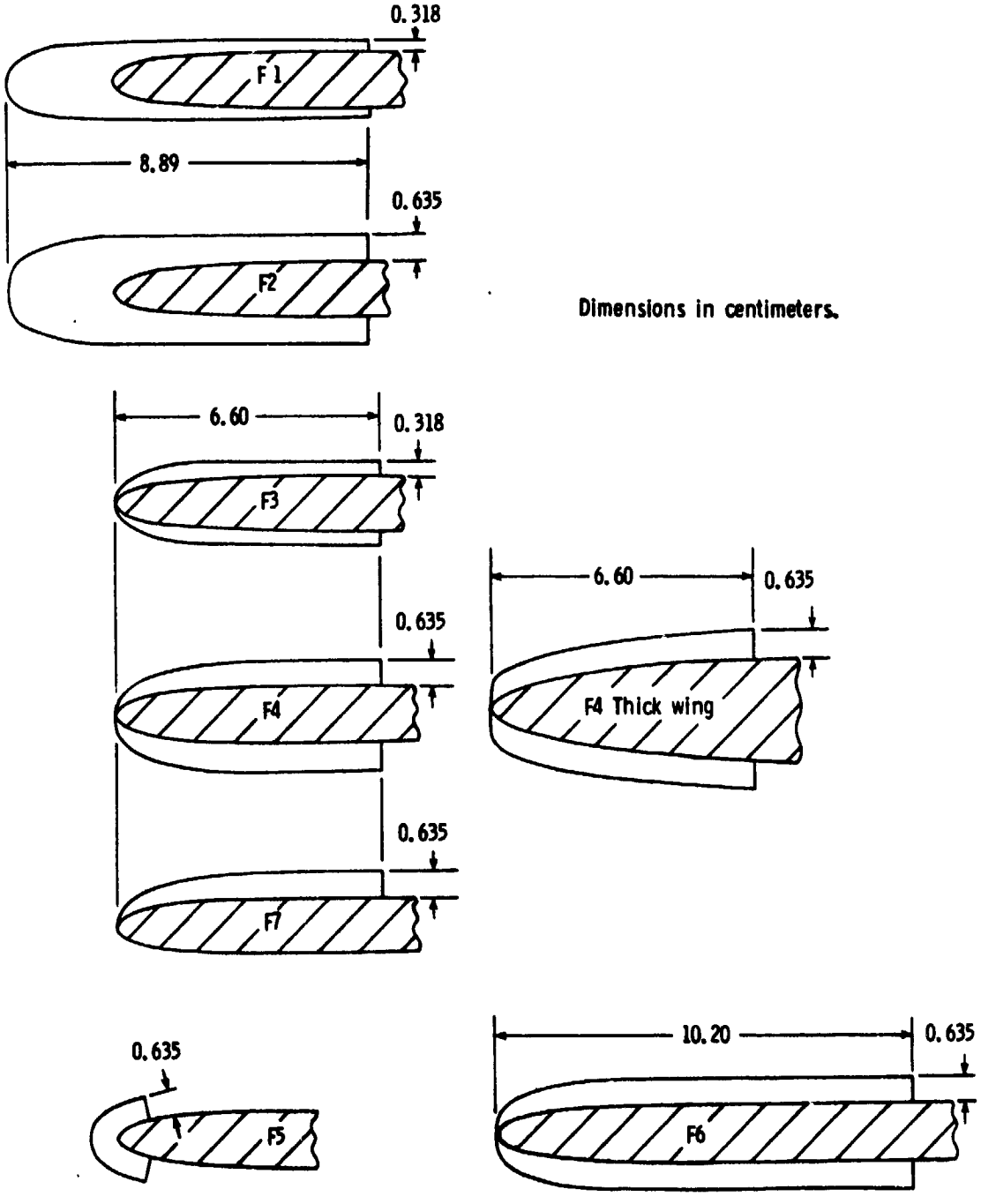

Figure 3. - Drawing of fences tested.

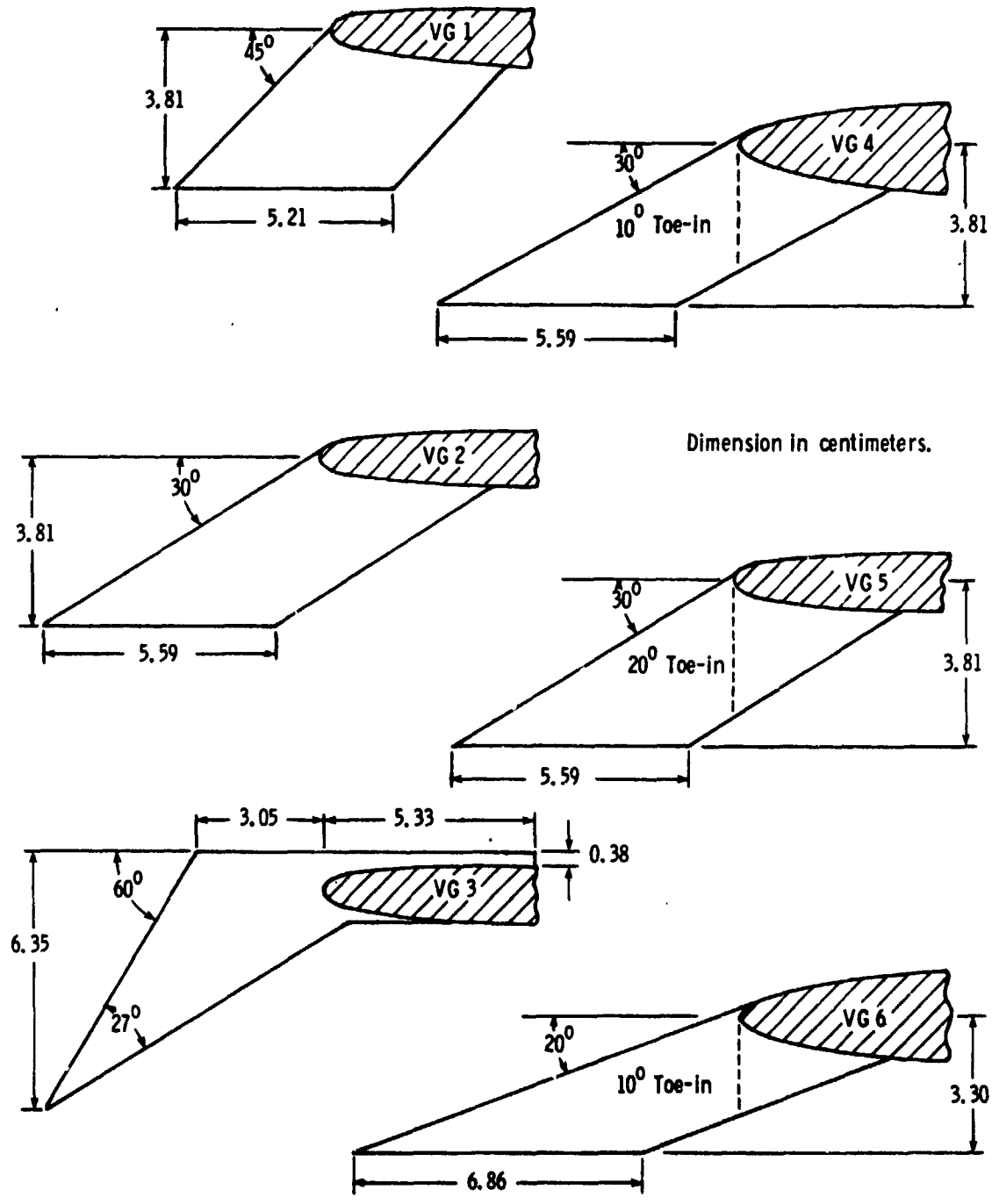

Figure 4. - Drawing of pylon-type vortex generators tested.

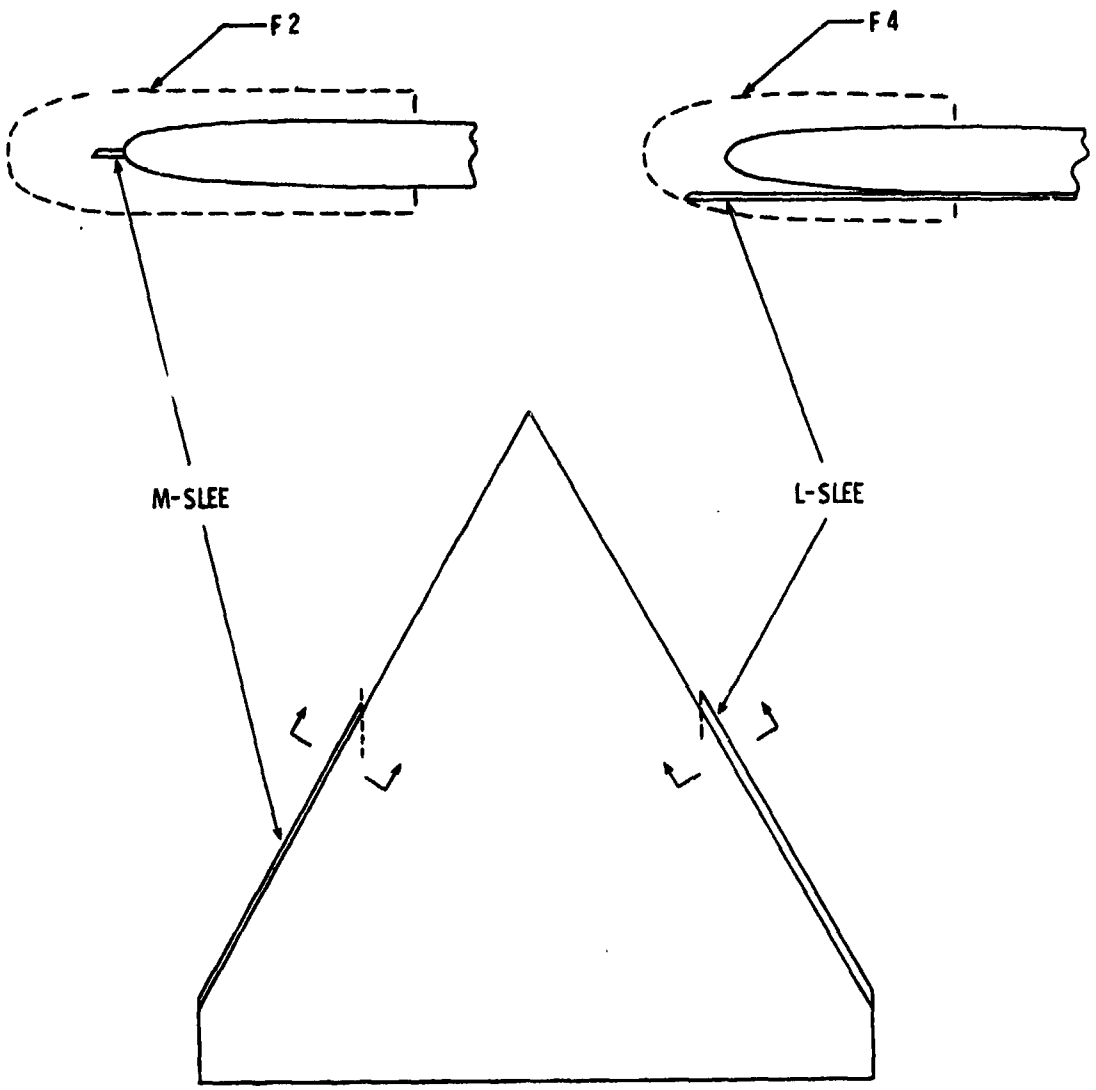

Figure 5. - Drawing of mid and low sharp leading edge extensions with projections of 0.64 cm and 0.89 cm respectively.

III. WIND-TUNNEL FACILITY

The following paragraphs present a brief overview of the test facility used for this investigation. Specific details can be found in the references.

3.1 DESCRIPTION

This series of tests were conducted in the NASA Langley Research Center's 7- by 10-foot high-speed tunnel. This is a continuous flow, closed-circuit, atmospheric tunnel with test-section speeds varying from very low to approximately Mach = 0.94. Reference 15 contains the details on tunnel calibration and test capabilities.

3.2 DATA ACQUISITION AND OUTPUT

This facility is equipped with a dedicated on-site computer system which operates a digital data acquisition, display, and control system. System output is recorded on a line printer and displayed on a graphics terminal with hard copy capability. Reference 16 contains the details on system capabilities and data reduction.

3.3 TEST SECTION AND MODEL SUPPORT SYSTEM

The walk-in test section is nominally 213 cm high and 305 cm wide, with 335 cm of usable length. Figure 6 shows the test section and the vertical strut used to hold the sting support system. Both the standard (Test 51) and high angle stability (Tests 47 and 63) stings were used during this investigation.

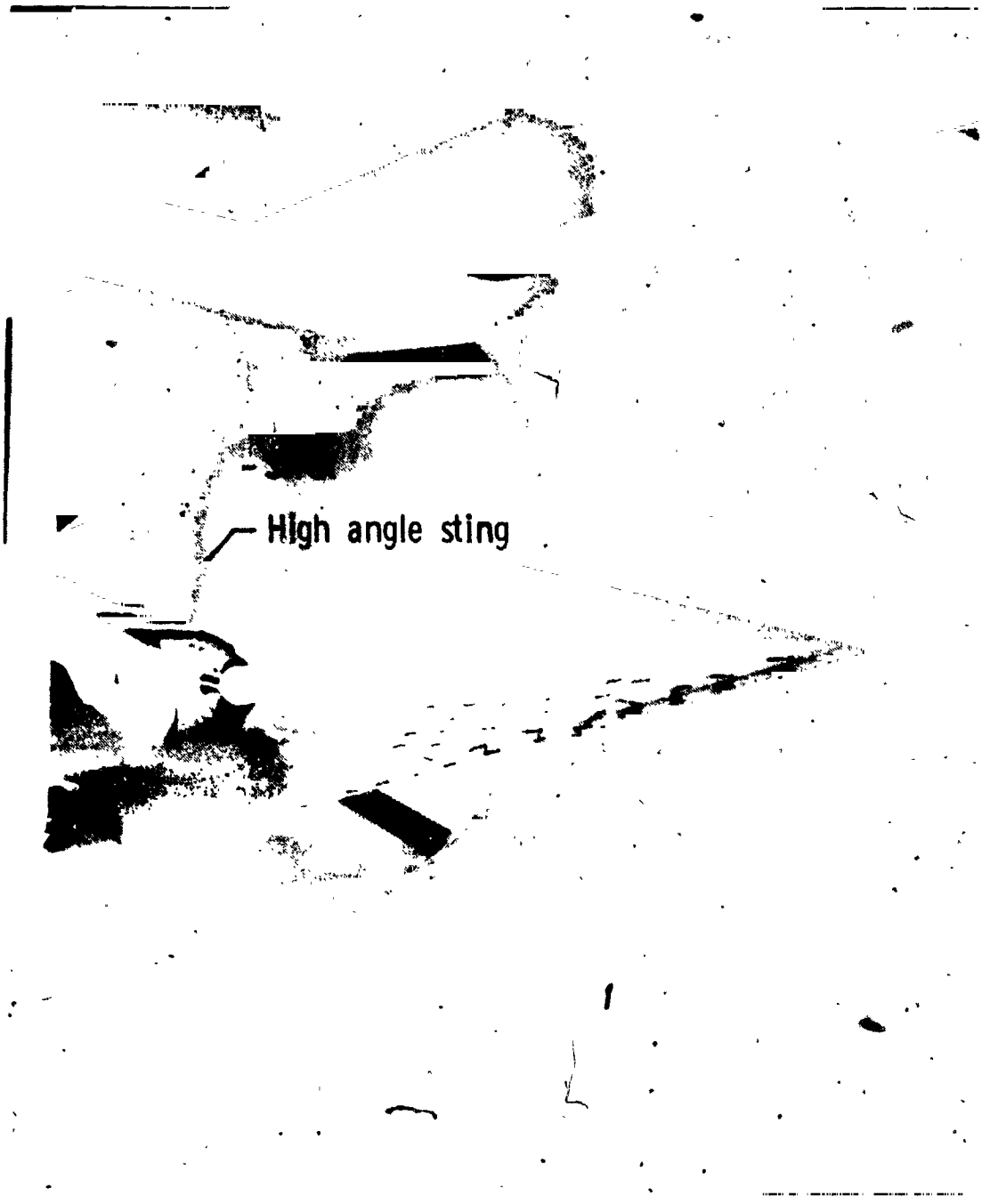

Figure 6.- Picture of test section.

3.4 FLOW VISUALIZATION

Flow visualization studies, using smoke, oil, and tuft techniques, were conducted during the course of this research and proved useful during data analysis. Figure 7 shows a typical smoke setup in which kerosene smoke is introduced ahead of the model by a hand-held generator and the resulting flow streamlines observed and photographed. Surface flow patterns were visualized at test Mach number using fluorescent oil and tufts that would luminesce under ultraviolet light (see ref. 17 for mini-tuft techniques). These techniques provided a "footprint" of the separated vortex flow which were remotely photographed through top and side windows of the test section.

BLACK AND WHITE PHOTOGRAPH

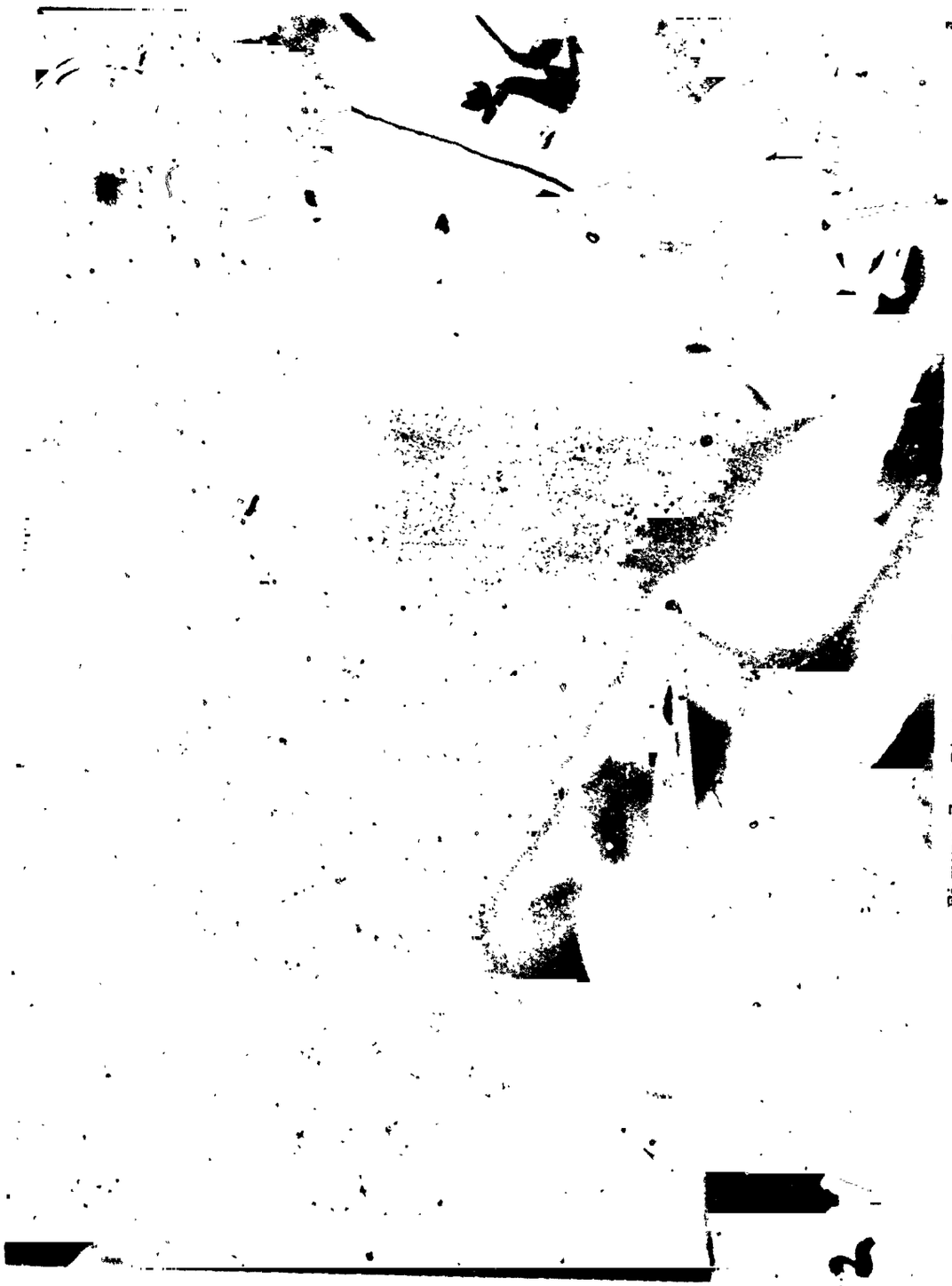

Figure 7.- Picture of typical smoke visualization study.

IV. CALIBRATION AND DATA CORRECTION PROCEDURES

This section presents a brief overview of calibration procedures and corrections to data. Further details can be found in the references.

4.1 CALIBRATIONS

The six-component strain-gage balance was calibrated, both in the laboratory and on the sting, so that measured forces and moments could be converted to engineering units. The accelerometer was calibrated to obtain true angle of attack. In addition, the pressure transducer used in Test 63 was calibrated to obtain engineering units.

4.2 CORRECTIONS TO DATA

For the test conditions of this study, no correction for longitudinal buoyancy was required (ref. 15). Reference 18 was used to compute solid and wake blockages due to the model. Jet boundary corrections were applied to angle of attack as derived from reference 19, as well as corrections for aerodynamic loading of the sting support system. Corrections for model weight were applied to force and moment data. Chamber pressure measurements were used to eliminate housing drag in the drag data.

V. DATA PRESENTATION

Before proceeding to the analysis of the data, the aerodynamic coefficients selected to evaluate the characteristics and performance of the devices will be introduced along with the methods of presentation. Definitions for the coefficients can be found in the List of Symbols. Basic wing data are presented in graphical form as a dashod line for comparison purposes. The following two subsections discuss the static pressure and balance derived data.

5.1 BALANCE DATA

The diagrams in figure 8 show the orientation of the aerodynamic coefficients with respect to the body axis and wind axis coordinate systems. Angle of attack (which is alternately referred to as "α" or "alpha" in the text) is the angle between the free-stream flow and the wing. For a symmetric airfoil at $\alpha = 0^{o}$, the only nonzero force acting is the profile drag (a combination of skin-friction and pressure/form drag); however, with increasing angles of attack, an unbalance in other aerodynamic forces develops. The normal force and axial force coefficients (C_N and C_A) were selected to evaluate drag reduction performance of the devices instead of the usual wind axis coefficients.

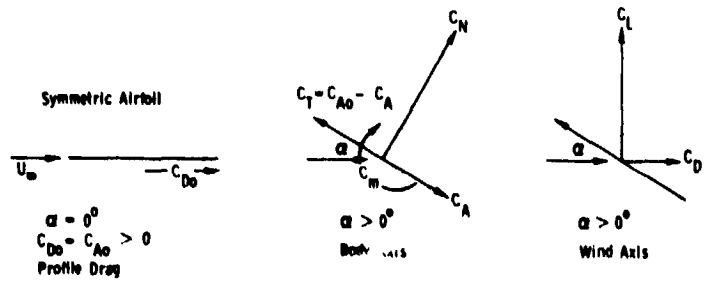

Figure 8.- Diagram showing the orientation of aerodynamic coefficients.

This was done because C_A is a more sensitive indicator of changes in drag.

A typical presentation of these coefficients is shown in figure 14. In the upper graph, two aspects of thin symmetric airfoils can be noted - $C_N = 0$ at $\alpha = 0^\circ$, and the data are linear to about 8° α, but nonlinear beyond. The break in the data at 8° indicates the onset of leading-edge (LE) separation ($\alpha_D = 8^\circ$) which is closely followed by the development of a primary vortex system which originates at the wing tip and moves inboard along the LE to the wing apex. LE separation is also evident in the center C_A graph near 8° α by the departure of the curve from an initial parabolic shape; the subsequent severe reversal in the data near 10° α indicates a significant thrust loss most likely caused by flow separation at the wing trailing edge. The inherent ability of the C_A coefficient to reflect changes in the aerodynamic thrust ($C_T = C_{A_O} - C_A$) makes it a highly visible drag type coefficient that is well suited for this investigation.

Figure 25 contains a typical comparison between LE devices and the basic wing (dashed line). The C_A data for the fence-on cases indicate greater negative values beyond $\alpha_D \approx 8^\circ$ which implies lower drag. This is confirmed by the drag parameter ($PD = C_D - C_{D,BW}/C_{D,BW}$) in the center graph, viz., by adding three fences to the basic wing, a drag reduction of 27 percent at 12° α is possible. Thus, C_A was selected as the primary coefficient to compare the drag performance of the LE devices.

The pitching-moment coefficient (C_m) was another important aerodynamic coefficient used to evaluate the LE devices. An example is at

the bottom of figure 25 which shows that C_m is negative at $\alpha = 0^o$ - a characteristic typical of tailless planforms. The basic wing (dashed line) has a gentle slope to about 6^o α which is a favorable aspect; however, the subsequent sharp downturn is an undesirable feature that will cause serious control problems. Near 10^o α, the basic wing becomes longitudinally unstable (pitch-up) as indicated by the reversal in the curve; the fence-on cases have improved the longitudinal characteristics by reducing the slope beyond 8^o angle of attack and delaying pitch-up by several degrees α. (Note that the C_m data for the thin wing have been modified from that reported in reference 13 by moving the moment reference center 5.1 cm further aft in order to magnify/illustrate characteristic variations with α.)

Additionally, balance data for the thick wing is included with pressure data in discussions of LE device flow mechanisms. (See example in figure 26(b).) Note that the pitching moment is referenced to 47 percent of the root chord. The next section explains the method used to convert the static pressure measurements into the wing leading-edge thrust coefficient C_T.

5.2 PRESSURE DATA

Pressure data were collected during Test 63 (thick wing) to achieve a better understanding of the operation of the devices by means of aerodynamic thrust distributions along the wing leading edge. Since reference 20 established that aerodynamic forces on delta wings occur primarily along the leading edge, it was decided to instrument the right leading edge with static pressure orifices. (See Section 2.1.2 for model instrumentation.) Discussions follow on the integration of the

static pressure data to obtain the thrust coefficients, $C_{T,LCL\ PRESS}$ and $C_{T,TOT\ PRESS}$, and the presentation of these data. Also figure 9 is included to assist in this discussion.

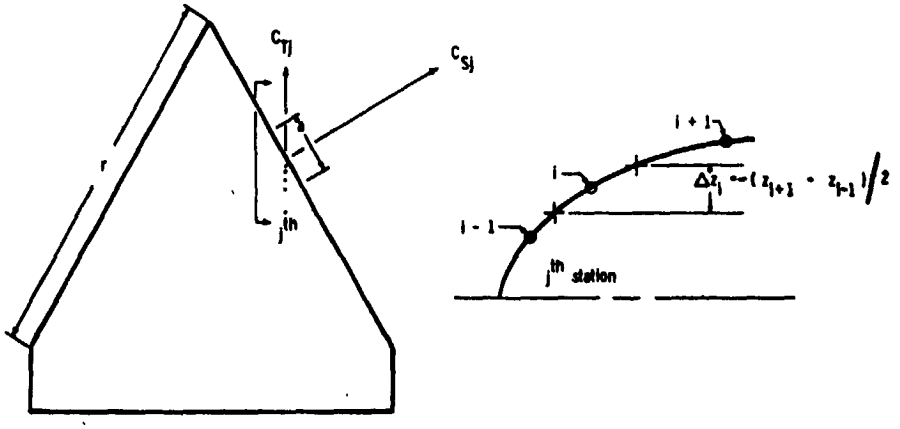

Figure 9.- Drawing showing the parameters used in the computation of the pressure derived thrust coefficient.

The local suction force

$$\sum_{i=1}^{m} SF_{ij}$$

developed around the leading edge of a station is defined to be

$$\sum_{i=1}^{m} (p_{ij} - p_{\infty})\ a\ \Delta z_{ij}$$

where p_{ij} is the measured static pressure at the i^{th} orifice of the j^{th} station, a is the measured distance along the leading edge of the j^{th} station (which is considered constant for the model tested), and Δz_{ij} is the vertical distance that p_{ij} operates on. With the assumption that the suction force per unit length of leading edge is a constant

$$\sum_{i=1}^{m} SF_{ij}/a$$

then the total suction force exerted on the wing by a station would be

$$(2r) \sum_{i=1}^{m} SF_{ij}/a$$

where $2r$ is the total distance along both leading edges. By using the relations $p - p_\infty = q_\infty C_p$ and $C_T = C_S \cos\Lambda$ (Λ being the wing sweep angle), and dividing by the reference force $q_\infty S_{ref}$, yields

$$C_{T,LCL\ PRESS} = C_{Tj} = \sum_{i=1}^{m} (2r)\, C_{pij}\, \Delta z_{ij}\, \cos\Lambda / S_{ref}.$$

Averaging the sum of the local thrusts leads to

$$C_{T,TOT\ PRESS} = \frac{1}{n} \sum_{j=1}^{n} C_{Tj}.$$

The thrust distributions thus derived, along with balance data and flow visualization pictures, have been used to establish LE device flow mechanisms. Because of the volume of information involved, the data for each device have been condensed and standardized into a two-part figure ((a) and (b)). The following paragraphs describe the figure layout and serve as a guide for all the devices.

In figure 26(a), the device and configuration is shown at the top of the page with the relative position of the two pressure stations selected for discussion shown by dots. The first two columns of graphs

present the pressure coefficient around the leading edge in a chordwise direction (C_p vs. x, in.) for three angles of attack. In the case of the SLEE, the lower surface data are shown with square symbols. The last column shows the thrust coefficient distribution along the semispan ($C_{T,LCL}$ vs. η) for four angles of attack. The dashed lines represent basic wing (no device) data which will be used as a baseline to compare the devices. The arrows indicate the position of each device.

The last two columns in figure 26(b) show the $C_{T,LCL}$ distributions versus α for the six pressure stations. These distributions were also used to determine the local onset of LE flow separation defined as the first decrease in slope beyond the linear portion of the curves. This established a boundary between attached and separated flow as can be noted in the η_s vs. α graph in the lower left corner of the figure.

VI. DISCUSSION OF RESULTS

This section deals with analyses of the data and starts with a discussion of the factors that could contribute to inaccurate or misleading conclusions. The aerodynamic characteristics of the basic wing are discussed first to establish a reference, followed by comparisons of the leading-edge devices tested, and concludes with a summary of the results. The best performing configuration within a family of devices is compared with the basic wing and flow mechanisms pertaining to the devices are suggested.

6.1 FACTORS INFLUENCING TEST DATA

6.1.1 Balance Accuracy

The quoted instrument limit of error of the six-component balance, which is presented in Table 1, would suggest that accuracy was not a factor bearing on the results of this investigation, except possibly in the axial direction when the absolute magnitude of the data might fall below the threshold sensitivity of the balance. A graph of the uncorrected balance measured axial force (AF) versus α is shown in figure 10, where the dashed line represents the balance threshold sensitivity and data system error. A comparison with the axial-force coefficient data in the same figure shows that the AF curve is a minimum near the departure angle of attack but has not entered the region of uncertainty. Therefore, the axial force data are considered accurate for this study.

6.1.2 Sting Support Systems

A rule of thumb for minimizing sting interaction is that the base of the model should be at least 5 to 6 balance housing diameters upstream of the first tapered section of the sting. The standard sting used during Test 51 meets this requirement and has been proven through previous test experience to have no significant influence on the data. However, it should be remembered that blockage can result in misleading conclusions and that this effect is an important consideration in wind-tunnel research.

6.1.3 Data Repeatability

It is uneconomical to conduct comprehensive error analysis of wind-tunnel data and was certainly not required for this investigation;

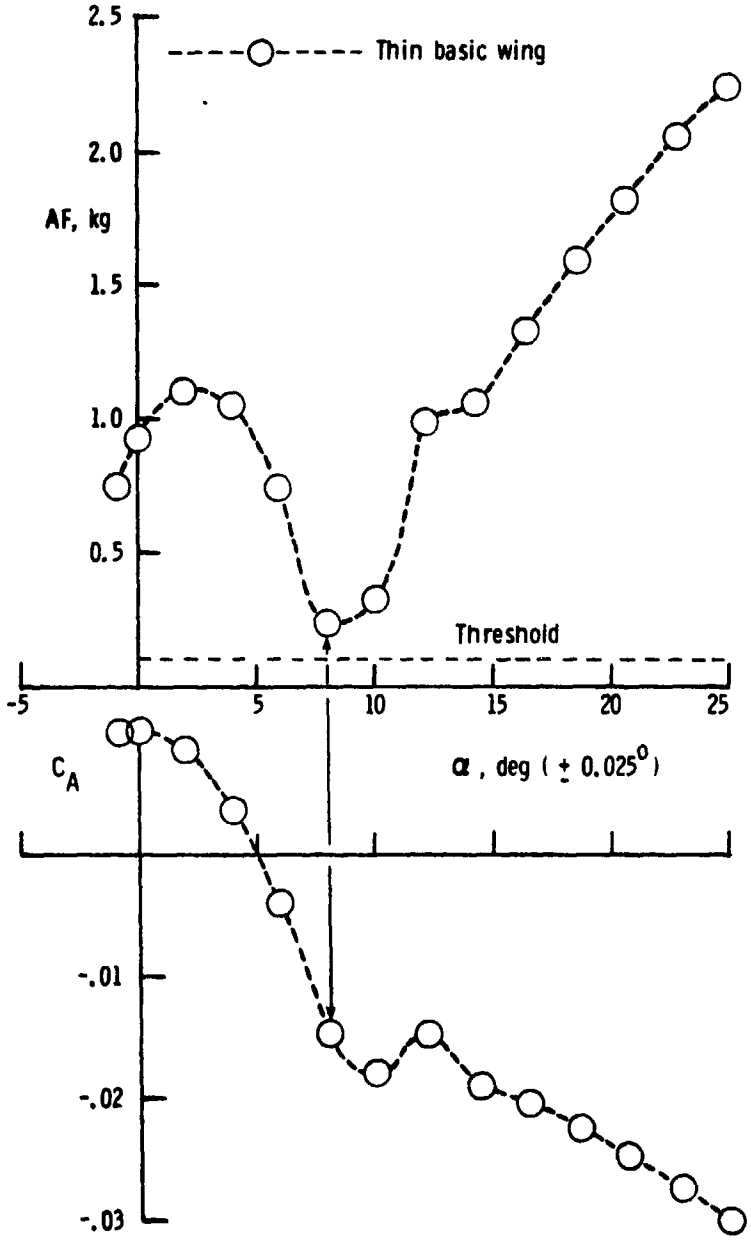

Figure 10.- Balance accuracy - axial component.

however, a minimum check of the repeatability of the data collected was made during the final test. Two sets of data were taken at a constant α before proceeding to the next angle of attack. At the four α steps thus investigated, the maximum difference in C_A balance (the most critical) was 0.56 percent, and the pressure coefficients showed almost identical distributions at all stations. It was, therefore, concluded that data repeatability was not a factor of concern in this investigation.

6.1.4 Boundary-Layer Transition Trip

As a practical measure, in order to avoid the possibility of disturbing the pressure measurements, it was decided that a transition trip was not necessary for Test 63 because in the α range of interest, the wing was under the influence of LE separation, viz., the flow would separate prior to reaching the trip. To verify this decision, a comparative test was made of the basic wing with a 60 grit trip located in a narrow band 3.3 cm aft of and parallel to the wing LE on both the upper and lower surfaces. Comparison of the longitudinal coefficient data (fig. 11) showed that minor variations did occur. The C_N versus α data are seen to be almost identical as is the case for the C_A data except that the latter has a minor deviation at $\alpha \approx 16^{\circ}$. The pitching-moment coefficient (C_m) data shows a small scatter at low angles of attack, but very close agreement in the α range of interest (beyond $\alpha = 8^{\circ}$). On the evidence of this comparison, it was concluded that a boundary-layer transition trip was unnecessary for this study.

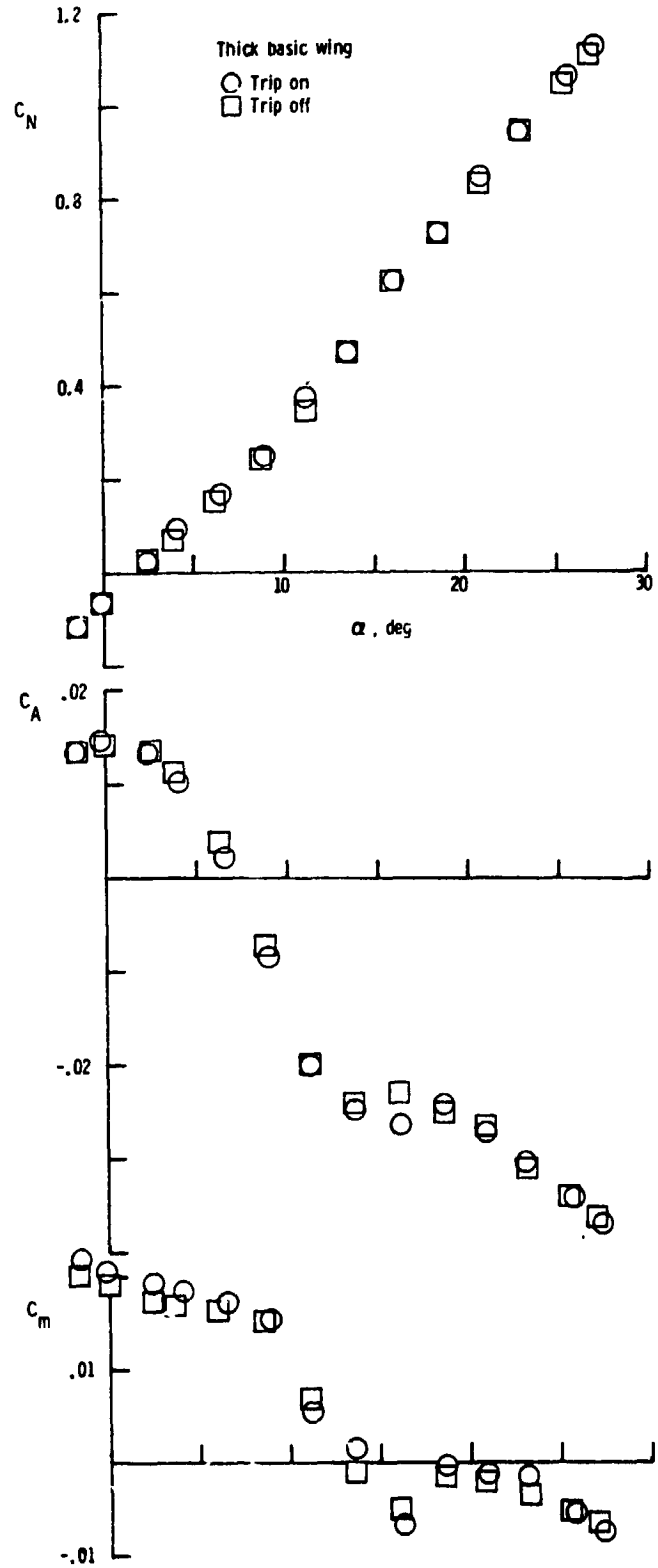

Figure 11.- Effect of boundary-layer transition trip on the performance of the thick wing (Test 63).

6.1.5 Fluorescent Mini-Tufts

A novel experiment was conducted during the course of Test 63 that involved the simultaneous collection of force and pressure data as well as flow visualization pictures. Based on the information contained in reference 17, very small (0.02 mm diameter) nylon monofilament material, which has been treated with a fluorescent dye, will radiate in the visible spectrum when illuminated with an ultraviolet light source, and hence, photographed without interfering significantly with the flow field. An example can be seen in figure 18. This concept of disturbance free surface flow visualization which allows simultaneous photographic-balance-pressure recording over a range of angles of attack has potential for considerable economy of wind-tunnel test time.

A verification of this concept was attempted following the first run (no tufts) when approximately 1000 mini-tufts nominally 3.2 cm in length were glued to the wing upper surface using a mixture of three parts Duco cement and one part lacquer thinner which, when dry, could not be felt by the fingertips. The results are presented in figure 12.

The C_A versus α data show close agreement except near $\alpha = 12^{\circ}$ which could be attributed to the condition of the leading edge and will be discussed in the next subsection. At $\alpha = 11.5^{\circ}$, the pressure data at the 45 and 70 percent semispan positions show almost identical pressures for both cases except for a slight deviation in the upper pressures at $\eta = 0.70$.

On the basis of the foregoing data, the mini-tufts were retained for the duration of testing.

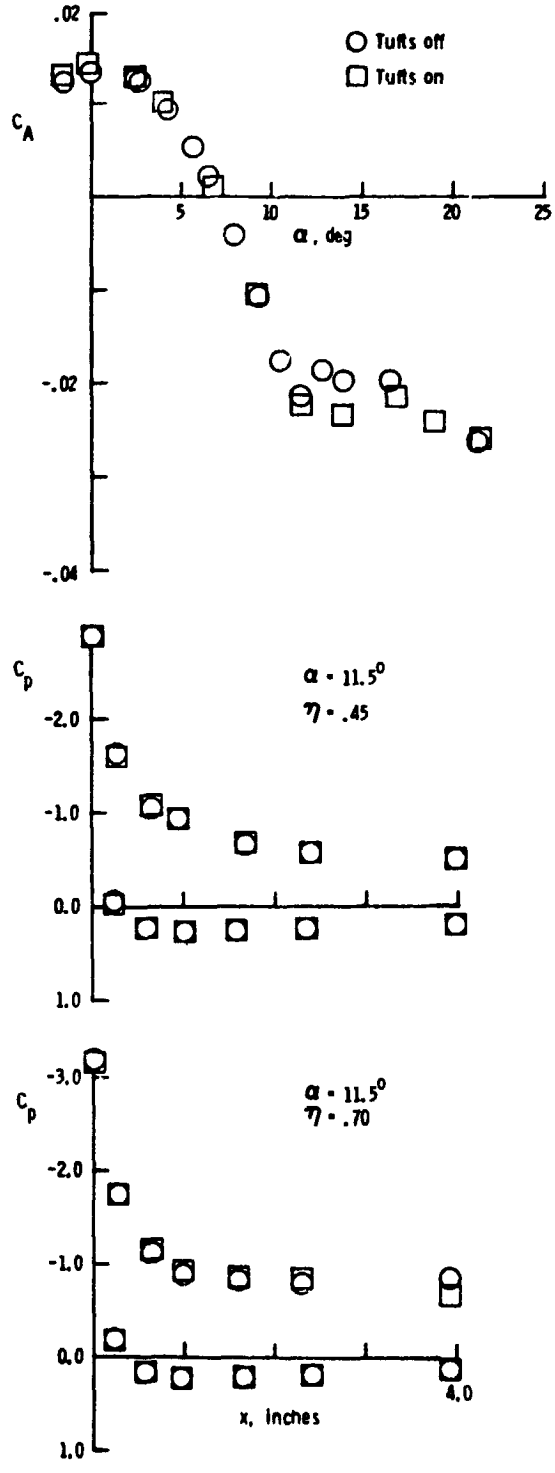

Figure 12.- Effect of mini-tufts on force and pressure measurements.

6.1.6 Wing Leading-Edge Surface Condition

It became apparent during Test 51 that the LE was being aerodynamically degraded by the model change procedures, i.e., accumulation of plaster on and near the transition trip and nicks in the wood surface in the vicinity of the slots. To determine the influence of surface condition on the data, a test was conducted in which the LE was covered with a smooth skin material (Unicote). The first two tests (Runs 56 and 57) of this series were unsuccessful due to peeling of the Unicote during the runs. The last test (Run 58) was conducted after the model was completely reconditioned and a new transition trip applied as before.

The primary variation in the data occurred with C_A and is presented in figure 13. This comparison indicates a minor scatter in the data between 8° and 13° angle of attack with the two Unicote runs showing a more gradual loss of LE suction than the reconditioned wing. A possible explanation is contained in reference 10 which reported that very small steps at the LE that were just barely noticeable to the touch of the fingertip, could cause an effect similar to that of a vortex generator, i.e., a more gradual LE separation. For this to occur in the present study, the irregularities around the slots must have projected through the Unicote material, thus altering the flow. This is believed to be the case because after the model was reconditioned for the final run of this test, the slots could not be felt with the fingertip.

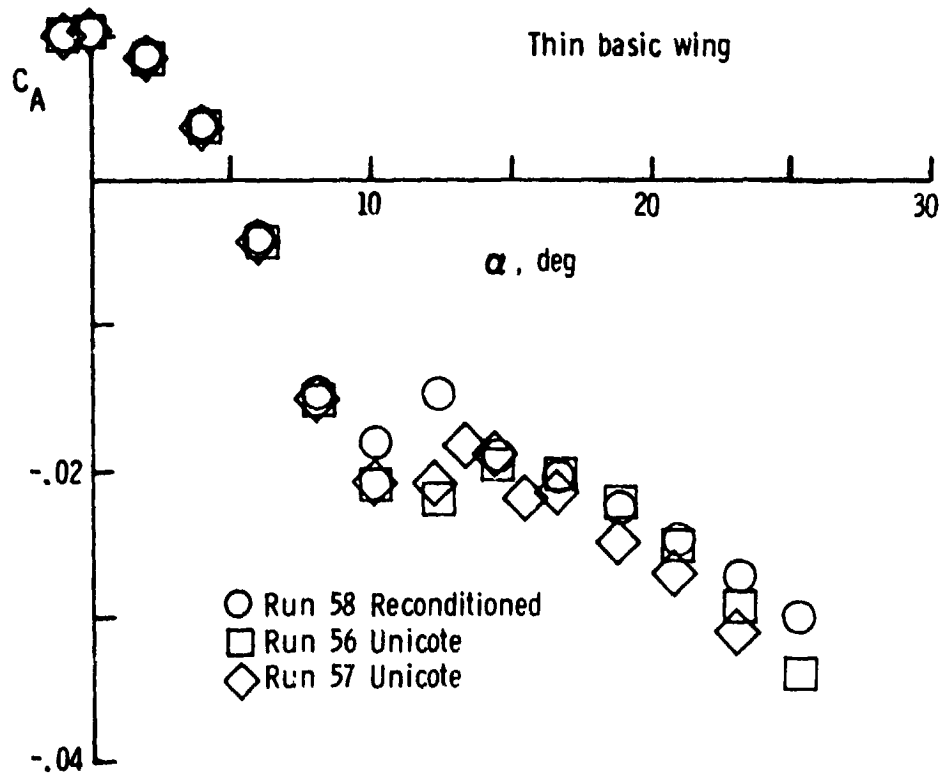

Figure 13.- Effect of leading-edge surface condition on force measurements.

From this discussion, it is concluded that the final test (Run 58) provided valid data for the purposes of this research. It is also noted that LE surface condition can be an important factor in experiments concerned with LE flow separation.

6.2 BASIC WING AERODYNAMIC CHARACTERISTICS

6.2.1 Delta Wing Flow Mechanisms

The general character of the flow over delta wings with blunt leading edges will be discussed before presenting the results of this study. There are two angles of attack (α) ranges to consider: the low α range for which the flow is fully attached around the leading edge (laminar and/or turbulent boundary layer), and a higher α range in which LE flow separation predominates. The separated flow develops into a spiral vortex sheet that rolls up into a vortex core over the leading edge. The vortex origin moves along the leading edge from the tip to the wing apex with increasing α, following the inboard spread of separated flow. The primary vortex will eventually burst causing a sudden reduction in rotational energy which dissipates into turbulence. The complexity of the vortex system, with primary, secondary, and perhaps tertiary vortices, is discussed in reference 21. The parameters that influence the change from attached to separated flow are discussed below.

The angle of attack at which the changes in the type of flow (i.e., onset of separation and vortex formation) first become evident in the overall aerodynamic characteristics of the wing (viz., normal force, axial force, and pitching moment) is called the departure angle of attack (α_D), and is a function of LE radius, wing sweep angle, and Reynolds number. LE blunting increases α_D by allowing attached flow to persist to higher angles of attack, whereas increasing LE sweep for a given radius causes earlier departure. It has been found that LE radius and wing sweep effects may be combined into a single parameter, viz., LE

radius Reynolds number (R_{LER}) based on the free-stream velocity component normal to the LE (ref. 22). Increasing R_{LER} makes the LE boundary layer (normally turbulent because of sweep-induced instability that forces early transition of the laminar boundary layer) relatively thinner, and therefore, more resistant to separation in the adverse pressure gradient region starting just downstream of the LE - thus increasing α_D. With further increase in α, additional (and more drastic) changes in the overall force and moment characteristics can occur as the point of vortex burst moves upstream from the wake region onto the wing.

It should be clear from the above discussion that the flow over delta wings is basically complex and that LE devices add to this complexity. The mechanisms associated with the vortex system will be discussed next using balance, pressure, and flow visualization.

6.2.2 Thin Basic Wing (Test 51, Run 58)

The basic wing (without devices) was tested to establish a base line for comparative assessments of the LE devices. Prior to the test, the model was reconditioned by filling the LE slots with plaster, sanding and painting the model, and applying a new transition trip to the upper and lower surfaces. The finish on the LE was such that the slots could not be felt by fingertips. The following paragraphs discuss the aerodynamic characteristics and oil flow visualizations and comparison of data with theory.

The normal force, axial force, and pitching-moment coefficients, as shown in figure 14, indicate trends typical of a delta wing with blunt LE, i.e., fully attached LE flow at low angles of attack followed

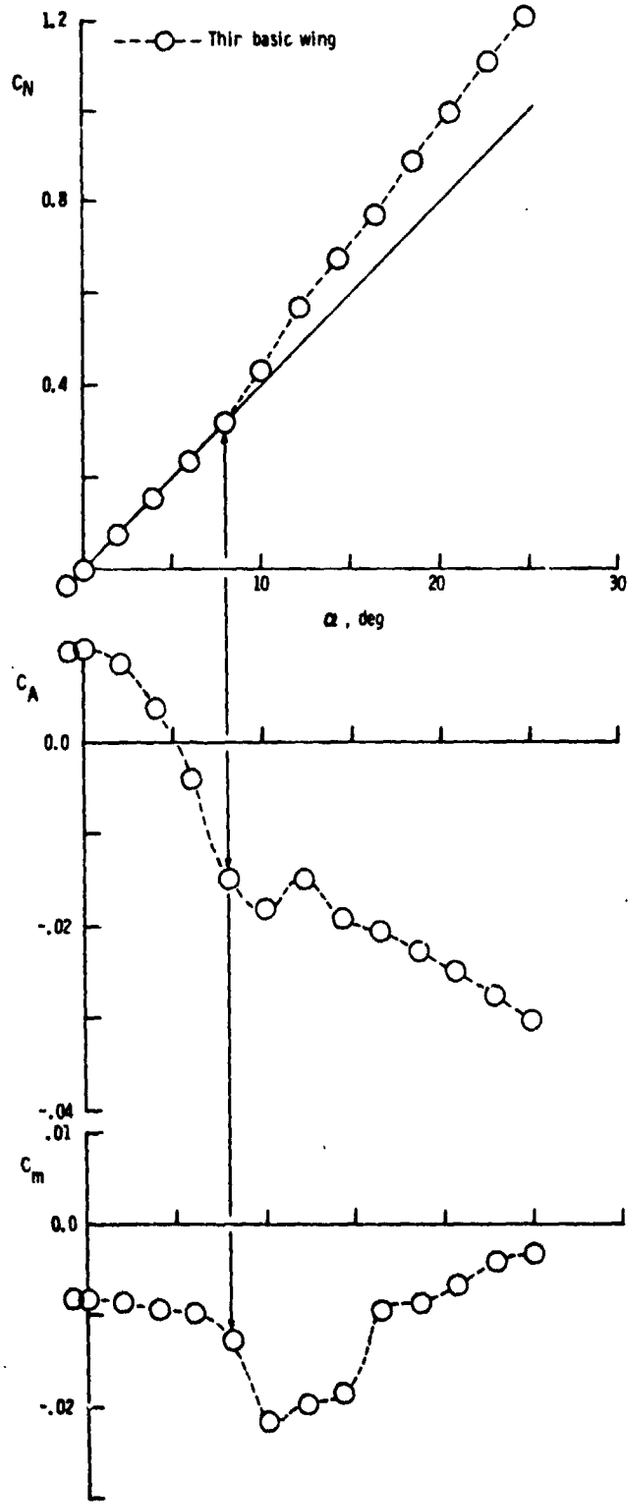

Figure 14.- Aerodynamic characteristics of the thin basic wing.

by LE separation at higher angles. For this wing, $\alpha_D \approx 8^o$ can be recognized by the sudden increase in the C_N slope curve and by the simultaneous departure of C_A from the initial parabolic curve (i.e., LE separation causing loss of LE suction). From these two curves, it is apparent that vortex (or nonlinear) lift has been generated at the expense of LE suction (or thrust). Note also that through the range of angle of attack beyond α_D the vortex lift has been maintained and that C_A shows a slight recovery. It is precisely this exchange between the normal- and axial-force coefficients that causes the additional (vortex) lift on a delta wing to be necessarily accompanied with a drag penalty.

The pitching-moment coefficient (C_m) is also influenced by the development of the vortex system. At $\alpha_D \approx 8^o$, the curve shows a definite nose down trend which can be attributed to the vortex lift being generated aft of the moment reference center. By 10^o, the vortex system appears to have progressed up the LE to a point where the forward moving center of pressure causes a pitch-up moment. The pitch-up point can also be recognized in the C_A curve as the α for which the LE separation gradient is greatest - which produces increased vortex lift at the expense of suction over most of the LE.

Figure 15 shows oil flow visualization pictures of the right-hand upper surface at angles of attack of approximately 4^o, 9^o, and 15^o. At 4^o, the flow is fully attached over the wing except for a laminar separation bubble along the LE. This bubble is a region of slowly rotating low energy fluid, resulting from a local separation of the laminar BL in an adverse pressure gradient followed by reattachment as turbulent flow (inset "a"). The apex of the primary vortex system

ORIGINAL PAGE
BLACK AND WHITE PHOTOGRAPH

Figure 15.- Oil flow visualization pictures of right-hand upper surface of thin basic wing.

appears to be near the 40 percent semispan position at approximately 9° when the wing is approaching the point of pitch up. The vortex core trajectory in the plan view is indicated by the locus of inflexion points in the herringbone-type pattern formed in the oil flow. Inset "b" shows a typical cross-section of the vortex system normal to the LE and viewed from the rear. The large primary vortex rotates in a counter-clockwise direction (clockwise on the left wing), with a smaller secondary vortex rotating in the opposite sense (inset "c"). By $\alpha \approx 15^{\circ}$, the vortex system has progressed close to the wing apex; the flow pattern then stabilizes with further increase in α as indicated by the regularity of the curves in figure 14.

A comparison of the present measurements with theory (ref. 23) is contained in figure 16. The theory allows for intermediate values of LE suction between 100 percent suction (fully attached or potential flow) and 0 percent suction (fully separated flow). This comparison of drag-due-to-lift ($C_D - C_{D_o}$) data for the blunt LE confirms that the LE flow is attached up to approximately 8° angle of attack as previously noted in the C_N and C_A characteristics. Between 8° and 15°, there is a rapid loss of LE suction that finally settles along the 10 percent suction curve - which is expected of a blunted LE. The data for a wedge LE also shows the expected (smaller) residual suction arising from the forward sloping surface behind the sharp LE.

6.2.3 Thick Basic Wing (Test 63, Run 18)

This run provided the baseline data for evaluating the LE devices tested on this wing. The model was prepared in the same manner as described in the previous section except that the LE slots were flush

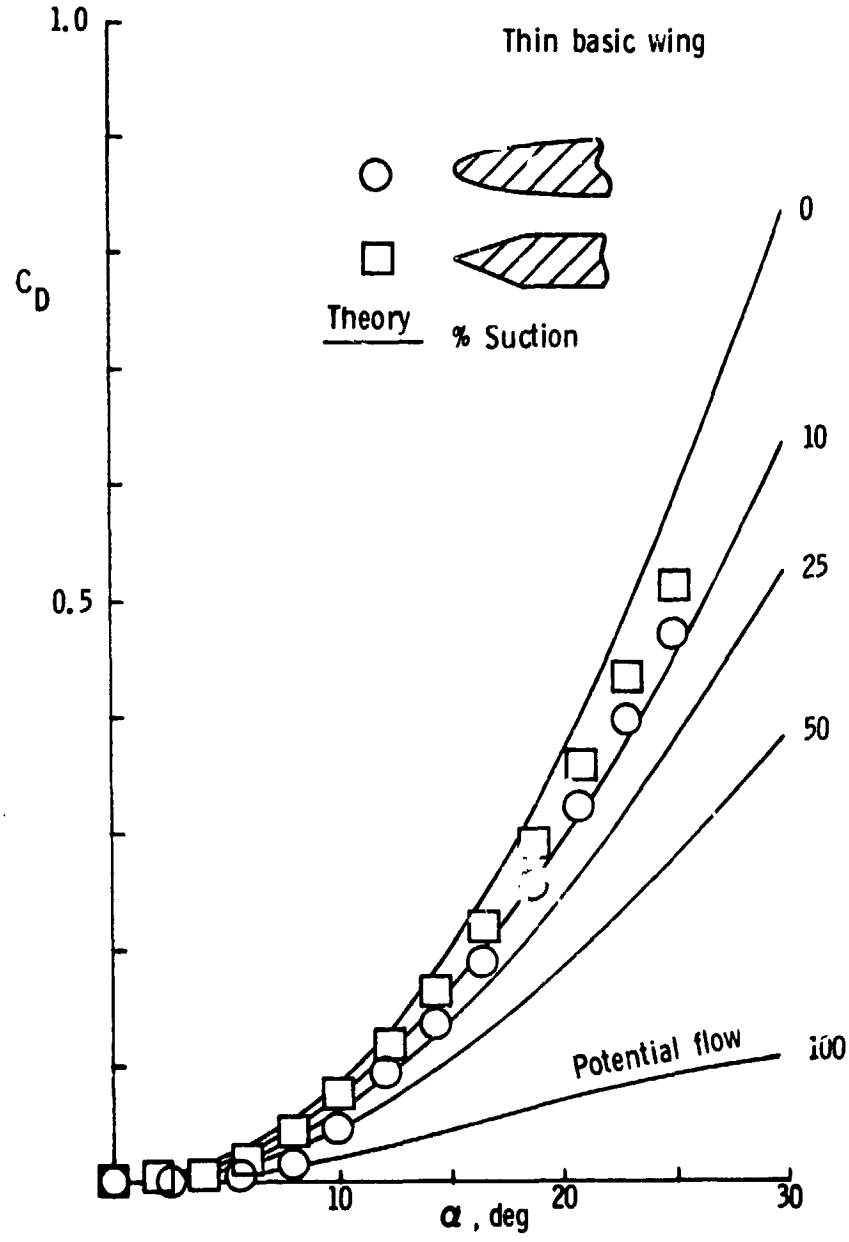

Figure 16.- Comparison of experimental data with theory for the thin basic wing.

filled with shaped aluminum inserts. Balance and surface static pressure measurements as well as mini-tuft pictures were taken at each data point. The results are presented in figures 17 through 19.

Figure 17 presents the balance measurements. A negative C_N and positive C_m at $\alpha = 0^o$ is believed to result from asymmetry in the trailing-edge bevel (see fig. 2). LE separation and pitch-down occurred near 9^o and pitch-up at approximately 16^o as opposed to 8^o and 10^o, respectively for the thin delta wing. It was expected that the larger LE radius of this wing would maintain attached flow to a higher α than on the thin wing, but to delay the pitch-up angle by as much as 7^o requires additional explanation.

The flow visualization pictures (fig. 18) for $\alpha = 16^o$ show that the primary vortex has reached the vicinity of the wing apex. Although the mini-tufts lack the degree of resolution afforded by the oil flow, both the visualization techniques show the main features of the surface flow pattern, e.g., attachment and separation lines, outflow under the primary vortex, and the position of the vortex system relative to the LE. In addition, the oil pattern shows local regions of high shear outboard of each LE slot location. Evidently, the disturbance produced by the slots (even though plugged flush) was sufficient to promote locally separated flow with subsequent reattachment. This contention is supported in reference 10 which reported that seemingly minor LE disturbances had significant effect on the LE suction characteristics of a blunt delta wing. Thus, the progress of LE separation towards the wing apex with increasing α is slowed resulting in a delayed pitch-up. More importantly, the above effect would be expected to improve the high α

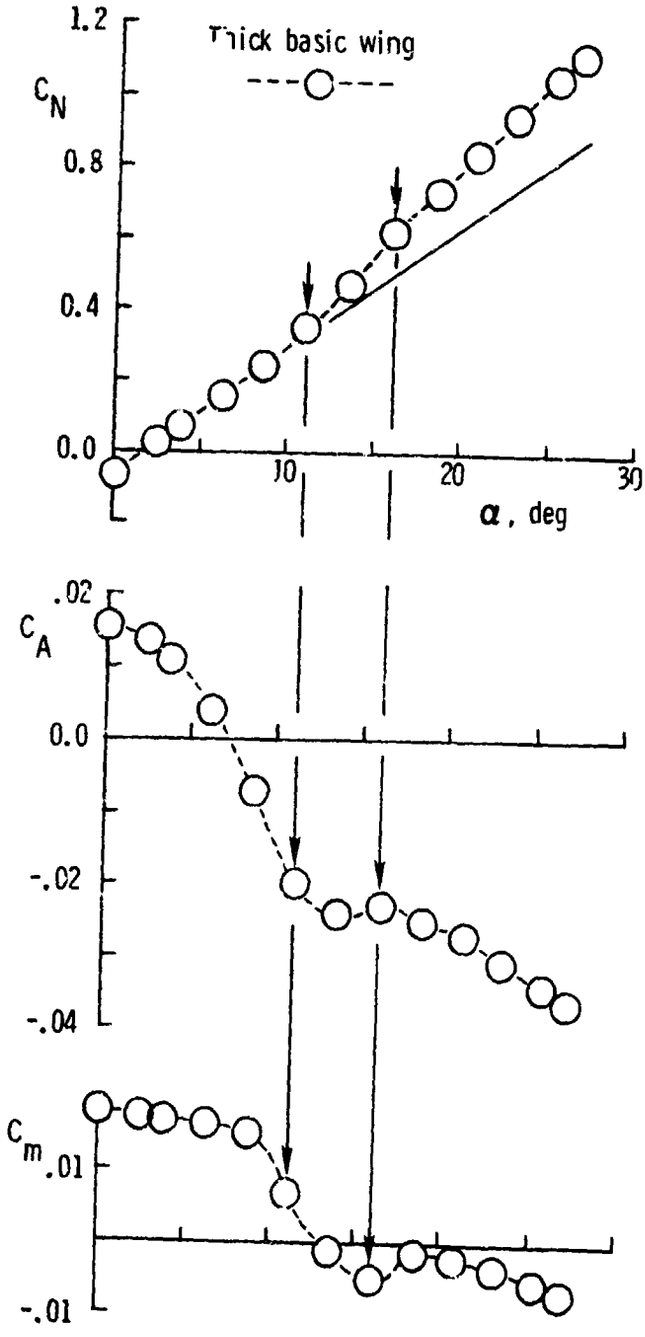

Figure 17.- Aerodynamic characteristics of the thick basic wing.

Figure 18.- Flow visualization pictures for the thick basic wing at $\alpha = 16^{\circ}$.

drag characteristics of the basic wing, with the result that the assessed performance of LE devices would be conservative. To provide more understanding of the LE thrust distribution, the surface static pressures around the right LE were integrated as discussed in section 5.2.

In figure 19, the pressure derived LE thrust coefficients (local and total) is compared with the balance axial force coefficient ($\Delta C_{A,BAL} = C_A - C_{A_o}$). The figure at the top shows a typical thrust distribution. There is generally close agreement between balance and pressure data (lower two curves) to approximately $\alpha = 13^o$ at which point the balance data indicate an axial force increase that is not reflected in the pressure data. This situation indicates that the balance sensed a body-axis force that occurred other than at the LE and could be attributed to the onset of trailing-edge separation. The pressure data show a sudden loss of LE thrust near $\alpha = 19^o$ which can also be noted in $C_{T,LCL\ PRESS}$ at $\eta = 0.45$ and 0.70. The local thrust distribution highlights several interesting aspects of the wing tested.

It can be noted that while $C_{T,TOT\ PRESS}$ is zero at $\alpha = 0^o$, the local values show a scatter at the origin which continues to about $\alpha = 14^o$. An unrealistic negative thrust noted at $\eta = 0.20$ and 0.33 is perhaps due to the limited number of orifices near the stagnation line. The importance of this figure is that the best position for LE drag-reduction devices can be determined, e.g., the departure of $\Delta C_{A,BAL}$ near $\alpha = 14^o$ would probably be delayed by locating a device near $\eta = 0.82$ (to decrease slope) and $\eta = 0.45$ (to increase slope).

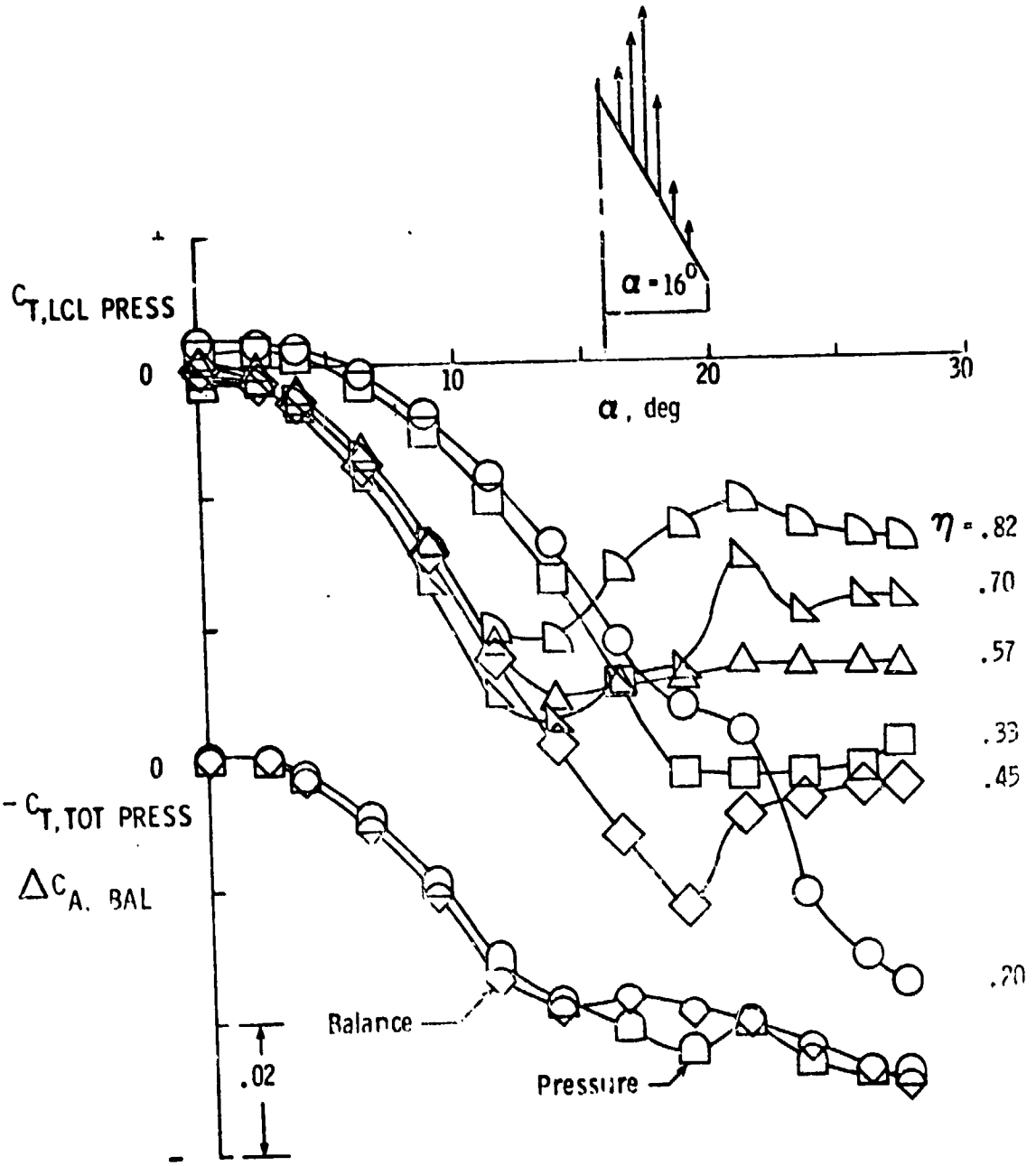

Figure 19.- Leading-edge thrust coefficients for the thick basic wings.

6.3 FENCES

6.3.1 Geometry

A total of seven different fences were evaluated with respect to variation in height and length. (See fig. 3 for fence dimensions.) Comparisons were made between the different geometries to determine the capability of each fence to delay the onset, or reduce the severity, of LE separation as indicated by the departure of the axial-force coefficient curves from the initial parabolic shape and from the basic wing data. The results are presented in figures 20 and 21.

Figure 20 (upper C_A graph) shows a height comparison between fences that are at the 75 and 87.5 percent semispan (η = 0.75 and 0.875) which project ahead of the thin wing LE. The F1-fence configuration indicates slightly less drag than F2 (of twice the height) at angles of attack below 10^o. This would be expected from considerations of skin friction drag of the fences. In the mid α range (10^o to 20^o), both fences indicate a gradual LE separation starting at $\alpha_D = 8^o$, the fence with larger height appearing to have a slight drag advantage.

The last two C_A graphs in figure 20 show height comparisons with fences (F3 and F4) that are flush with the wing LE. The data show the same trends as in the previous graph.

The results of the height comparisons would indicate that for the fence geometries evaluated, there was little or no effect noted in the test α range and that the height parameter is not a driving design consideration. A logical question would be, what is the minimum height required to produce an improvement over the basic wing characteristics? The significant effects noted with filled-in slots in comparison with

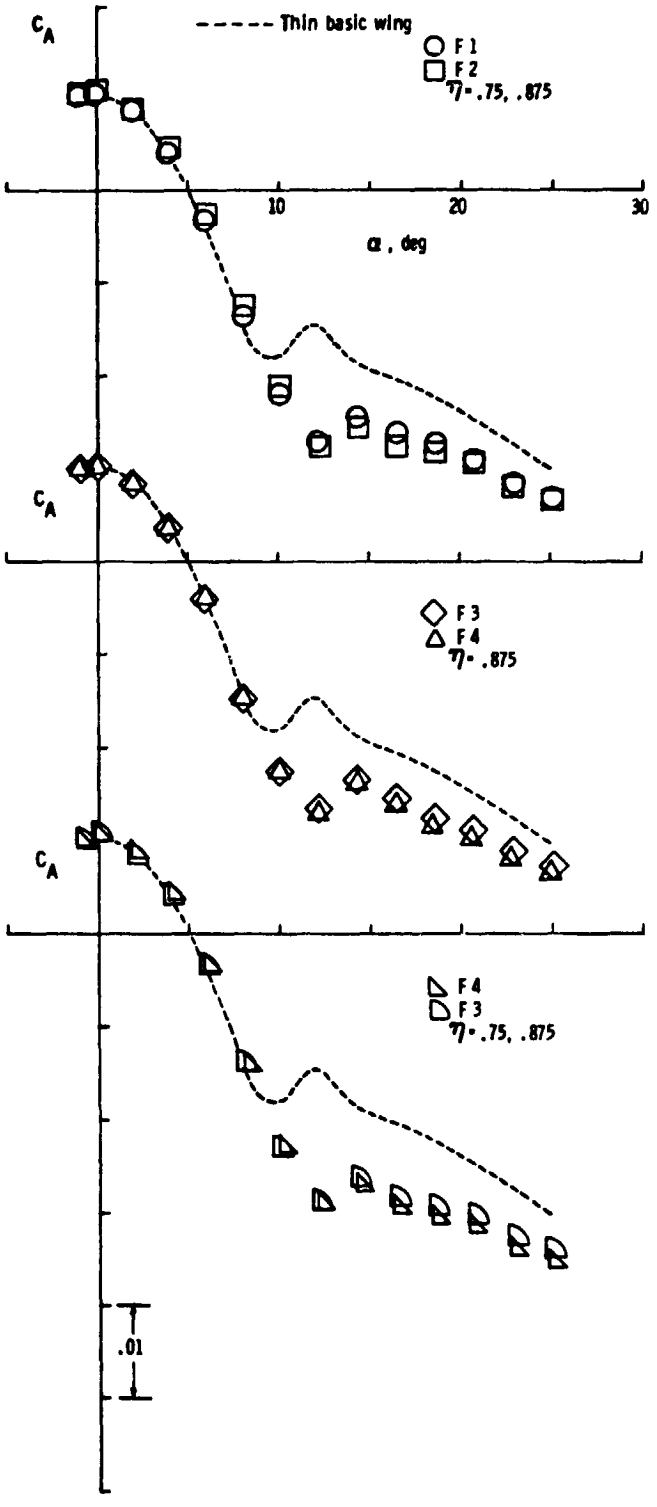

Figure 20.- Effect of fence height.

clean leading edges (section 6.1.6) would suggest that the minimum effective fence height may be very small indeed. However, the question of minimum height and also a chordwise variation in height require further study.

The second fence geometric variable evaluated was the chordwise length downstream of the wing LE including projection ahead of the wing LE. The upper C_A graph in figure 21 shows a comparison between single fences of four different lengths located at $\eta = 0.625$ on the thin delta wing. Close agreement of data is found up to $\alpha_D \approx 8^\circ$, but differences can be noted beyond. Near 12°, the F2 fence (which projects ahead of the LE) shows a relatively sudden loss of suction while the flush-mounted F4 fence and its derivative F7 (upper surface only) indicates a less severe loss of effectiveness. The longer flush-mounted F6 fence delays this effect to approximately $\alpha = 16^\circ$ and would appear to have the best performance as can be seen by the relative magnitudes of the curves. Note that a comparison of the F4 and F7 data indicates that following the onset of separation, there is some advantage to having the fence extend over both the upper and lower surfaces.

Figure 21 (center C_A graph) presents a length comparison for two fences of smaller height, F1 (projection ahead of wing) and F3 (flush mounted), which are located at $\eta = 0.75$ and 0.875. In the α range 10° to 20°, the flush-mounted fences appear to have retained slightly more LE suction. This advantage may be expected to improve with the addition of a third fence at say $\eta = 0.625$. This expectation is supported in the last graph.

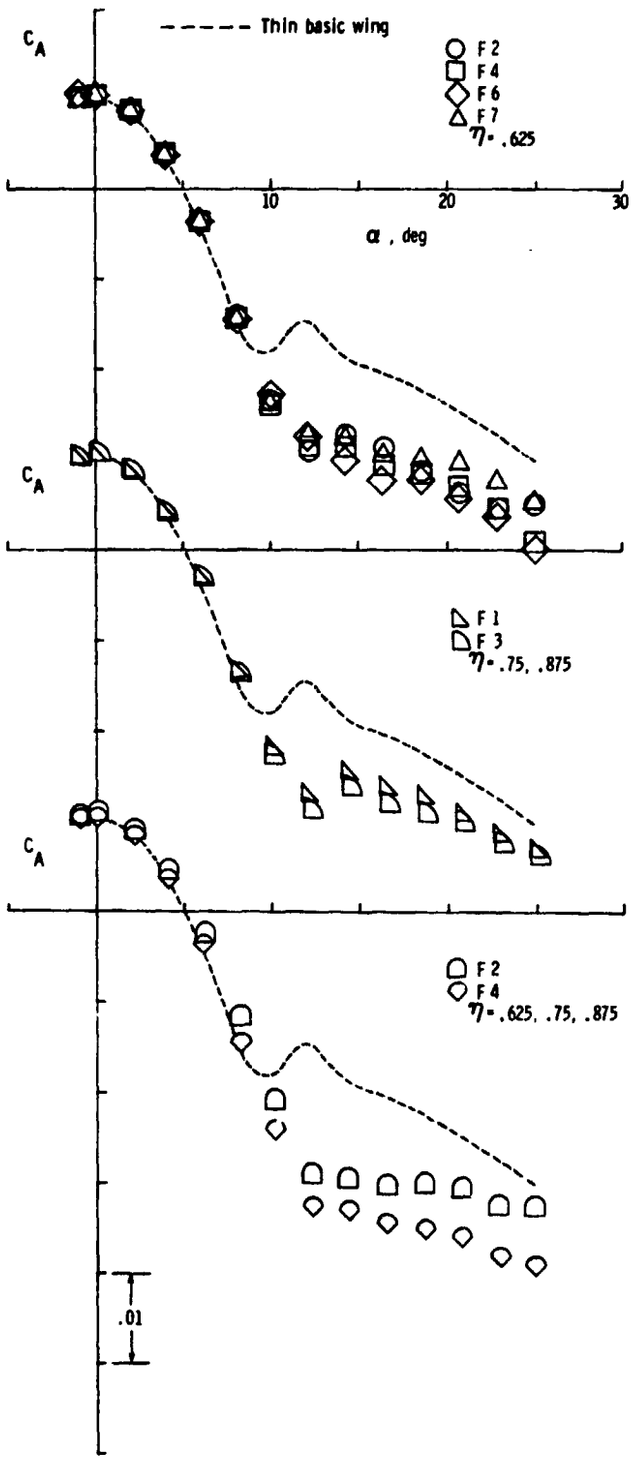

Figure 21.- Effect of fence chordwise length.

The bottom C_A graph in figure 21 contains data for three fences of F2 and F4 type, located at η = 0.625, 0.75, and 0.875. It is readily apparent that flush-mounted fences (F4) (having less wetted area) produce less drag at low angles of attack and are more effective in maintaining LE suction beyond α_D than those which project ahead of the wing (F2). This figure also emphasizes the effect of spanwise position as well as multiplicity of devices as will be discussed in the next two sections.

The above comparisons establish that fence length is an important design parameter, although projection ahead of the LE appears unwarranted. Fences that extend further aft on the wing seem to have better drag reduction capabilities, as well as those that project both above and below the LE. Since this study was concerned only with LE flow control, no investigation was made of fences extending further downstream on the wing surface which may have other advantages.

6.3.2 Spanwise Position

Two series of runs were conducted to evaluate a single fence at different semispan positions. Of particular interest was the position effect of specific fence shape on the onset of LE separation and the axial-force departure characteristics following separation. Comparative results of the F2 and F4 fences on the thin and thick wings, respectively, are presented in the next figure.

Figure 22 (upper C_A graph) shows the position effect for the F2 fence which indicates only minor variations in drag at low angles of attack and a gradual departure from the initial parabolic attached flow curve ($\alpha_D \approx 8^o$). Near 12^o, a severe loss of LE suction is noted for all

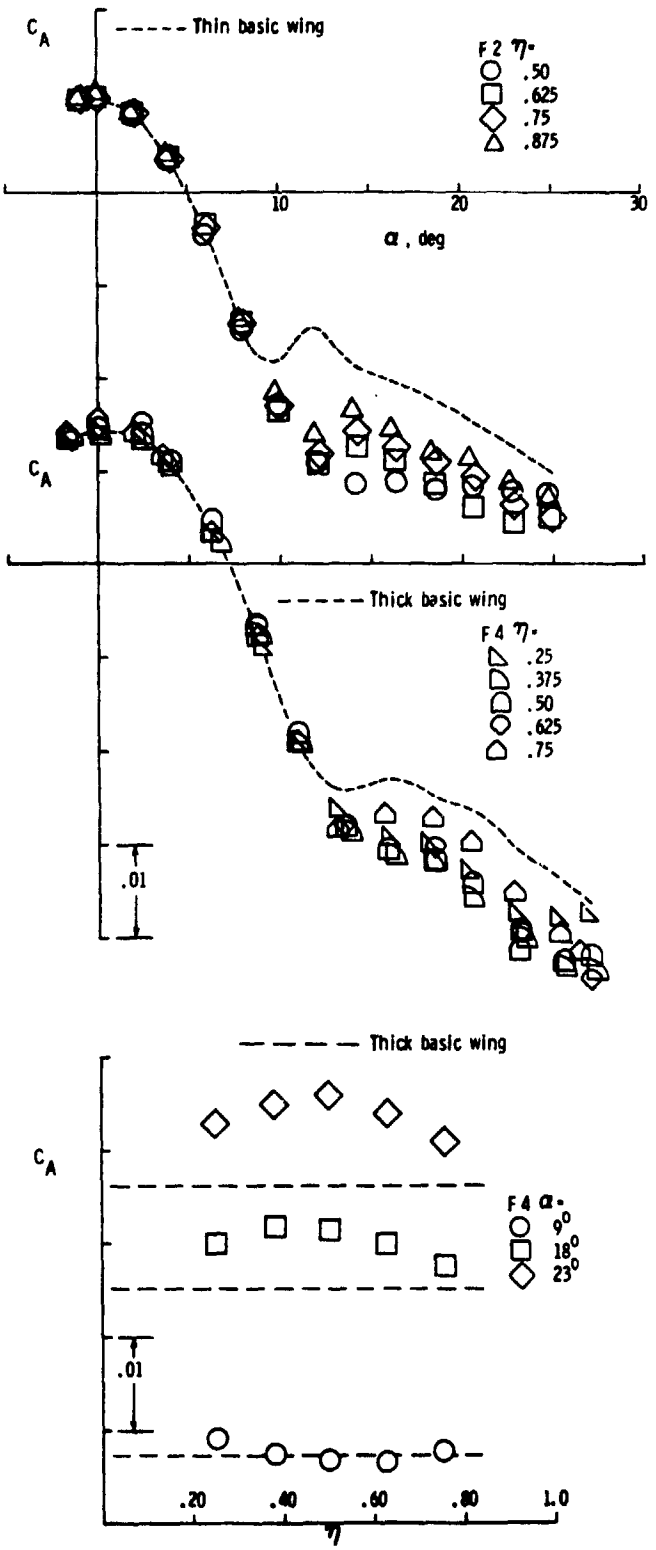

Figure 22.- Effect of fence spanwise position.

spanwise positions of the fence except at $\eta = 0.50$. Between $\alpha = 12^{\circ}$ and 18°, the $\eta = 0.50$ position retains the most suction which is relegated to the $\eta = 0.625$ position beyond 18°.

The second comparison of spanwise position effect was conducted on the thick wing using the F4 fence (fig. 22, center C_A graph). The data indicate separation onset at $\alpha \approx 9^{\circ}$ for all spanwise positions, and that only for $\eta = 0.75$ does a severe suction loss occur (near 13°). Beyond 15°, the fence appears to be equally effective at either $\eta = 0.375$, 0.50, or 0.625.

To better appreciate the position effect, the last graph in figure 22 shows C_A data versus percent semispan at three selected angles of attack. The horizontal dashed line represents the axial-force coefficient for the thick basic wing (no devices) at the three angles of attack. At $\alpha = 9^{\circ}$ with attached LE flow, there is evidently no fence effect, but at $\alpha = 18^{\circ}$, the $\eta = 0.375$ position shows the best performance (and at $\eta = 0.50$ at $\alpha = 23^{\circ}$). If the curves are assumed to be smooth and continuous as shown in the figure, then the best position for a single set of fences can be selected with respect to α, e.g., $\eta = 0.40$ for $\alpha = 18^{\circ}$ and $\eta = 0.50$ for $\alpha = 23^{\circ}$.

To summarize, a single pair of fences did improve the post-separation aerodynamic performance of the wings tested. More specifically, a single fence on a spanwise-uniform semi-elliptic LE and a 60° delta planform, has the greatest drag-reduction capability when located near the 50 percent semispan position.

6.3.? Multiple

Multiple fence arrangements, which have been alluded to in earlier sections, will now be discussed. Two methods were used to evaluate the impact of the number and distribution of devices along the LE: (1) the number of fences were gradually increased, starting with one fence near the tip and adding fences one at a time progressively inboard; and (2) by changing the semispan distribution of a fixed number of fences. Axial-force comparisons were made to determine the best number and distribution for the different fences.

Figure 23 presents C_A data on one, three, and five pairs of small F5 fences (upper graph). It can be noted that increasing the number of devices increased the drag at angles of attack below α_D, but the departure is more gradual for all the configurations. Also, with increasing number of fences, there is a trend towards delayed loss of LE suction to higher angles of attack, as may be inferred from the C_A data between 10^o and 20^o. Note that the single pair of fences at $\eta = 0.75$ show more drag than the basic wing. Although not presented, the pitching-moment data of the configuration with five pairs of fences indicates pitching-type instability at the same α for which a severe loss of LE suction occurs (i.e., 18^o). Beyond 20^o, the data tend to merge with each other as well as with basic wing data, which indicates that with fences as small as the F5 type, the LE flow is no longer influenced to any significant extent.

The center C_A graph in figure 23 also shows that increasing the number of fences (progressively inboard) improves the performance in a progressive manner. It can be pointed out that when the third set of

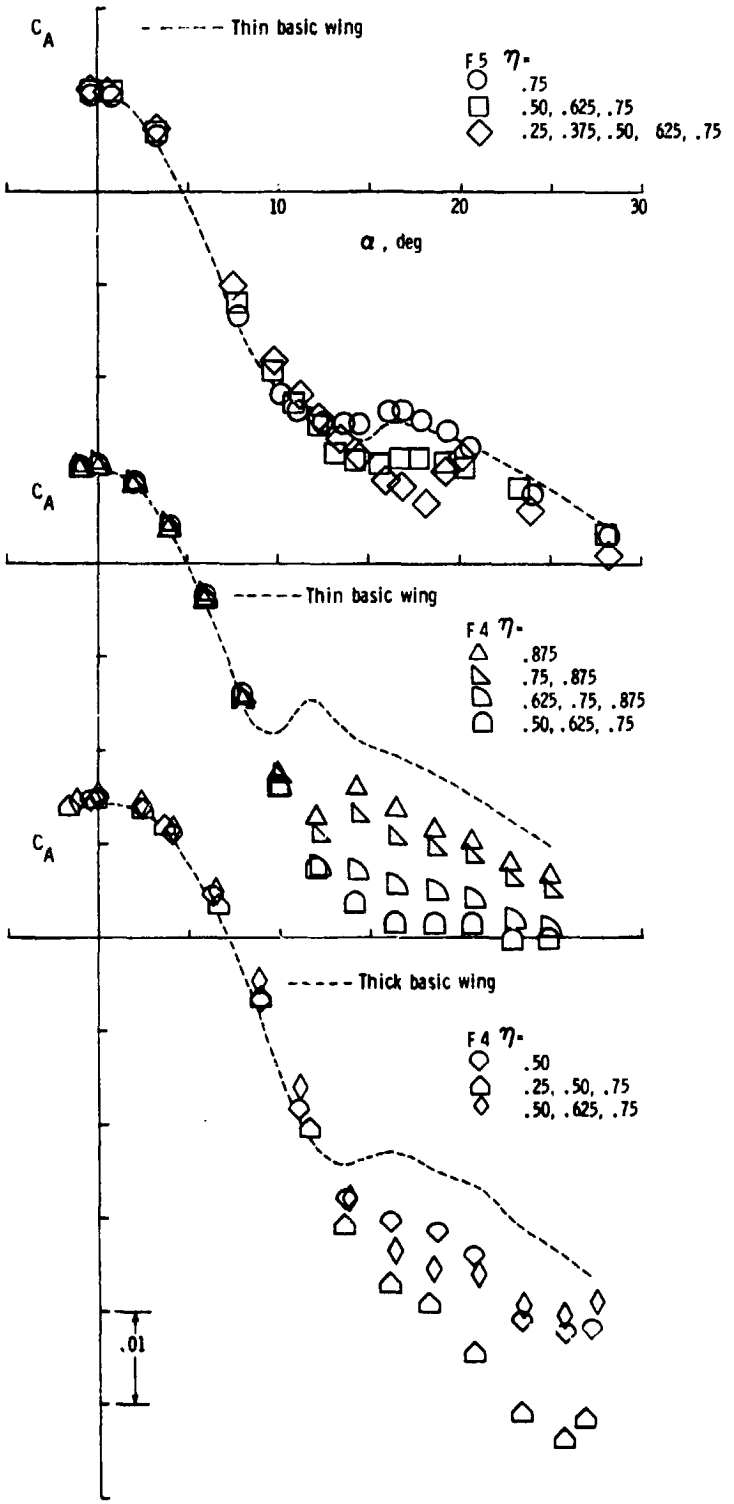

Figure 23.- Effect of multiple fences.

fences were added, the severe suction loss at 12° was eliminated, leading to substantial gains. The interaction between the multiple fence effect and the position effect is shown by the improved performance when the pair of fences were moved from $\eta = 0.875$ to $\eta = 0.50$, as suggested in the previous section.

The last graph in figure 23 shows the C_A data for the same F4 fence, but installed on the thick delta wing. In this case, one set of fences at $\eta = 0.50$ is found to be almost as effective as three sets located at $\eta = 0.50$, 0.625, and 0.75. From a comparison of the same configuration on the thin wing (top C_A graph in fig. 25), it would appear that LE radius had little effect on the performance of multiple fences.

Another factor that has a bearing on the effectiveness of multiple fences may be termed the proximity effect. This can be seen by the C_A data for three pairs of F4 fences at $\eta = 0.50$, 0.625, 0.75, and $\eta = 0.25$, 0.50, and 0.75 with the latter distribution being more effective (bottom graph in fig. 23). It is apparent that the distance between adjacent fences is an important parameter; however, the present data are insufficient to reach firm conclusions.

To summarize, the retention of LE suction and corresponding drag-reduction capabilities of fences can be greatly enhanced by multiple arrangements. The optimum number and distribution along the LE, including the minimum distance between fences, are important parameters which require further investigation.

6.3.4 Leading-Edge (LE) Radius

The difference in thickness of the two leading edges tested offered the opportunity to investigate the impact of LE radius on the drag-reduction capabilities of the fences. The thick wing (which had twice the LE radius of the thin wing) presented more forward facing surface area relative to the wing reference area, and it would, therefore, be expected that beyond α_D the vortex induced suction would provide greater thrust than on the thin wing. It also had a more gradual curvature around the LE, and so it would be expected to retain LE attached flow to a higher α. However, because of certain differences in the models (figs. 1 and 2) and the facts covered in section 6.1, the following discussion offers, at best, a limited insight into the LE radius effect.

The upper C_A graph in figure 24 presents the data for a single pair of F4 fences located at 50 percent semispan ($\eta = 0.50$). The dashed and chain-dot lines represent basic wing data. The thick wing shows a larger drag at $\alpha = 0^o$ which was due to increased housing drag and trailing-edge separation. Prior to the onset of LE flow separation, the two sets of data can be noted to diverge slightly which is probably an aspect ratio or geometric effect (AR = 1.9 and 1.6 for the thin and thick wings, respectively). The opposite is true beyond α_D where the data points converge as the primary vortex system advances to the wing apex. In the mid α range (12^o-22^o), both sets of data are relatively constant and of nearly equal magnitudes on a ΔC_A basis, thus the effect of LE radius would not appear to be a factor in this case.

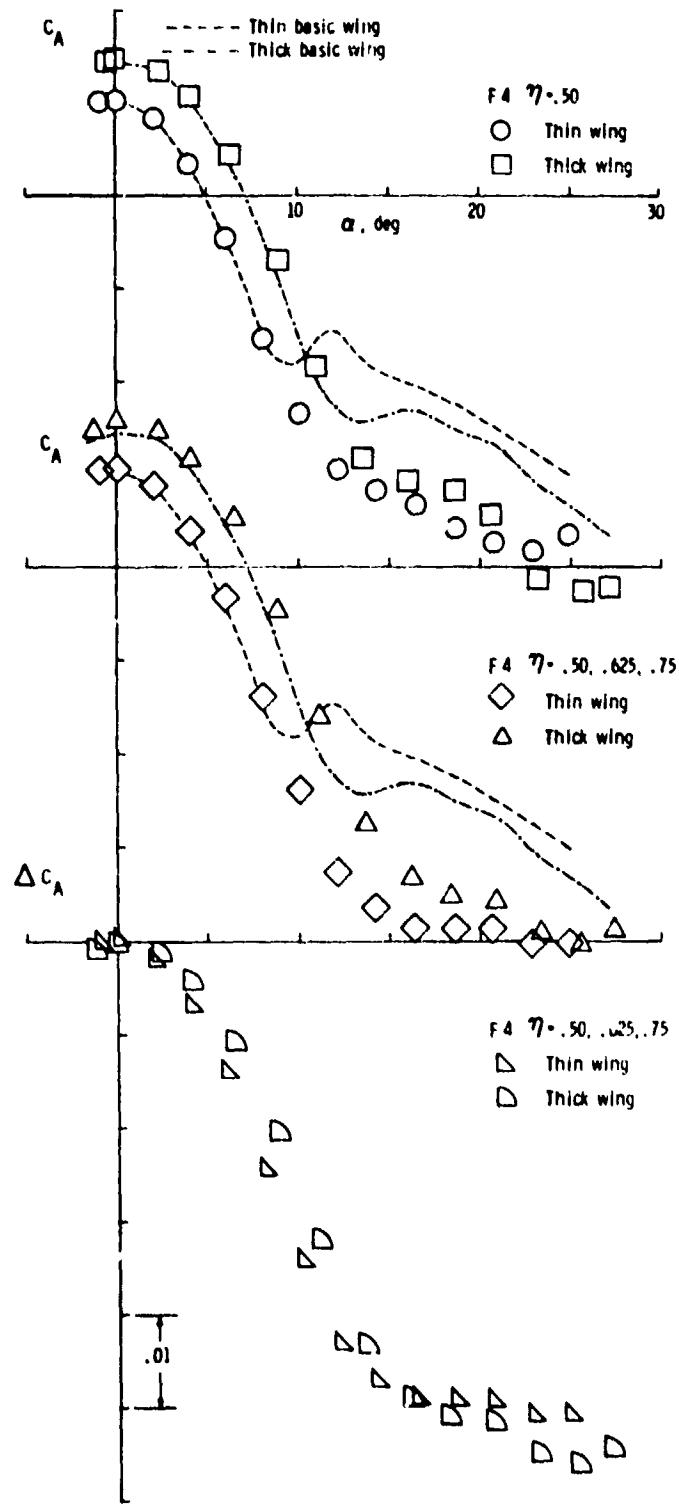

Figure 24.- Effect of leading-edge radius on fence performance.

The center C_A graph in figure 24 presents the data on three pairs of F4 fences located at η = 0.50, 0.625, and 0.75. While the multiple effect is apparent (see previous section), the trends are the same as for a single pair as can be noted in the last graph where the data are presented with the $\alpha = 0^o$ drag removed ($\Delta C_A = C_A - C_{A_o}$). The same divergence and convergence near 9^o α can be noted as well as a crossover near 16^o where the thick wing assumes a slight suction advantage.

It would appear from the limited data presented that LE radius had relatively little effect on the performance of the fences tested. However, this conclusion can only be justified by additional research.

6.3.5 Best Performance and Flow Mechanisms

The F4 fence evaluated on the thin wing provided the best drag-reduction capability of the fences tested. As previously discussed, a stronger effect of the fence was to be expected on the thin wing which experienced earlier LE separation and a greater loss of suction than the thick wing. Fence configurations along with their respective performance (PD and C_A) at $\alpha = 12^o$ and 15^o are presented in Table 2. Two configurations will be discussed; a single pair of F4 fences at η = 0.50 and three pairs at η = 0.50, 0.625, and 0.75. To further support the discussion, static pressure data collected from the thick wing will be presented.

The aerodynamic characteristics (C_A and C_m) and the drag-reduction parameter (PD) are presented in figure 25. The dashed line represents the experimental data for the basic wing. As indicated in the C_A graph at the top, the multiple pairs have slightly more drag in

the low α range as opposed to the single pair. Following $\alpha_D \approx 8^\circ$ on the basic wing, the data gradually converge to about 10°, and subsequently, diverges with the multiple pairs showing greater drag reduction. These trends can also be noted in the center PD graph where the multiple pairs indicate almost 27 percent drag reduction at $\alpha \approx 12^\circ$.

Table 2

Summary of Fences Tested on Thin Wing

	25.0	37.5	50.0	62.5	75.0	87.5	C_A @ 15°	PD @ 12°	Run #
BW							.0195	-----	51
F						●	.0231	-15.6	17
					●	●	.0248	-20.5	
F 2			●				.031	-6.1	36
				●			.0276	-2.0	39
					●		.0256	-11.4	38
						●	.0230	-6.0	40
					●	●	.0250	-11.1	50
				●	●	●	.0298	-25.1	37
F 3						●	.0237	-19.7	43
					●	●	.0266	-23.6	53
F 4			●				.0233	-11.0	37
				●			.0288	-14.7	46
						●	.0250	-19.1	41
					●	●	.0274	-23.6	51
			●	●	●		.0247	-6.7	38
				●	●	●	.0281	-26.6	44
F 5						●	.0233	-18.4	16
	●	●	●	●	●	●	.0281	-14.7	45
F6				●			.0260	-19.4	39
F7				●			.0245	-13.5	42

It was pointed out earlier that fences have been traditionally used as a fix for longitudinal instability. This effect can be noted in the C_m graph at the bottom of figure 25 where both fence configurations have favorably changed the basic wing characteristics (severe pitch-down between approximately 6° and 10° α followed with instability) by reducing the slope and delaying pitch-up by as much as 4°. It is interesting to note that the single pair delayed pitch-up the most.

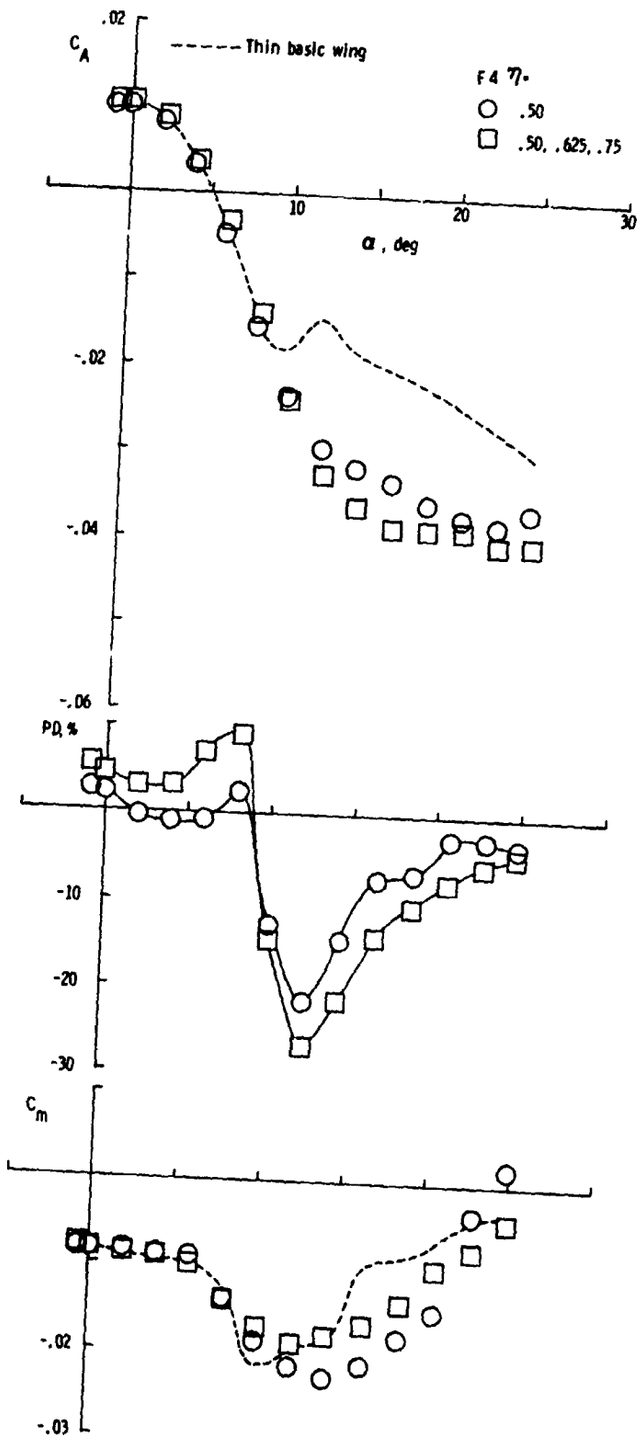

Figure 25.- Best fence performance.

It has been shown that multiple fences provide greater drag-reduction capability than a single fence; however, the discussion of flow mechanisms here will focus on a single fence (η = 0.50) positioned on the thick wing with the understanding that each fence would produce similar local effects in a multiple configuration. Below $\alpha = 9^{o}$, the LE flow is fully attached with or without a fence as can be noted by the parabolic shape of the C_A curves in figure 25 (thin wing) and figure 26(b) (thick wing), as well as by the linearity of the C_N curve in the latter figure.

By $\alpha = 16^{o}$, a major change in the flow has occurred - substantial increase in thrust outboard of the fence is indicated in the C_p and $C_{T,LCL\ PRESS}$ distributions (fig. 26(a)). It is believed that the LE region just outboard of the fence acts as a "pseudo apex" where both the reduced suction peaks and pressure gradients allow the flow to remain attached to the highest angles of attack. Therefore, the further advance of LE separation is arrested. This shielding effect can be noted downstream of the fence in the η_s versus α plot (fig. 26(b)) where the onset of separation has been delayed by several degrees. The same plot also suggests that the area inboard of the fence acts as a "pseudo tip" in that the onset of flow separation occurs earlier due to an increased pressure gradient. This can be seen in the upper surface C_p distributions (η = 0.45) at $\alpha = 16^{o}$ and also at 21^{o} where the flow tends to stagnate as indicated by a higher constant pressure level with respect to the basic wing. The local thrust coefficient data at $\alpha = 16^{o}$ and beyond, demonstrate thrust enhancement outboard of this single device, while there is only a localized loss of thrust just inboard.

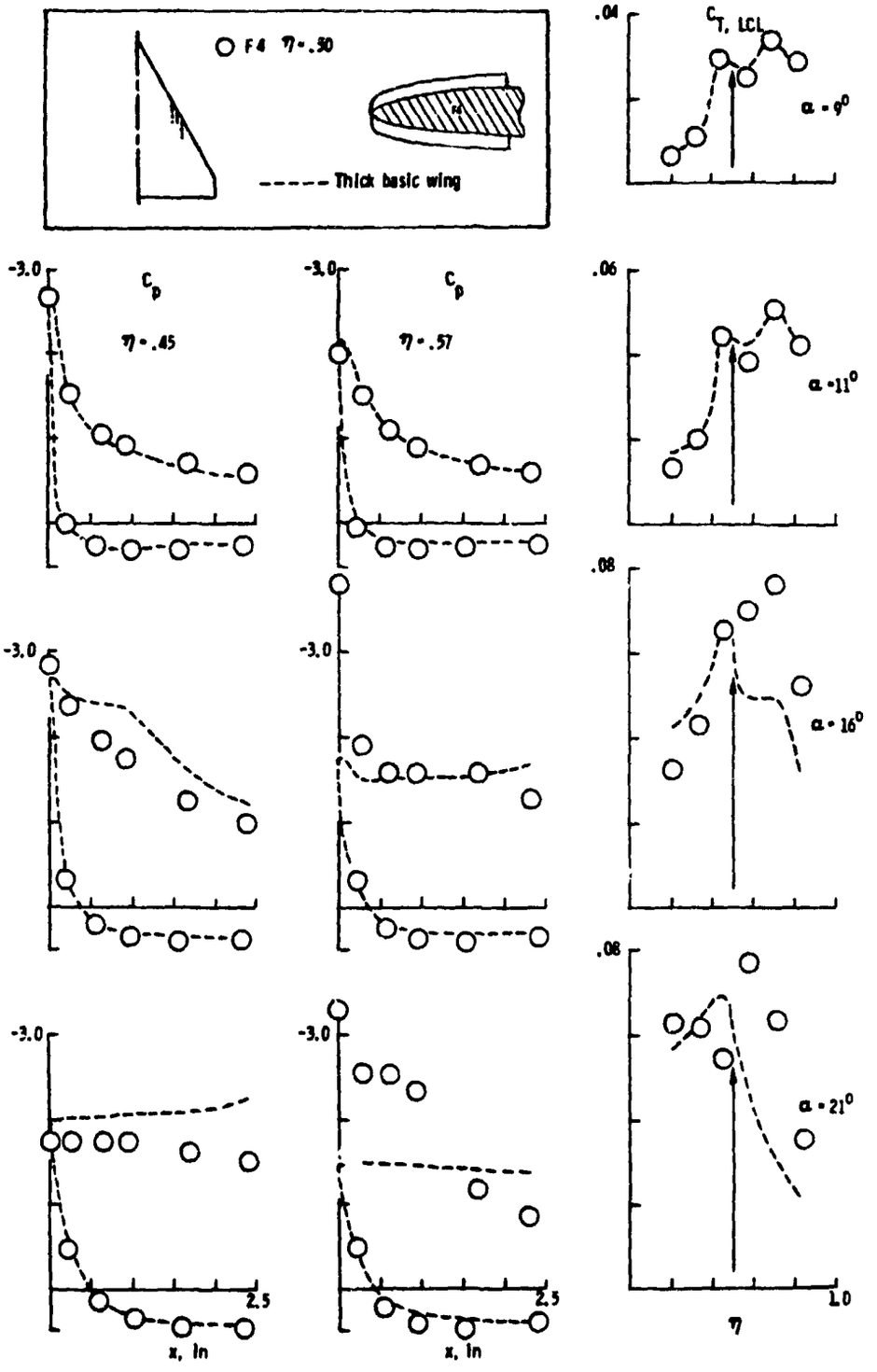

Figure 26(a).- Comparison of balance and pressure data obtained from the thick wing configured with fences.

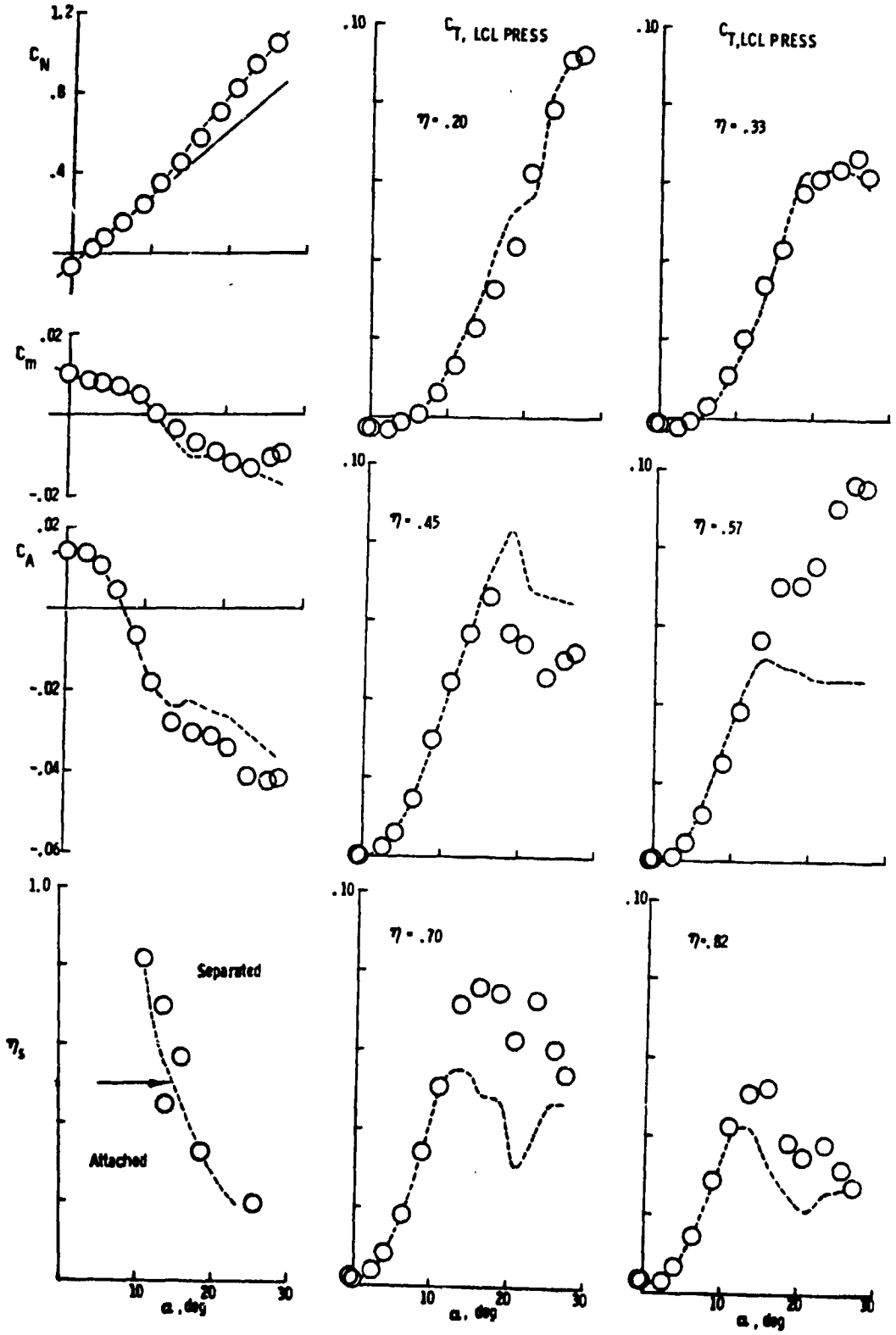

Figure 26(b).- Concluded.

These effects are confirmed in the oil flow visualization in figure 27 by the existence of two primary vortex systems, i.e., one emanating just outboard of the fence and the other near the wing apex. The conclusion is that the inboard movement of LE separation with increasing α is stopped on the outboard side of the fence, while another region of separation grows from the inboard side. The result is that the downstream vortex system acts on the blunt LE to generate greater levels of aerodynamic thrust as opposed to a single sheet vortex system which would be further inboard in this region (see inset fig. 27). It follows that the fence is effective in the compartmentation of the wing LE.

Another favorable aspect of this small device is its ability to improve longitudinal stability which is apparent in the C_m curve in figure 26(b). With the addition of the fence to the basic wing, pitch-up has been delayed by about 7^o ($\alpha = 16^o$ to 23^o) which is believed to be due to the interaction of the primary vortex system and the tip vortex. It is suggested that the primary vortex rotating in the same sense as the tip vortex, initially enhances the tip region thus creating additional lift augmentation leading to a pitch-down moment. As the angle of attack increases, the stronger LE vortex moves inboard diminishing the tip vortex and eventually displaces it from the tip region. The fact that the pitch-up α has been delayed by 7^o is attributed to a slower rate of movement of the outboard primary vortex towards the fence as compared to the primary vortex on the basic wing.

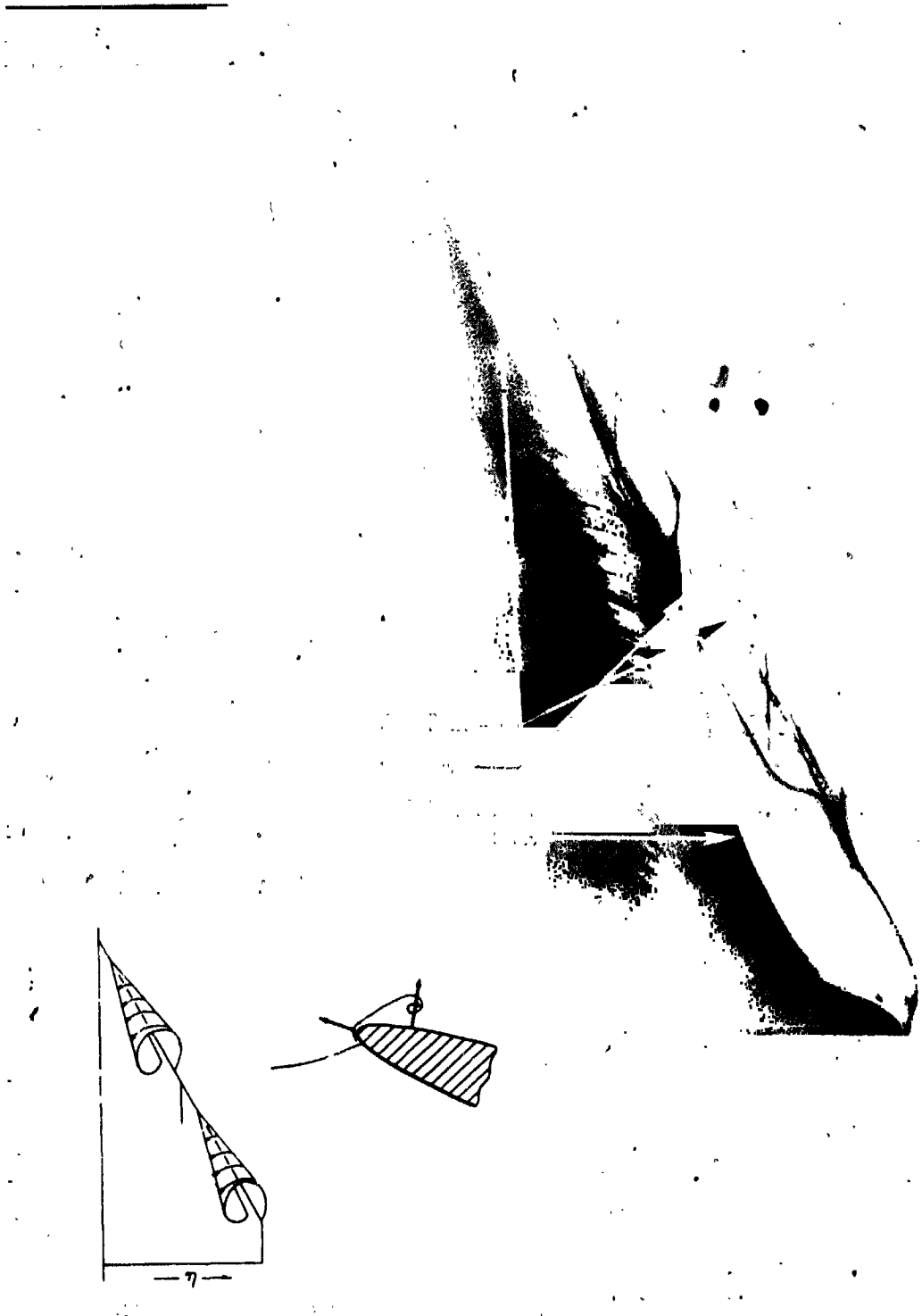

Figure 27.- Oil flow visualization picture of thin wing with F4 fence at the 50 percent semispan position ($\alpha = 16^{\circ}$).

6.4 SLOTS

6.4.1 Multiple

This device was evaluated in increasing numbers by removing the filler material, and thus exposing the slot to the LE flow. No attempt was made to alter the slot geometry in this experiment because these slots were also used to hold the fences and pylon-type vortex generators in place.

Figure 28 presents the C_A data (upper graph) for multiple arrangements of one, two, three, and six slots with the dashed lines indicating thin basic wing data. As would be expected, increasing the number of slots also increases drag at low angles of attack which can be attributed tc the internal wetted surfaces of the slot and also pressure drag on the vertical face at the rear of the slot. Beyond $\alpha_D \approx 8^o$, all of the slot configurations exhibit a more gradual loss of LE thrust, and by increasing numbers of active slots, better drag reduction performance was achieved. It should be noted that all four configurations show a sudden loss of effectiveness at about $\alpha = 16^o$ followed by a convergence to the basic wing near 21^o. The next section will discuss this characteristic.

6.4.2 Best Performance and Flow Mechanisms

It was pointed out in the preceding section that increasing the number of slots improved the higher α performance. This can be noted in Table 3 which contains information on slot configuration and performance.

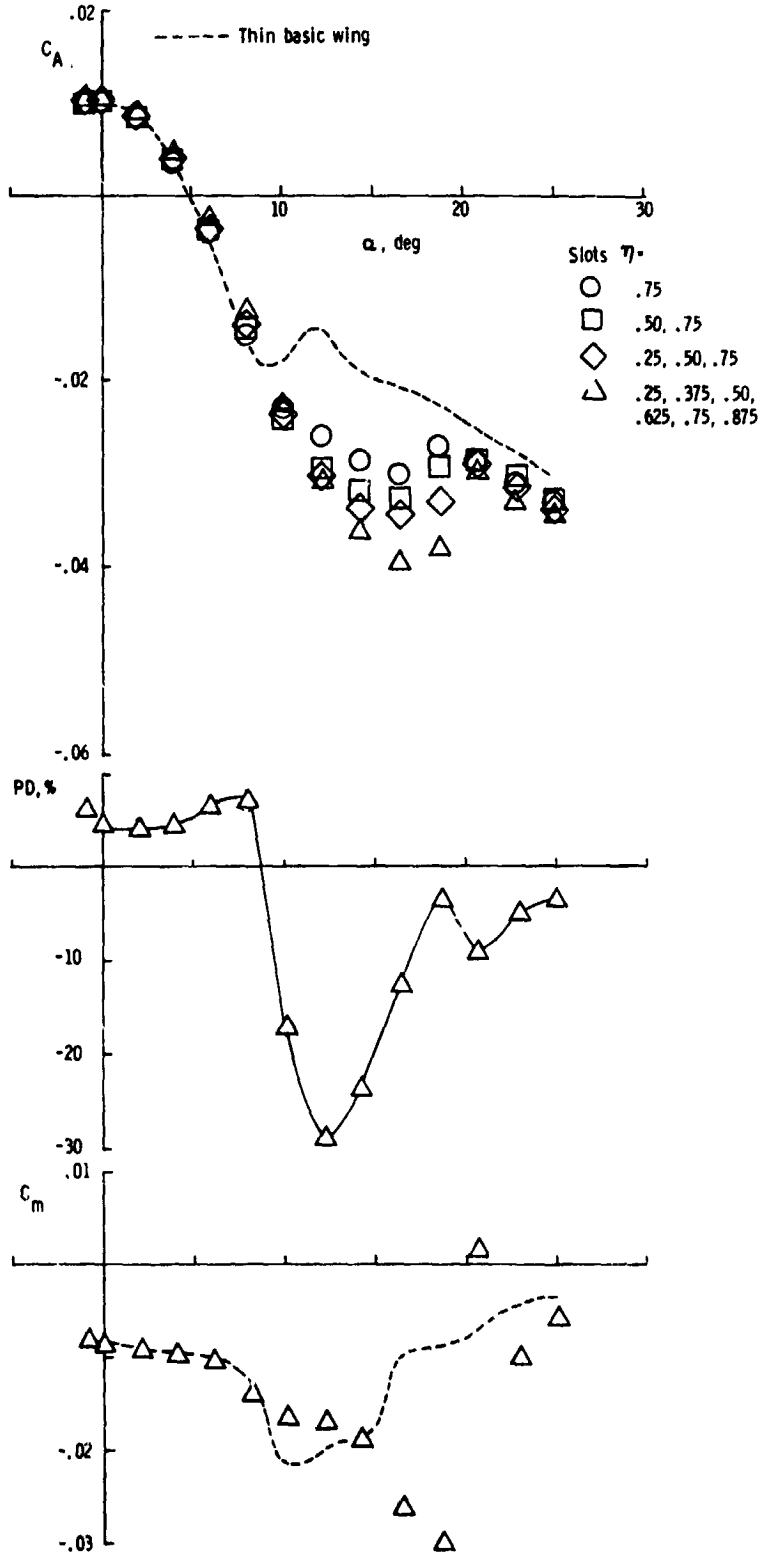

Figure 28.- Effect of multiple slots.

Table 3

Summary of Slots Tested on Thin Wing

	25.0	37.5	50.0	62.5	75.0	87.5	C_A @ 15°	PD @ 15°	Run #
BW							.0195	-----	57
S L O T					●		.0393	-15.4	50
			●		●		.0375	-23.4	51
	●		●		●		.0344	-20.4	5
	●	●	●	●	●	●	.0378	-28.3	54

Figure 28 contains the data for six slots in which the PD and C_A curves support the low-high α performance characteristics discussed earlier. The ability of this simple device (which was in no way optimized) to produce a 28 percent drag reduction is remarkable. The drag penalty at low angles of attack could possibly be alleviated by suitably shaping the internal contour of the slot, which might also improve the high α performance.

Another feature of the slot can be noted in the C_m curve where the pitch-up of the basic wing (at $\alpha \approx 10^\circ$) has been delayed to approximately 19° by the slots - however, the accentuated pitch-up after 19° is an undesirable feature. A fix for this problem will be discussed in Section 6.7.2.

The flow mechanisms associated with the slots will be discussed with reference to figure 29 where the data pertain to five slots on the thick wing. In figure 29(a), the diagram shows that pressure stations at $\eta = 0.57$ and 0.70 were selected to present C_p data at $\alpha = 16^\circ$, 18°, and 21°. The close agreement of the C_T distributions at $\alpha = 9^\circ$ indicates that the slots had no significant influence below $\alpha \approx 9^\circ$, except of course, for a slight drag increase. Also, the flow is still attached as can be seen in the C_N and C_A curves in figure 29(b).

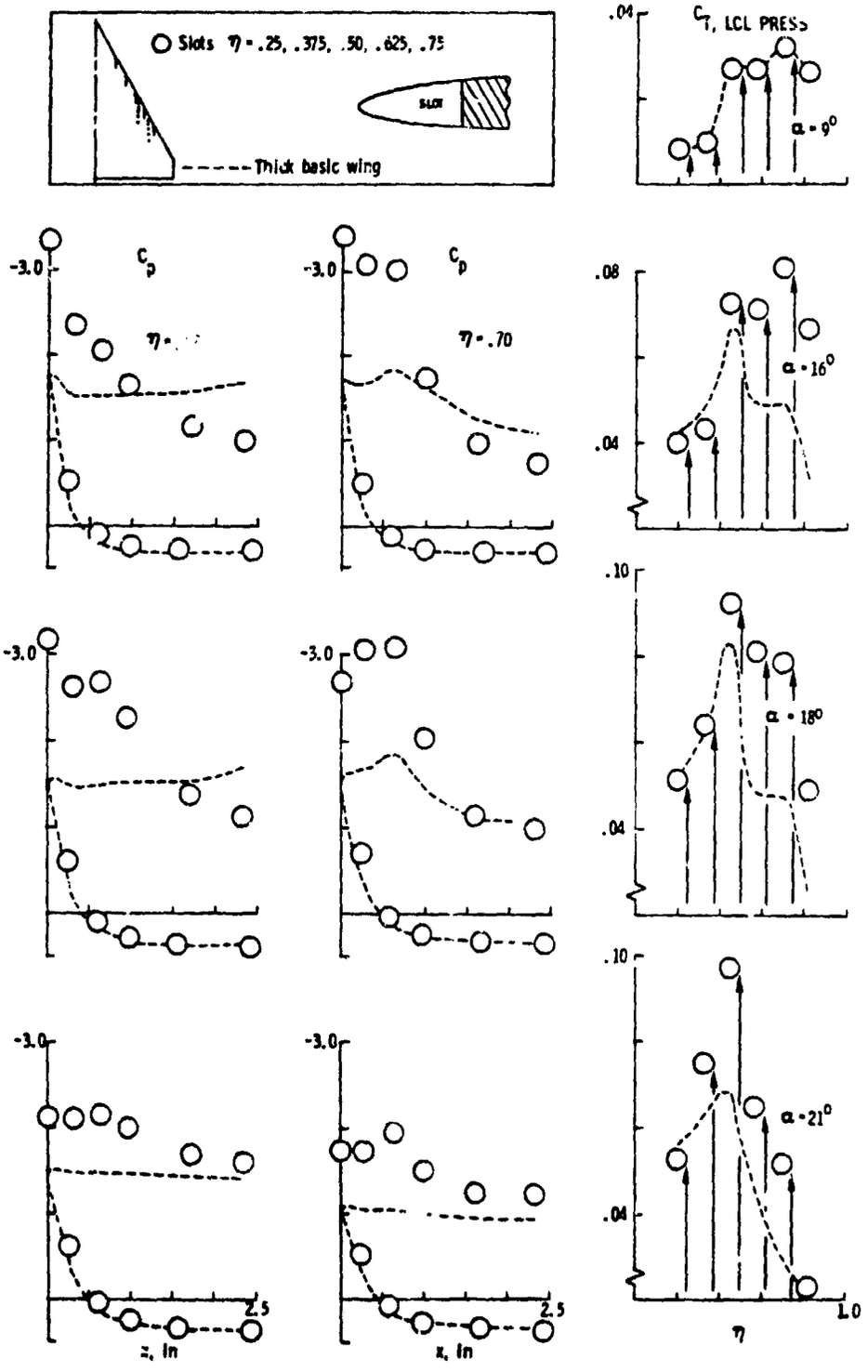

Figure 29(a).- Comparison of balance and pressure data obtained from the thick wing configured with multiple slots.

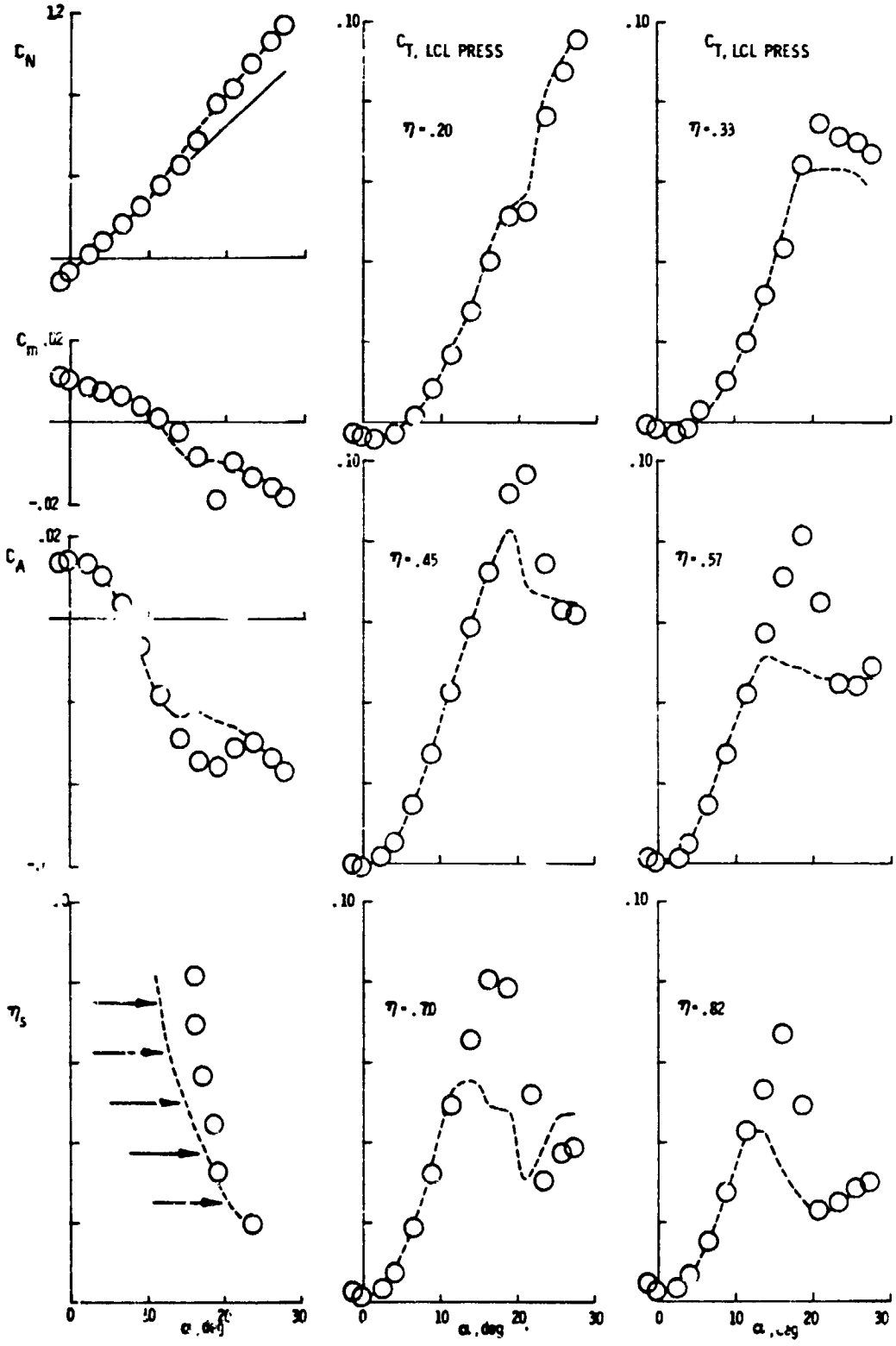

Figure 29(b).- Concluded.

At angles of attack greater than 9°, the effect of the slot becomes evident as was the case for the fence.

By $\alpha = 16°$, a significant increase in thrust can be noted (fig. 29(a)) on both sides of the slot (C_p and C_T distributions) as compared to the basic wing where the flow tends to stall. The same trends hold to $\alpha \approx 18°$, but by 21°, the improvement in thrust outboard of $\eta = 0.50$ diminishes and approaches that of the basic wing. This tendency can also be noted in the C_T versus α data in figure 29(b). It is suggested that the flow mechanism associated with the slot is a jet sheet resulting from the natural flow through the slot from the high pressure lower surface to the upper surface (see fig. 30).

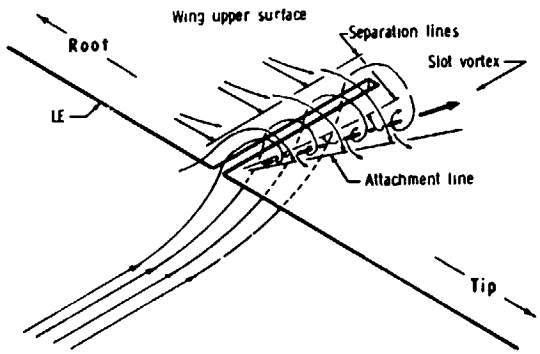

Figure 30.- Illustration of suggested slot flow mechanism.

The action of this sheet is to impede the spanwise flow of the boundary layer at relatively low angles of attack and, consequently, delay the onset of LE separation (say from 9° to 15°) which leads to vortex thrust enhancement as was the case of the fence previously described. However, when separation does occur, it spreads quite rapidly along the LE. This idea is supported by the η_s versus α data in figure 29(b) where the delay in the onset of separation can be noted.

The oil flow visualization picture in figure 31 ($\alpha \approx 12^{\circ}$) shows that a pair of discrete vortices are generated outboard of each slot as indicated by the dark shear areas. This would suggest that the primary vortex system has been segmented into a series of smaller systems that act primarily on the blunt LE. The chordwise shear areas indicate the presence of slot vortex systems, i.e., the jet sheets emanating from the slots roll up into vortices due to upstream vorticity considerations. Also the stagnated oil deposits along each side of the slots (light areas) indicate that the flow separates on the upstream side and is entrained in the vortex, while on the downstream side, the oil deposit results from an inboard flow due to reattachment. These visualizations support the previously described mechanism and shows how the slots are effective in compartmentation of the LE in a manner similar to a multiple fence configuration which prompts the term fluid fence or as expressed by F-106 fighter pilots - aerodynamic fence. Note that at 21° α, the slot vortices have apparently left the surface and would suggest that slot effectiveness is nearing termination.

The pitching-moment characteristics of the thick wing with slots (fig. 29(b)) are similar to the thin wing in that a severe pitch-up is indicated at $\alpha \approx 19^{\circ}$. It is thought that the rapid spread of separation (n_s plot) causes a separation region near the wing tip that results in an aft loss of lift and, consequently, longitudinal instability. This can be noted in the visualization picture near the wing tip where the accumulation of oil signifies separation.

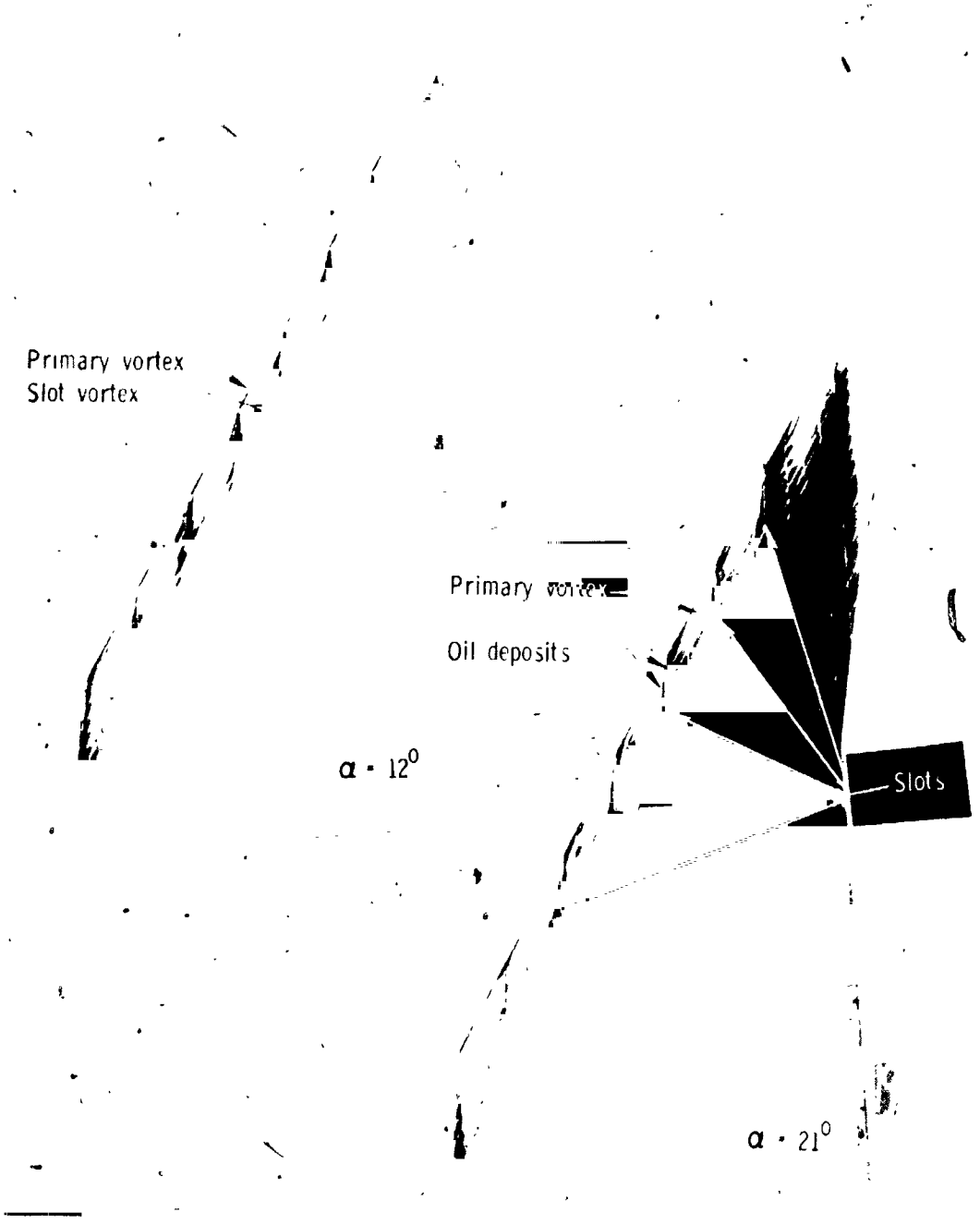

Figure 31.- Oil flow visualization picture of thick wing with slots at 25, 37.5, 50, 62.5, and 75 percent semispan.

6.5 PYLON-TYPE VORTEX GENERATORS (VG)

6.5.1 Sweep Angle

This angle, as measured down from the horizontal plane of the wing, was judged to be an important geometric parameter because it determines the position of the VG ahead of and below the wing LE. The effect of sweep angle on VG performance is presented in figure 32. (Refer to fig. 4 for VG dimensions.)

The upper C_A graph in the figure shows the effect of varying the sweep angle with two VGs (located at η = 0.75 and 0.875) on the thin wing. The data indicate that a reduced sweep angle incurs a small drag penalty in the mid-α range, and an equally small drag reduction at the higher angles. From this comparison, the 30° sweep VG was selected for further study.

The second C_A graph in figure 32 shows a comparison between VGs with sweep angles of 30° (VG4) and 20° (VG6) located at η = 0.625 on the thick wing. These VGs had toe-in angle of 10°. (Toe-in effect will be discussed in the next section.) At the lower angles of attack, both VG sweep angles produce almost identical drag penalties which are minor with respect to the basic wing. The effectiveness of these devices may be judged by the elimination of axial force reversal and the subsequent thrust gain beyond about 12° α - right up to the highest α tested. From this comparison, the VG6 was eliminated on account of its somewhat lower performance and thus, the 30° sweep angle was deemed to be a near-optimum design.

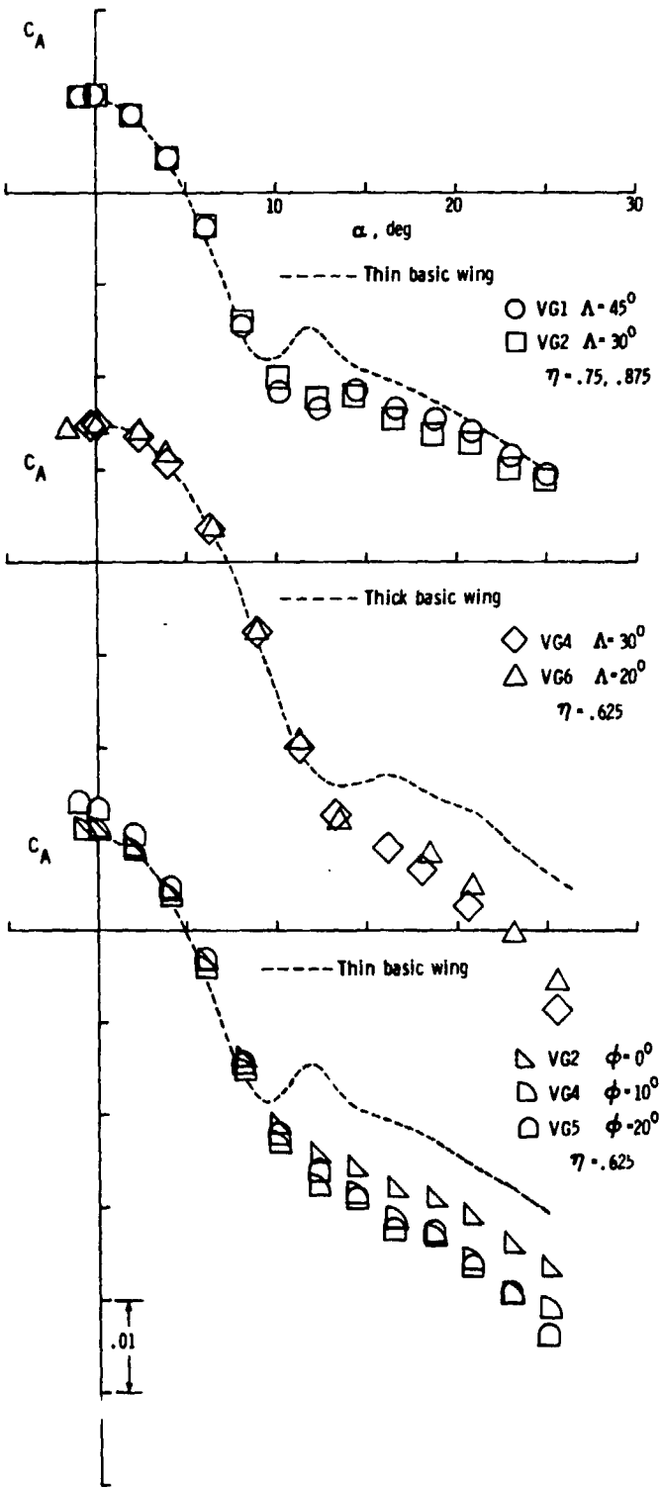

Figure 32.- Effect of VG sweep angle and toe-in angle.

6.5.2 Toe-In

The pylon-type VG acts as a lifting surface in the sidewash induced ahead of the LE of the wing. Thus, by aligning the VG with the sidewash at low angles of attack, the vortex initiation may be delayed so that the maximum effectiveness of the device is retained in the high α range. The results of varying toe-in angles are presented in the last C_A graph in figure 32.

This figure shows toe-in angles of $\phi = 0^o$ (VG2), 10^o (VG4), and 20^o (VG5) with each device located at $\eta = 0.625$ on the thin wing. The first notable effect is near $\alpha = 0^o$ where 20^o toe-in indicates a larger drag penalty than the other two angles. Beyond $\alpha_D \simeq 8^o$, better performance is provided by toe-in angles of 10^o and 20^o, but due to the excessive α zero drag, the 20^o toe-in angle was not tested further.

An uncertainty introduced into this evaluation was the sideways deflection of the VGs under aerodynamic load. This was observed via a TV monitor where the 0^o toe-in VG was actually operating at some toe-out angle at high angles of attack. Thus, although the qualitative effects of VG toe-in have been noted, the present data are insufficient to identify an optimum toe-in angle. Also, the effect of wing sweep angle on VG performance requires additional research.

6.5.3 Position

The spanwise position of a LE device has already been noted to be an important parameter governing drag-reduction effectiveness. Figure 33 presents the data on three series of tests that were conducted to establish the best spanwise position for a single VG.

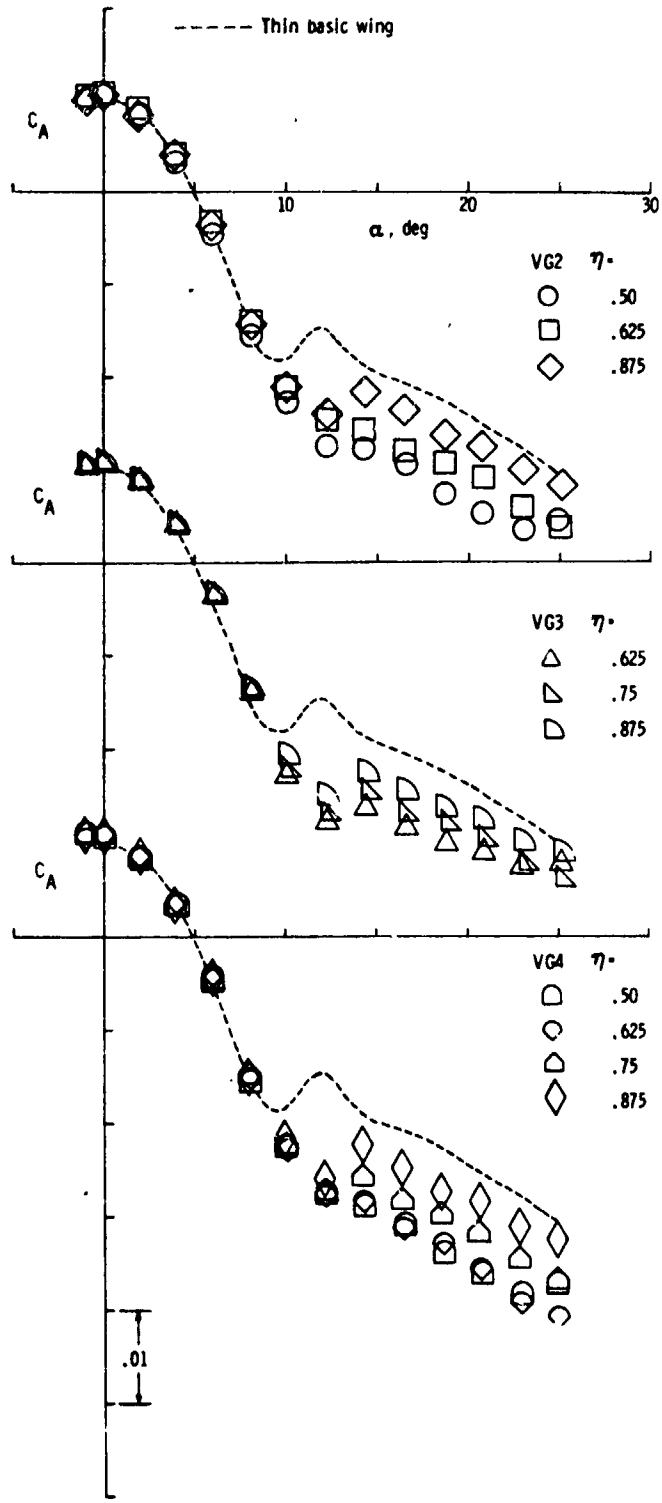

Figure 33.- Effect of VG spanwise position.

The top C_A graph in the figur contains the data for the VG2 (0^o toe-in) which was tested at three difference semispan positions (η = 0.50, 0.625, and 0.875) on the thin wing. The low α characteristics are similar to previous tests (minor drag penalty) with increasing improvement of high α drag as the VG is moved to inboard stations. The severe thrust reversal observed with the VG at η = 0.875 suggests that there exists an outer spanwise limit for this device.

The center C_A graph in figure 33 presents the data on the VG3 successively positioned at η = 0.625, 0.75, and 0.875 on the thin wing. Note that the VG3 was actually a "hybrid" device incorporating a fence as well as a VG (see fig. 4). Again, the most inboard of these positions shows the best performance; however, a substantial thrust loss occurs at about 12^o α in all cases which is an undesirable aspect of this VG design. This device will be discussed in more depth in Section 6.5.4.

The last C_A graph in figure 33 shows the results with the VG4 (having a 10^o toe-in) positioned successively at η = 0.50, 0.625, 0.75, and 0.875 on the thin wing. The notable features derived from this figure are that the two outer most spanwise positions (of the VG) experience a thrust reversal at $\alpha \approx 12^o$ and that the two inner positions indicate better (and almost identical) performance.

To summarize the VG position effect, the best drag-reduction capability occurs with the device near the η = 0.50 position. Lacking test data with the VG inboard of η = 0.50 on the thin wing, the following thick wing results are quoted to support this conclusion: at α = 16^o with a single VG4 positioned at η = 0.25, 0.375, and 0.625,

drag reduction (PD) of 8, 11, and 15 percent respectively, were realized.

6.5.4 Lower Edge

It was initially presumed that the drag-reduction mechanism of the VG was based primarily on the induced effect of a streamwise vortex emanating from the lower edge and that the vortex strength would depend on its sweep angle. This led to the development of a VG-shape designated VG3 (see fig. 4). In order to provide sufficient rigidity above the lateral plane, the shape was extended forward of and above the LE. This resulted in what may be regarded as a hybrid device combining the fence and VG effects.

The upper C_A graph in figure 34 shows a comparison between the VG2 and VG3 positioned at $\eta = 0.625$ on the thin wing. The only appreciable differences are at approximately 12° α, where the VG3 has slightly better performance, and beyond 20° α, where the VG3 appears to have lost effectiveness. These minor deviations would seem to indicate that the inclination of the lower edge was not an important design parameter. This subject will be discussed in depth in Section 6.5.7, where it will be suggested that the drag-reduction potential of the VG is based primarily on a vortex emanating from the forward facing edge.

6.5.5 Multiple

It has been shown that high α drag reduction can be strongly dependent on the multiplicity of a given type of device. This effect was investigated with the VG4 in a series of tests on the thin wing.

The center C_A graph in figure 34 presents the results of three arrangements of the VG4 positioned at $\eta = 0.625$, 0.50, and 0.625, and

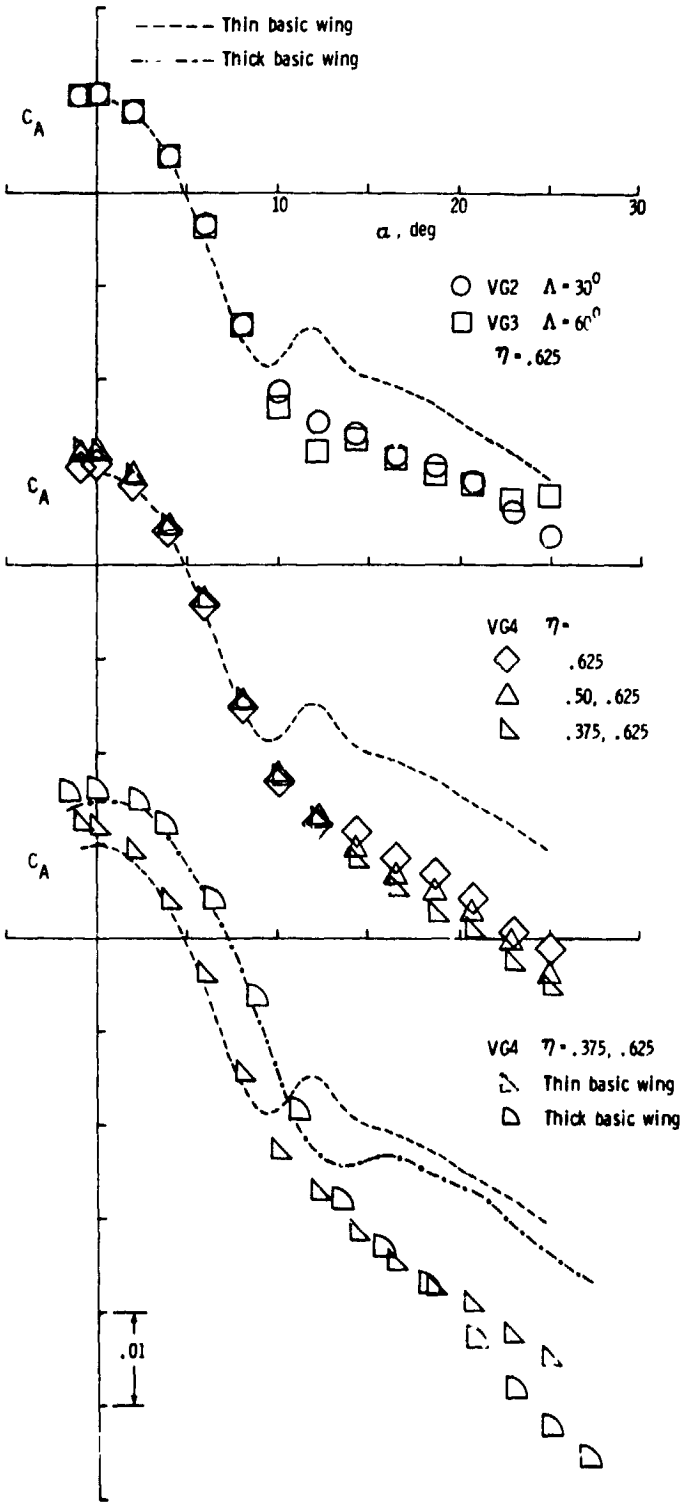

Figure 34.- Effect of - VG lower edge - multiple VG - and leading edge radius - on VG performance.

0.375 and 0.625. At the lower angles of attack, two VGs sustain a slightly higher drag penalty than the single VG, but in the α range of 4^{o} to 12^{o}, little difference can be noted. Beyond $\alpha = 12^{o}$, the addition of a second VG can be seen to produce a relatively constant thrust increment over the single VG, which is dependent on the gap between the twin devices. These data suggest a more detailed investigation of multiples of VGs is warranted, with the devices scaled down to counter the lower α drag penalty.

6.5.6 Leading-Edge (LE) Radius

The last C_A graph in figure 34 shows a comparison between the thin and thick wings with two VG4s at the $\eta = 0.375$ and 0.625 positions. The dashed and chain-dot curves represent the data for the thin and thick basic wings, respectively. The similarity of these data with that contained in figure 24 is apparent with the exception that the VGs on the thick wing generate a somewhat higher thust level as indicated by the crossover in the data near 18^{o} α. This would suggest that LE radius had an influence at the higher angles of attack, most likely due to the vortices being shed from the VG.

6.5.7 Best Performance and Flow Mechanisms

Balance derived performance data for two configurations of the VG4 are presented in figure 35. A single ($\eta = 0.625$) and multiple ($\eta =$ 0.375 and 0.625) arrangement was selected because of differing characteristics in the low-high α range. The figure contains C_A, PD, and C_m data with the dashed line representing the thin basic wing. A summary of the configurations tested is contained in Table 4.

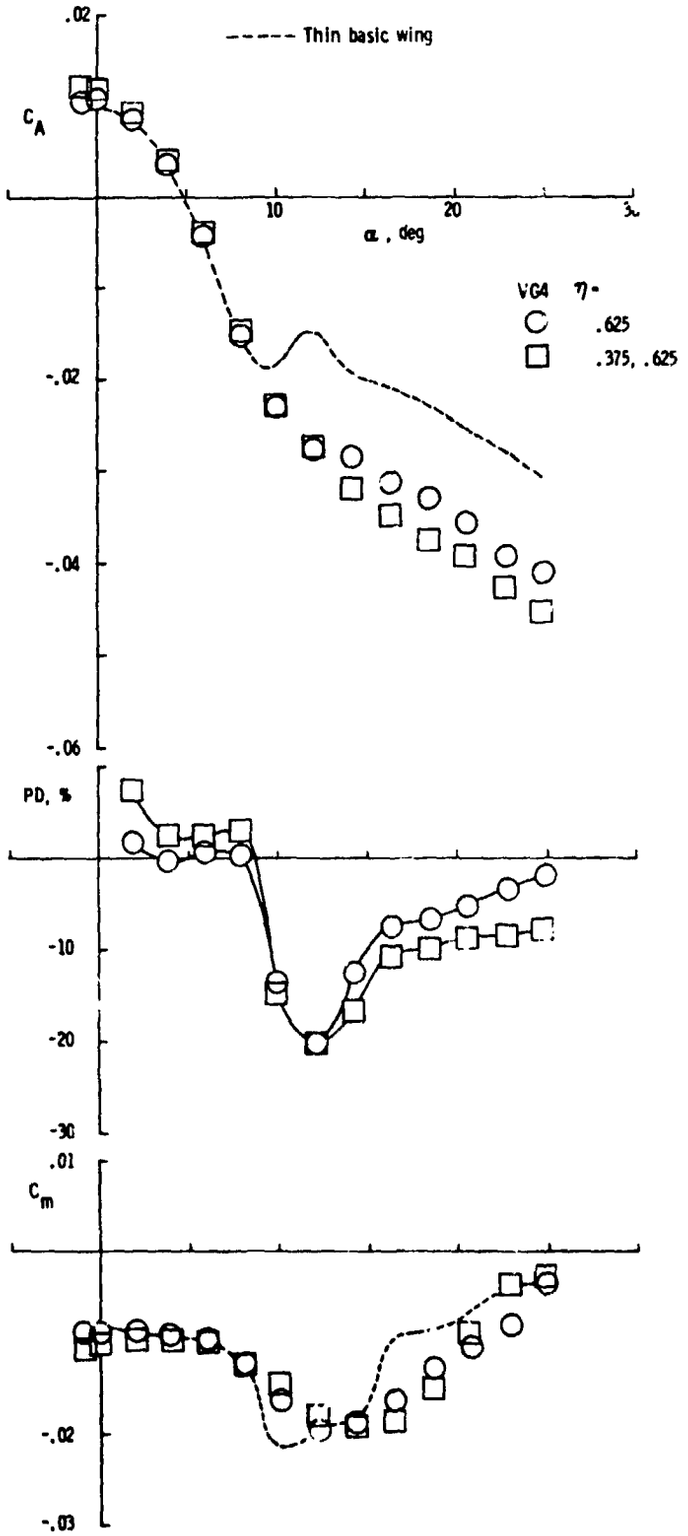

Figure 35.- Best VG performance.

Table 4

Summary of Vortex Generators Tested on Thin Wing

	37.5	50.0	[illegible]	75.0	87.5	C_A @ 12°	PD @ 12°	Run #
BV						.0195	----	64
VG					●	.0 3	-1[illegible].8	1[illegible]
1				●	●	.0218	-11.7	[illegible]
		●				.0278	-18.7	3[illegible]
V3			●			.0[illegible]	-17.0	44
2					●	.0 17	-13.9	1[illegible]
				●	●	.02[illegible]4	-13.[illegible]	2[illegible]
V2			●			.0[illegible]	-20.4	30
3				●		.02[illegible]9	-1[illegible].2	36
					●	.0230	-20.1	1[illegible]
		●				.0293	-19.6	35
			●			.0[illegible]3	-19.[illegible]	31
				●		.0[illegible]0	-17.3	[illegible]7
V3					●	.0225	-17.[illegible]	19
2	●		●			.03[illegible]9	19.8	46
		●	●			.0314	19.1	47
V3b			●			.0[illegible]0	-1[illegible].1	40

At the lower angles of attack, the C_A and PD graphs show that two VGs have more drag and that at about $\alpha = 4^{\circ}$, the single VG in the PD graph indicates slight advantage over the basic wing. Once LE separation begins, the drag reduction capabilities (PD) of both configurations rapidly converge to $\alpha = 12^{\circ}$ - coincidentally to the same value. Beyond 12° angle of attack, the inboard VG appears to become effective as indicated by the divergence of the data. This would suggest that for a design angle of attack below 12°, a single VG would suffice; whereas, for a higher α, a pair of VGs will be needed if the increased low α drag could be tolerated.

The last graph in figure 35 contains the pitching-moment data where it can be seen that a single device becomes longitudinally unstable when achieving maximum drag reduction. Note that the use of two VGs delays pitch-up to approximately 14° α.

The flow mechanisms associated with the pylon-type VG will first be discussed with respect to oil flow visualization on the thin wing at angles of attack of 9° and 16°. The lower α is shown in figure 36(a) where the VG4 is at $\eta = 0.625$. In the top view, two primary vortex systems can be noted on both sides of the VG, which is a situation similar to the fence case. The oil deposit (line of separation) on the wing LE immediately upstream of the VG would indicate that the VG was somehow causing a localized region of stalled flow. In the side view, two vortex formations can be noted on the VG - one along the lower edge and one along the forward facing edge. Note also in the top view at 9° α, the high shear area along the LE just outboard of the VG and the following vortex system positioned further outboard. It is suggested that the flow mechanisms originate as the result of the vortex shedding off the forward facing edge of the VG which then becomes fixed on the upper surface of the wing with a sense of rotation opposite to that of the primary vortex. This situation is depicted in figure 37 where the lower edge vortex is shown to pass beneath the wing.

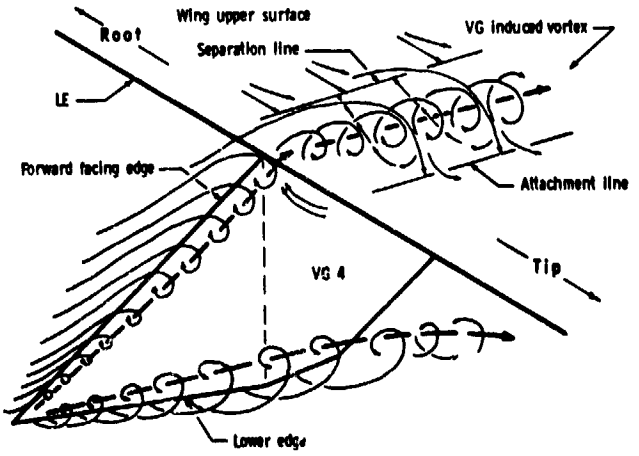

Figure 37.- Illustration of suggested VG flow mechanism.

C-2

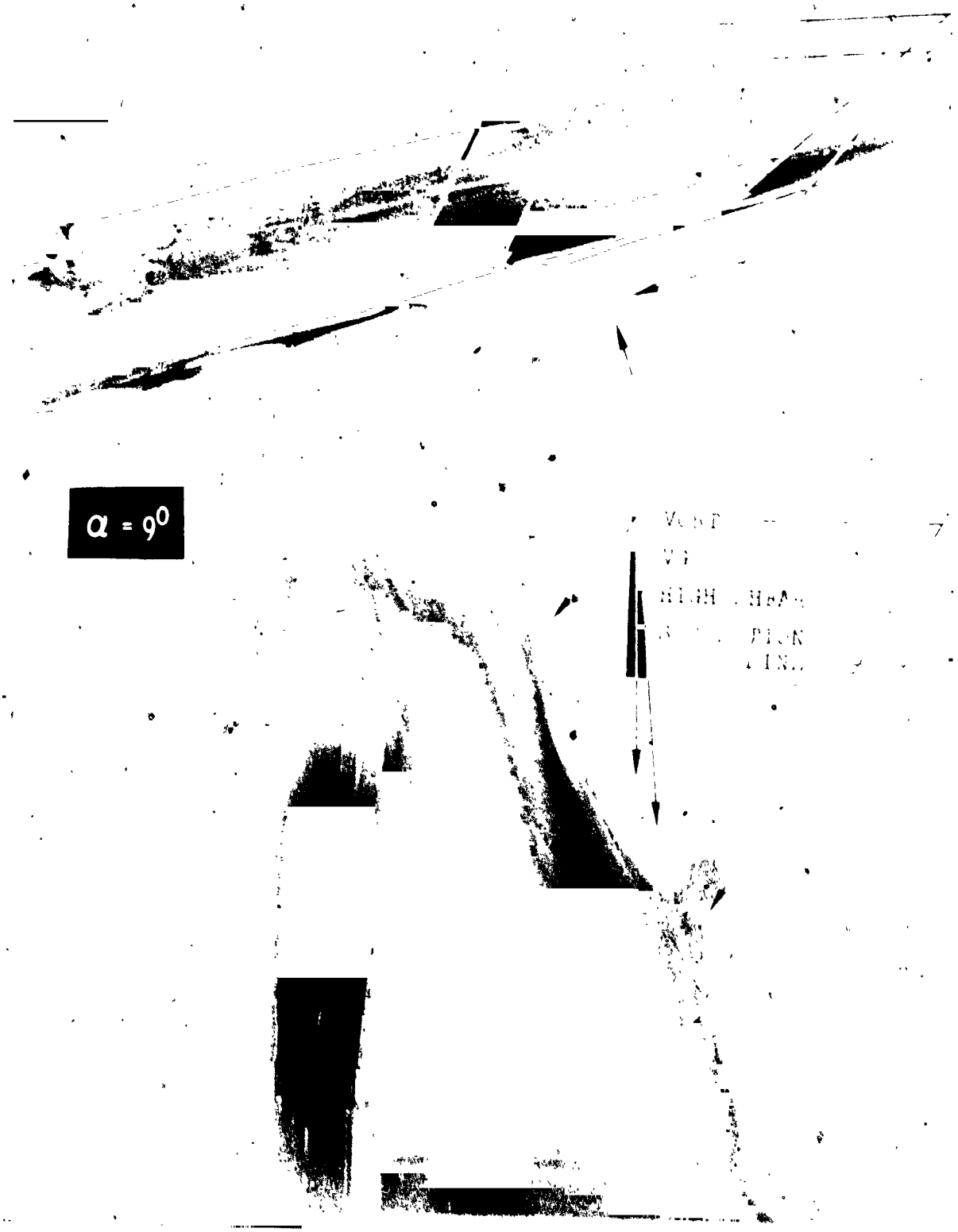

Figure 36(a).- Oil flow visualization pictures of thin wing with VG4 at the 62.5 percent semispan position ($\alpha = 9^{\circ}$ and 16°).

Figure 36(b).- Concluded.

At $\alpha = 16^{o}$, the visualization picture (fig. 36(b)) shows that both LE vortex systems have moved further toward the wing apex; however, the advancement of the downstream vortex is still being delayed by the higher shear area that now extends inboard of the VG. It is believed that the VG induced vortex persists under the influence of the two primary vortex systems and actually acts as a barrier by maintaining localized attached flow. Like the other devices already discussed, the VG is effective in the compartmentation of the wing LE which allows the primary vortex downstream of the VG to generate high levels of aerodynamic thrust.

Realizing that the discussion above was based on the thin wing visualizations, flow mechanisms will now be covered with respect to the thick wing. A comparison of balance and pressure data in figure 38 will provide the basis for this analysis. Also note that the VG was reinforced to preclude bending under aerodynamic loading.

The diagram at the top of figure 38(a) provides the location of VG4 and the relative position of the two pressure stations selected for discussion. Below $\alpha \approx 9^{o}$, the VG has little effect on the LE flow as can be noted in the $C_{T,LCL\ PRESS}$ versus η data at $\alpha = 9^{o}$. This is probably due to the close alignment of the VG with the oncoming flow and that any vortex shed from the device would pass beneath the wing, at this low α. The evidence of this can be noted in the C_p distributions at $\eta = 0.70$ where a distinct low pressure moves towards the LE on the lower surface between $\alpha = 13^{o}$ and 21^{o}. This C_p distribution also shows that the thrust at the LE continues to increase with α as opposed to the basic wing. This would suggest that the vortex emanating

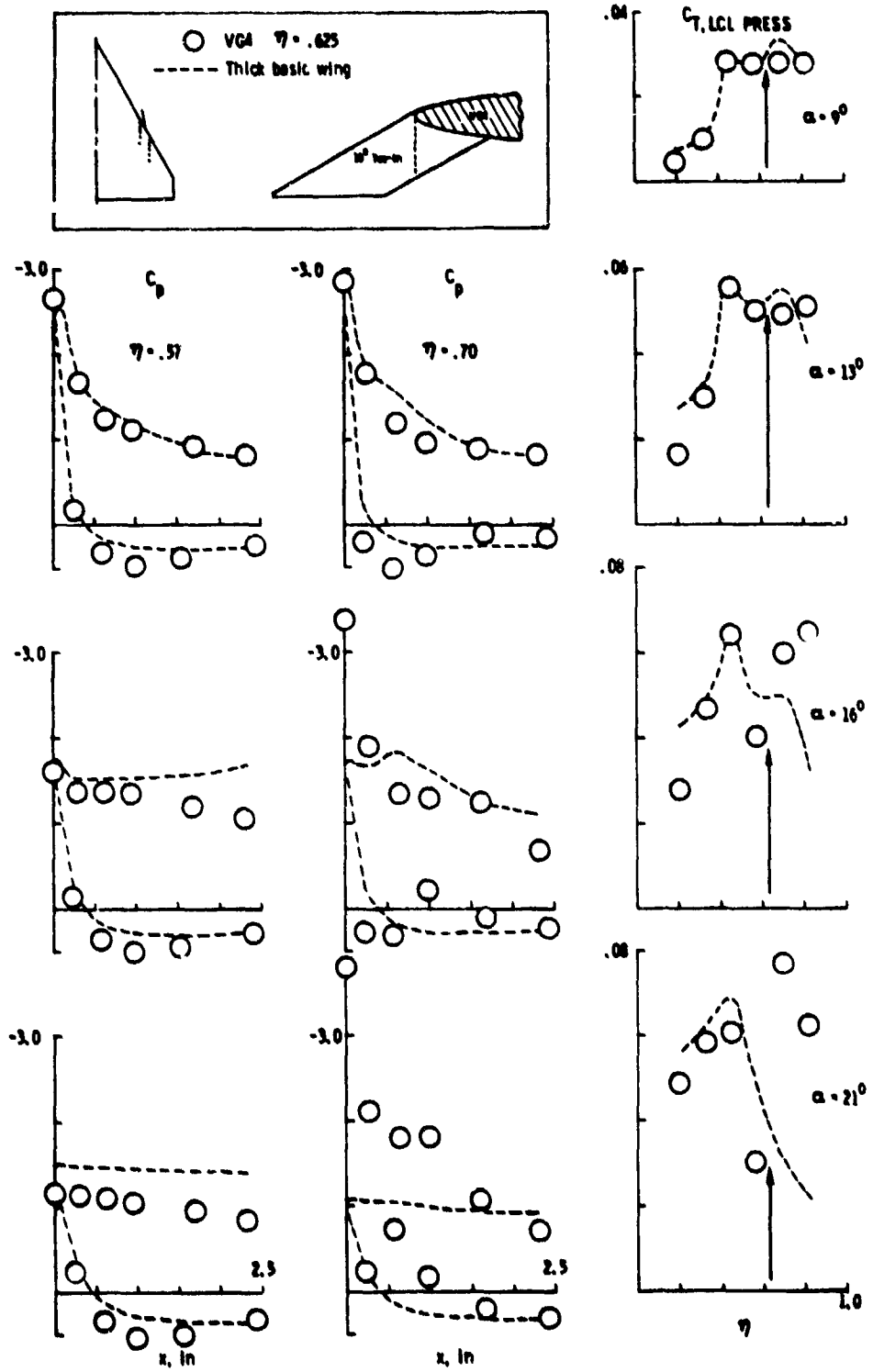

Figure 38(a).- Comparison of balance and pressure data obtained from the thick wing configured with VGs.

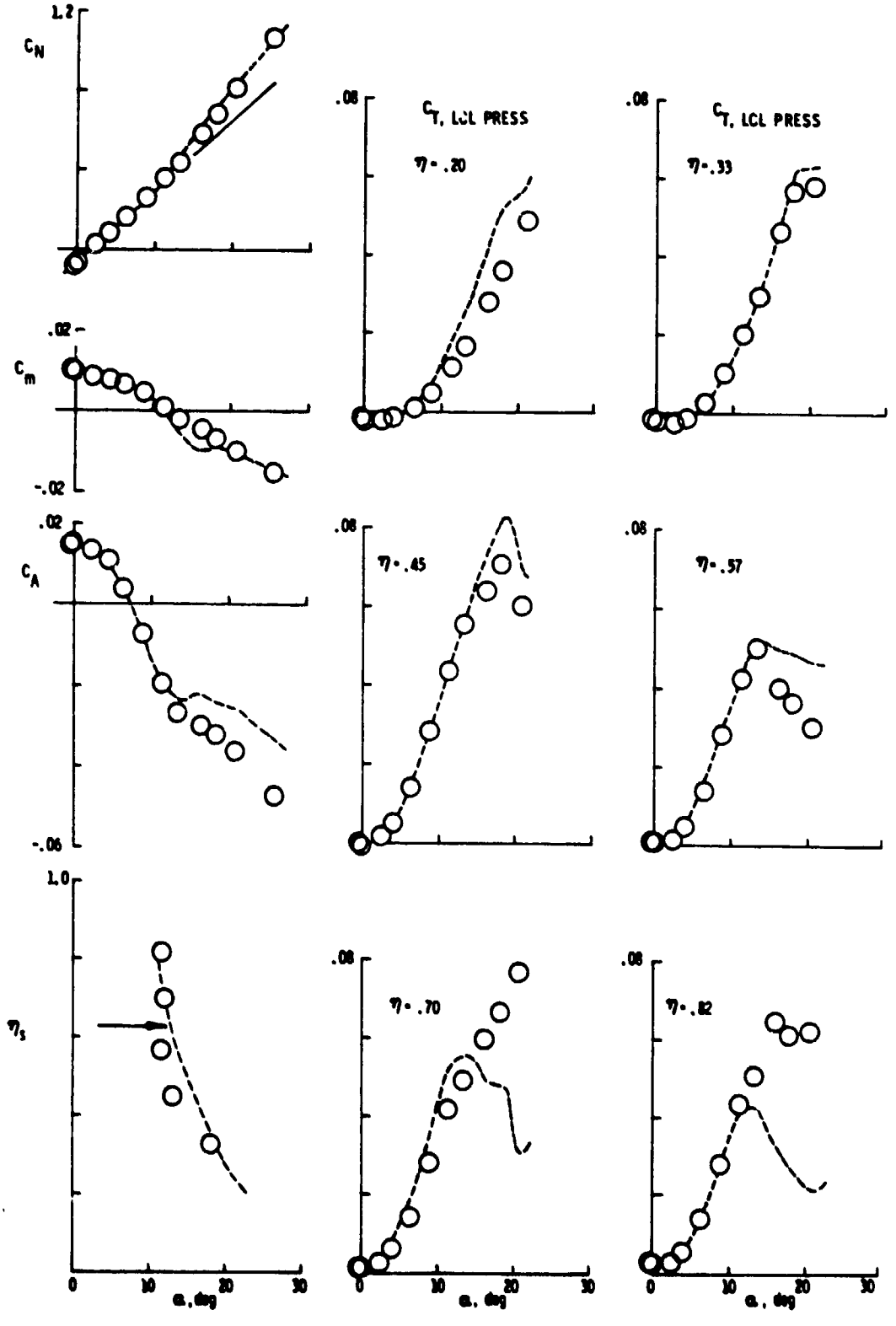

Figure 38(b).- Concluded.

from the lower edge of the VG eventually reaches the wing LE beyond 21° α and would subsequently pass completely over the upper surface. This point cannot be confirmed because of insufficient data at the higher angles of attack.

At the inboard station (η = 0.57), the C_p distributions indicate trends similar to the basic wing but with somewhat higher pressure levels of stagnated flow beyond α = 16°. This would tend to confirm the earlier observation from the thin wing oil visualization pictures in that the VG produced an increased upwash velocity inboard and, thus, a higher pressure level, e.g., at α = 21°. The effectiveness of the VG outboard can be noted in the $C_{T,LCL\ PRESS}$ distributions at α = 16° and 21° (fig. 38(a)).

The $C_{T,LCL\ PRESS}$ versus α distribution just outboard of the VG (at η = 0.70) indicates a slight loss of thrust in the α range of 5° to 14° (fig. 38(b)). It is thought that the vortex separating from the forward facing edge of the VG induces a downwash in this area which effectively reduces the angle of attack. C_p distributions also show this at lower angles of attack (not presented) as well as at α = 13°.

The balance data in figure 38(b) show trends typical of this study, e.g., a slight reduction in vortex lift (C_N) and a more gradual pitch-down without subsequent pitch-up (C_m). The η_s data indicate that the VG induced the onset of LE separation to occur simultaneously from η = 0.57 to 0.82 (at about 11° α), which caused a serious thrust decay near 15° α over the mid-section of the LE, viz., η = 0.40 to 0.60, which has been shown to have the greatest thrust potential. A fix for this problem is presented in Section 6.7.2.

6.6 SHARP LEADING-EDGE EXTENSIONS (SLEE)

6.6.1 Length and Position

These effects were considered to be the two most practical ways of alleviating the excessive drag that was expected to be incurred by the SLEE in the low α range. It was assumed that (1) shortening the SLEE would reduce profile drag, and (2) lowering the SLEE might create additional LE thrust, viz., exposing more of the wing forward facing area to the action of the SLEE induced vortex. SLEE length reductions along the wing LE were accomplished by progressively removing inboard portions of the SLEE. SLEE performance and characteristics are discussed next.

The upper C_A graph in figure 39 contains the data on four length variations of the mid-SLEE (see fig. 5 for SLEE dimensions) in which three trends can be noted: (1) the magnitude of $C_{A,0}$ is lowered somewhat with length reductions; (2) in the α range of approximately 2° to 9°, severe drag penalties arise with increased lengths, and (3) the shortest length provided the best drag reduction for all angles of attack. This latter trend was surprising because the longest SLEE would be expected to yield the most drag reduction. In view of this result, the evaluation was continued with the SLEE positioned in the plane of the wing's lower surface.

The center C_A graph in figure 39 presents two length variations of the low SLEE. This position of the SLEE eliminated the poor lower α drag performance of the mid-position and also showed significant gains beyond $\alpha_D = 8^\circ$, but at the expense of the 0° α drag. The length effect can be noted beyond approximately $\alpha = 16^\circ$ where the full-span

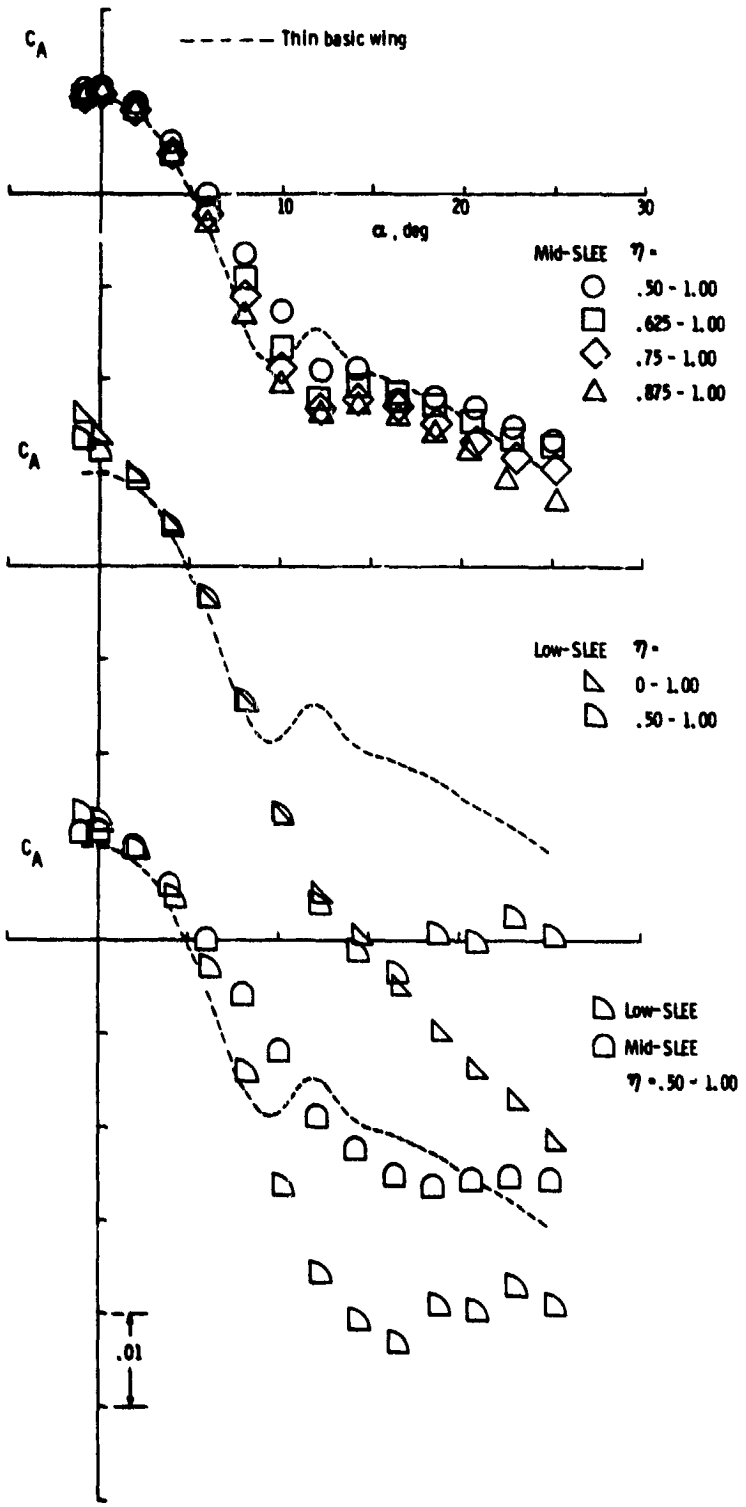

Figure 39.- Effect of SLEE length and position.

low-SLEE continues to diverge from the basic wing data while the half-span device suffers a severe thrust loss. This is consistent with the fact that the primary vortex system nears the apex of the thin wing at this α and, therefore, the continuance of thrust can be attributed to the inboard 50 percent of the low SLEE. Since the original contention (that length effect should be an impo~tant performance parameter) has been shown, it follows that the SLEE position is also significant.

To illustrate the effect of position, the last C_A graph in figure 39 presents a comparison of the half-span SLEE (η = 0.50 to 1.00) in the mid and low positions. Because the only differences in the two configurations was the amount of foward facing wing LE area and vertical position, it can be assumed from the data that the low SLEE was able to maintain the vortex in front of the LE; whereas, the vortex emanating from the mid SLEE is most probably lost to the upper surface. This subject will be discussed in detail in the following subsection.

6.6.2 Best Performance and Flow Mechanisms

As the result of the data just presented, the half- and full-span low SLEE were selected for further analysis to include discussion of flow mechanisms. Aerodynamic characteristics are shown in figure 40 and a summary of the configurations tested, along with drag-reduction performance at selected angles of attack, are contained in Table 5.

Table 5.- Summary of Sharp Leading-Edge Extensions Tested on Thin Wing

	0.0	50.0	62.5	75.0	87.5	100.0	C_A @ 15°	PD @ 12°	Run #
BW							.0195	-----	58
Mid-		●				●	.0199	-4.7	1
			●			●	.0210	-7.1	5
				●		●	.0221	-8.8	6
					●	●	.0231	-10.2	8
Low-	●					●	.0412	-23.1	59
		●				●	.0430	-26.6	41

The ability of the SLEE to maintain the flow at the LE is illustrated in the C_A graph at the top of figure 40 where the gradual departure characteristics yield a significant drag reduction in the mid α range. The fact that the half-span low SLEE (circle symbol) loses effectiveness at $\alpha \approx 17^{\circ}$ (while the full-span low SLEE continues to function) can be attributed to the vortex moving onto the wing upper surface in the outboard region. These performance trends are confirmed by the drag parameter (PD) (center graph) where the half-span SLEE develops a 27 percent reduction in drag at 12° angle of attack and the full-span SLEE shows a sudden decrease in drag starting at about 17° α as indicated by the sharp reduction in slope.

The pitching-moment data at the bottom of figure 40 indicate that both devices are longitudinally unstable except in the α range of approximately 8° to 12°, viz., between the onset of LE separation and the α for maximum drag reduction. While it is possible to improve the low α pitching characteristics (by moving the center of gravity further forward of the aerodynamic center), the severe pitch-up at 12° angle of attack would still be present - in fact, this shift in CG would actually reduce the controllability and thereby add to the maneuverability design problem.

The drag-reduction capability of the SLEE in the low position is quite remarkable in that a gain of 27 percent was achieved by such a small device (approximately 2 percent of the wing area for the half-span SLEE). It is recognized that the high $C_{A,0}$ values and longitudinal instability detract from the SLEE effectiveness; however, a fix for the latter problem will be covered in the section on combination of devices.

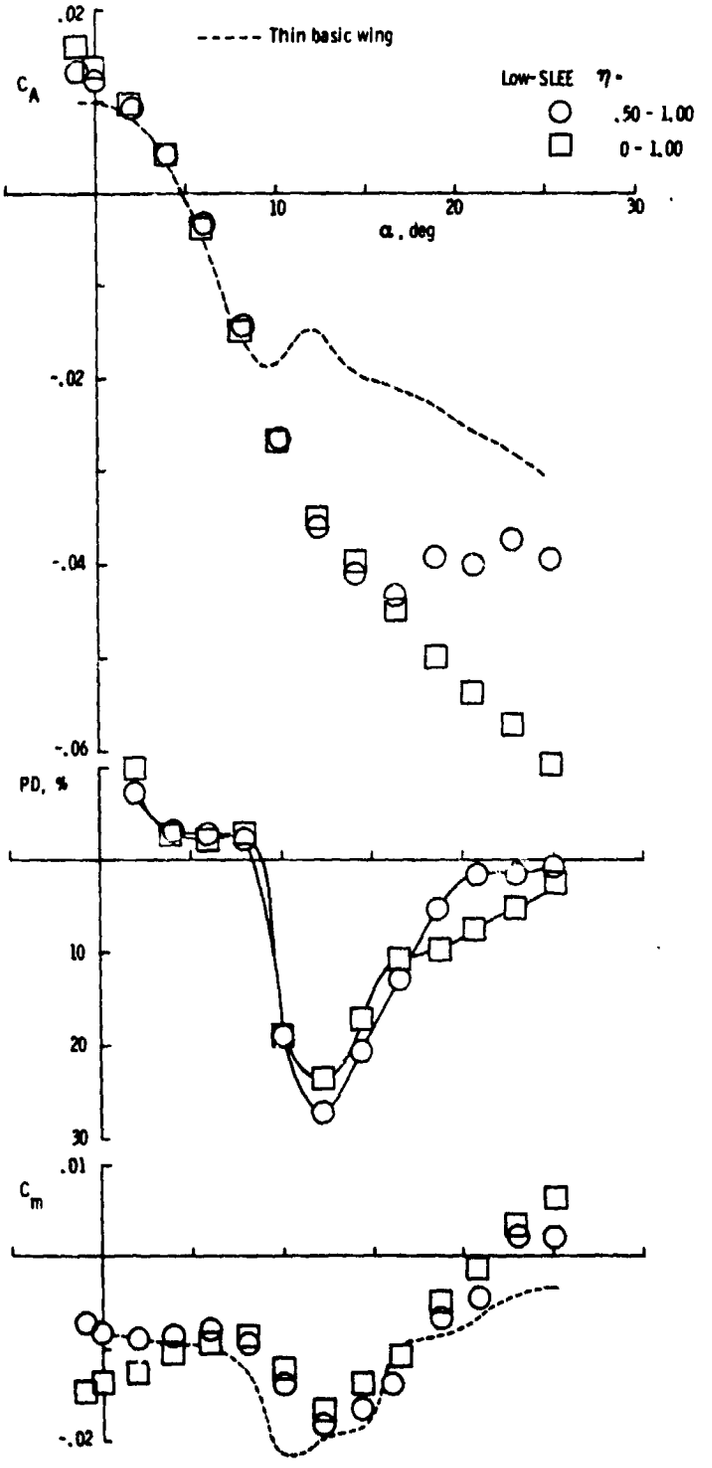

Figure 40.- Best SLEE performance.

This section will now be concluded with a discussion of the flow mechanisms associated with the SLEE.

The key feature common to the fence, slot, and pylon-type VG is the ability to maintain attached flow at the LE near the device and thereby allowing increased LE thrust levels to develop. On the other hand, the SLEE (sometimes referred to as a vortex plate) operates on the principle of forced separation at its LE which results in the formation of a tightly coiled vortex just in front of the wing's blunt LE. This situation is depicted in figure 41.

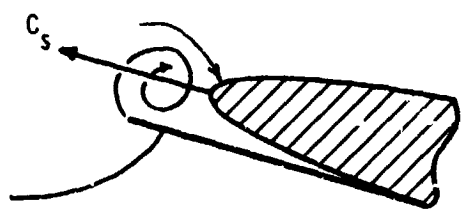

Figure 41.- Illustration of suggested SLEE flow mechanism.

With the vortex locked in this position, the low pressure will act on the forward facing area of the wing to create an additional suction force and, thus, higher levels of drag reduction will be achieved. This can be noted in figure 42(a) by comparing the C_p distributions around the thick wing LE for the low SLEE (η = 0.25 to 0.93) and the basic wing. At $\alpha \approx 11^\circ$, the lower surface pressure coefficients (square symbols) show high negative values as opposed to the positive values for the basic wing - this condition is also present at angles of attack of 16° and 21°. This pressure trend is evident in the C_T versus η distribution at the higher angles. This information suggests that below 11°, the vortex strength is only sufficient to offset the additional

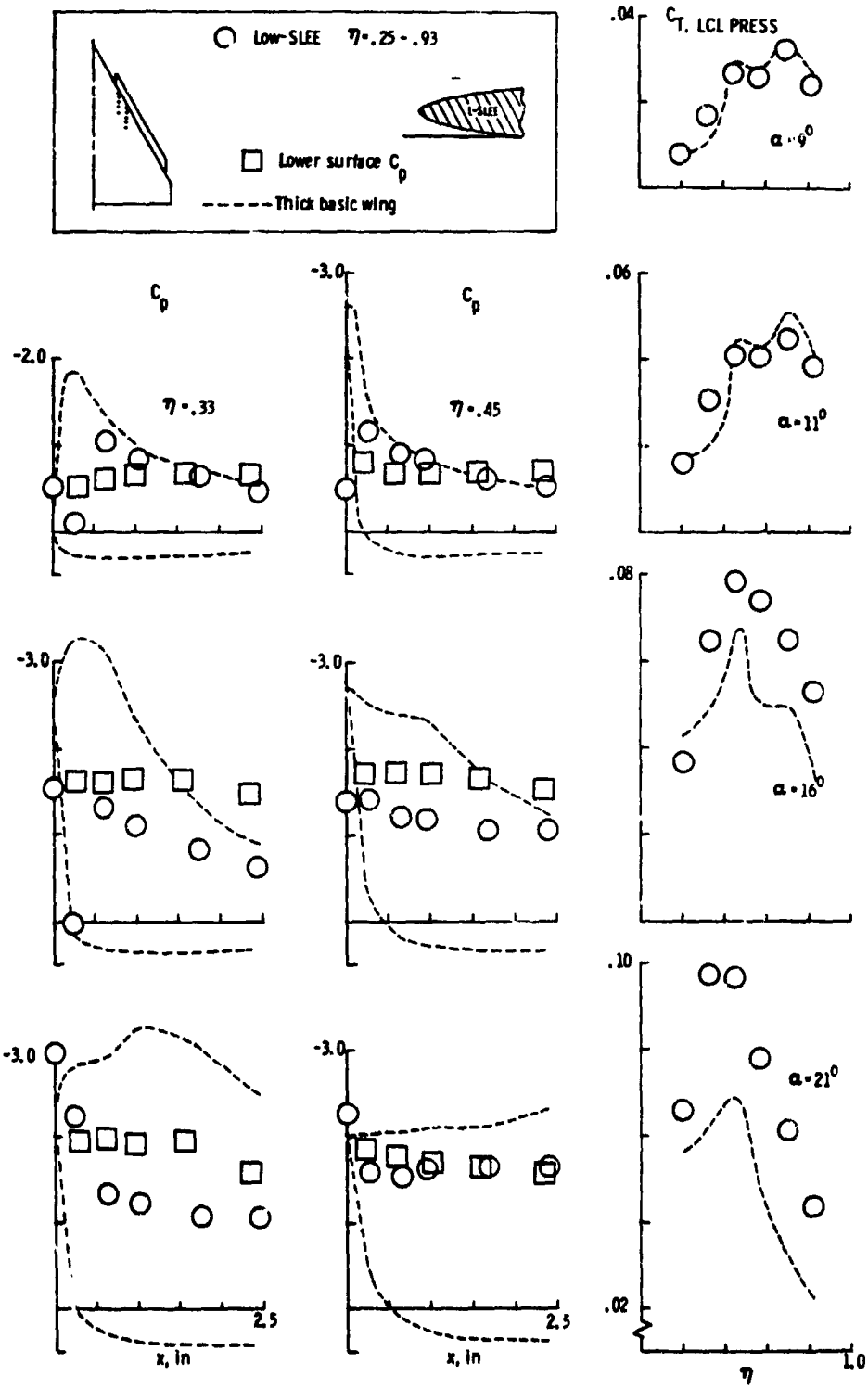

Figure 42(a).- Comparison of balance and pressure data obtained from the thick wing configured with L-SLEE.

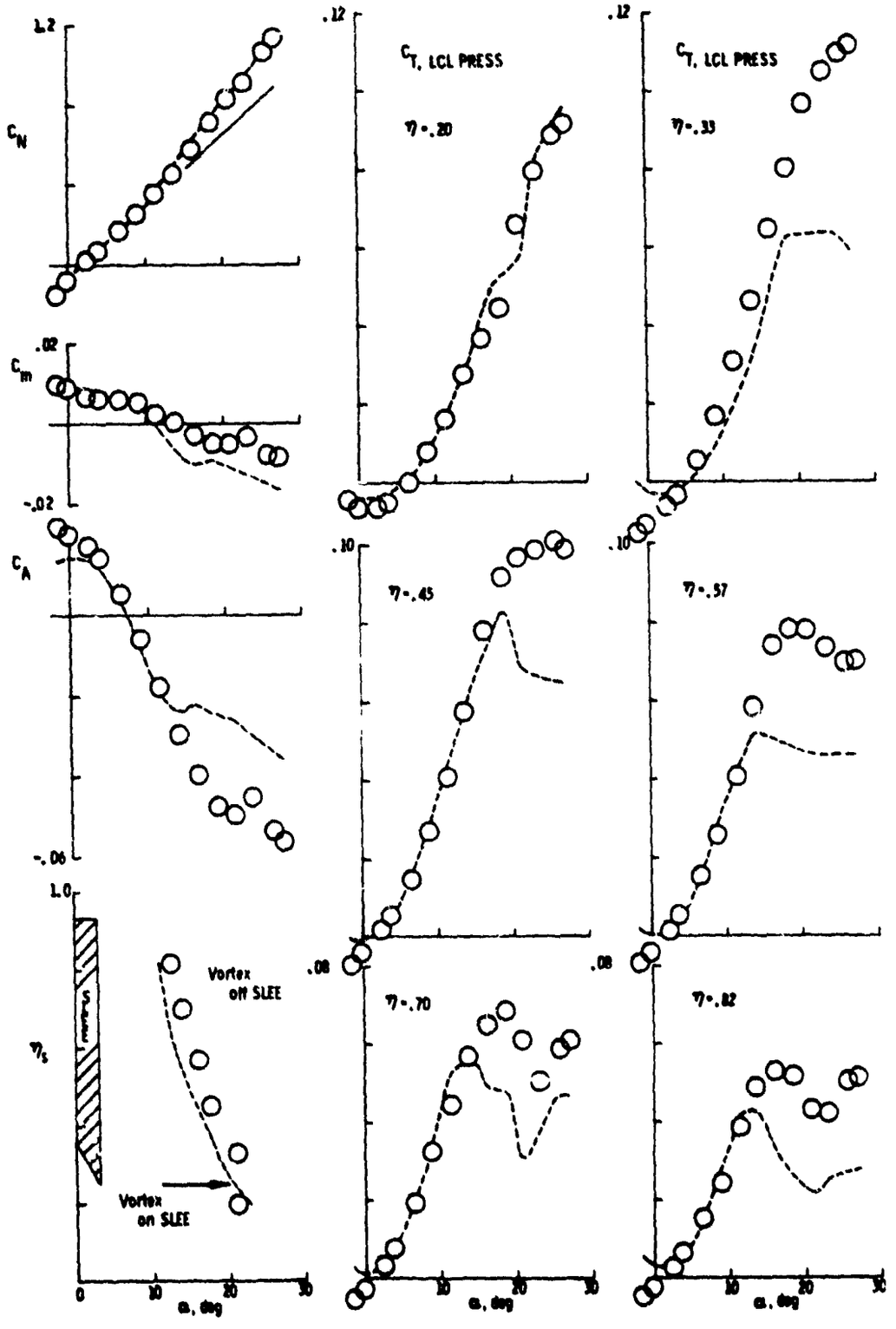

Figure 42(b).- Concluded.

drag of the SLEE; however, beyond 16°, the magnitude increases sharply yielding significant drag reduction. This tendency can also be noted in the C_T versus α distributions in figure 42(b).

The balance derived aerodynamic characteristics set forth in figure 42(b) show that the onset of wing LE separation occurs at $\alpha \approx 9°$ as indicated by the nonlinearity in the normal force (increase in lift) and the departure of the axial force from a parabolic shape (decrease in the rate of thrust development). The pitching-moment data show other favorable aspects of the SLEE, e.g., a more gradual pitch-down near $10°$ α and a subsquent delay in pitch-up. The η_s versus α data would appear to indicate that LE separation has been delayed by about $2°$ α; however, the interpretation of these data is complicated by the presence of the SLEE vortex along the LE. In this case, it is suggested that η_s actually represents a transition boundary which establishes the position of the SLEE vortex as being either on the SLEE (to the left of the curve) or on the wing upper surface (to the right).

It can be concluded that the low SLEE is a unique drag-reduction device well suited for blunt wings of relatively high sweep operating at high angles of attack. The flow mechanism has been established as a trapped vortex acting primarily on the chin of the wing LE. The tendency for the vortex to move streamwise onto the wing upper surface will ultimately limit the SLEE effectiveness - as shown by the thrust loss at the three outboard stations at about $\alpha = 20°$ (C_T vs α in fig. 42(b)). Methods to delay this vortex jump and thus improve SLEE performance will be discussed in the next section.

6.7 COMBINATIONS OF DEVICES

6.7.1 SLEE with Fence

6.7.1.1 Length and position.- It is evident that SLEE drag-reduction performance is based primarily on the ability to maintain the induced vortex along its length. This was noted in the last section where marginal performance was indicated in the mid α range due to the vortex moving onto the wing's upper surface. To combat this situation, the characteristics of the fence were suggested as a possible solution, i.e., to delay separation outboard and thus the compartmentation of that portion of the wing under the influence of the SLEE. Therefore, a study was conducted to evaluate the drag-reduction performance of the SLEE fence combination. The dimensions of these devices are shown in figure 5.

The top C_A graph in figure 43 presents the results of four length variations of the mid SLEE in combination with the F2 fence. It is apparent that the addition of the fence had very little effect as can be noted by a comparison of the fence-off data (at the top of fig. 39). From these data, it was concluded that the mid position of the SLEE was an ineffective drag-reduction device and therefore testing was terminated in favor of the more promising low position.

As shown in the center C_A graph in figure 43, the addition of the F4 fence to the low SLEE configuration demonstrated marked improvement in drag-reduction performance for all lengths in the higher α range. In the lower α range, there is a slight drag penalty irrespective of length except near $\alpha = 0^o$ where the data diverge in a parallel manner. This would appear to indicate that the fence did isolate the

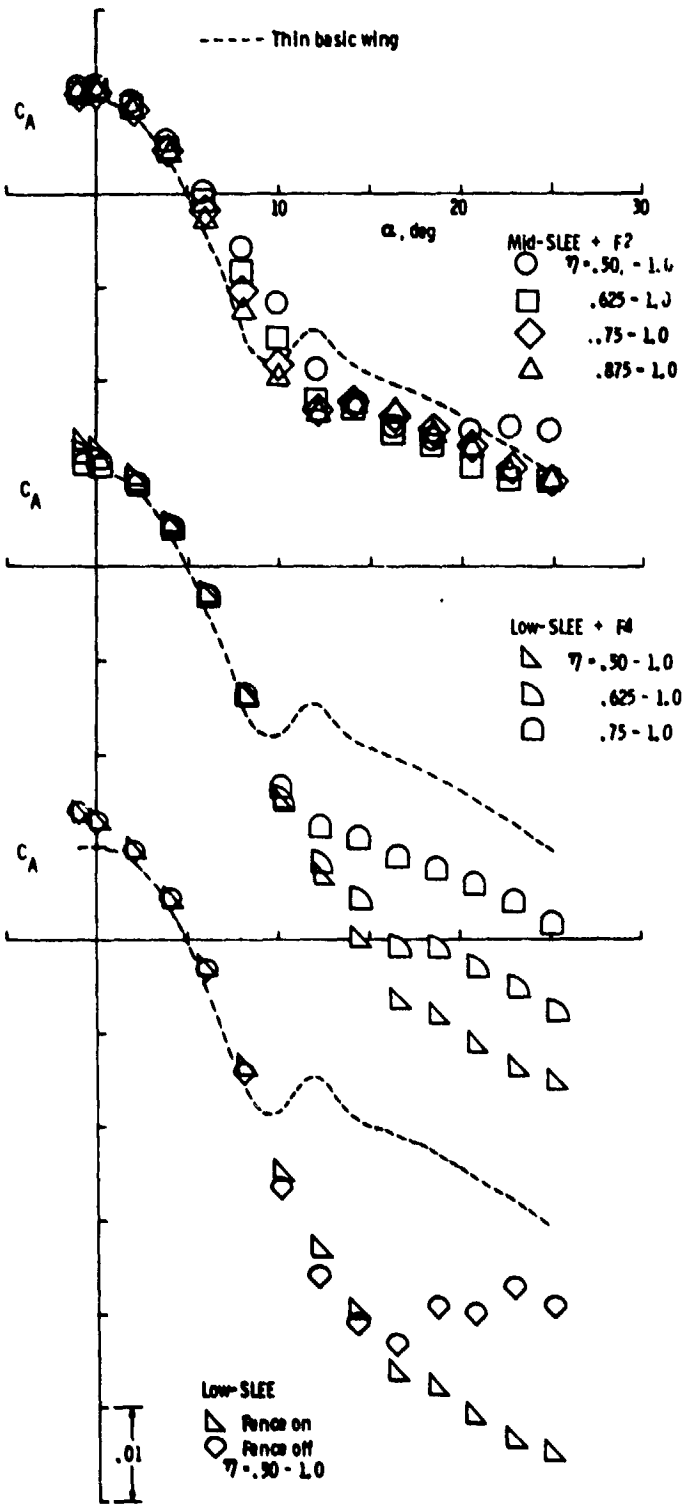

Figure 43.- Effect of SLEE length and position in combination with a fence.

SLEE and, thus, was able to maintain the vortex in front of the wing LE to the highest angles tested. This point is more vividly shown in the last C_A graph where a comparison between fence on and off is made. Another interesting observation is that the full-span SLEF without fence (center graph in fig. 39) has almost identical C_A characteristics as the half-span SLEE with fence.

From these results, it can be concluded that the addition of the fence to the low SLEE configuration enhanced drag-reduction performance. The ability of this combination to "lock" the vortex at the wing LE is self-evident and suggests other arrangements that might be more successful, e.g., a length extending from η = 0.25 to 0.75 with F4 fences at η = 0.25, 0.50, and 0.75, and a full-span SLEE with F4 fence at η = 0.50.

6.7.1.2 Best performance and flow mechanisms.- From a comparison of the tabulated performance data in Table 6, the half-span low SLEE with F4 fence was chosen for further discussions of performance and flow mechanisms.

Table 6.- Summary of Sharp Leading-Edge Extensions With Fences Tested on Thin Wing

	50.0	80.0	[illegible]	[illegible]	87.5	100.0	C_A @ 15°	PD @ 1.5°	Run #
BW							.0195	-----	58
Mid-		F2 ●				●	.0236	-6.7	3
			F2 ●			●	.0241	-9.4	4
				F2 ●		●	.0257	-11.4	7
					F2 ●	●	.0259	-13.1	9
Low-		F4 ●				●	.0241	-13.5	6
			F4 ●			●	.0273	-17.6	43
				F4 ●		●	.0259	-19.5	60

To illustrate the contributions made by the addition of the fence, the performance characteristics presented in figure 44 also contain the data for the fence-off case (square symbol). The C_A data at

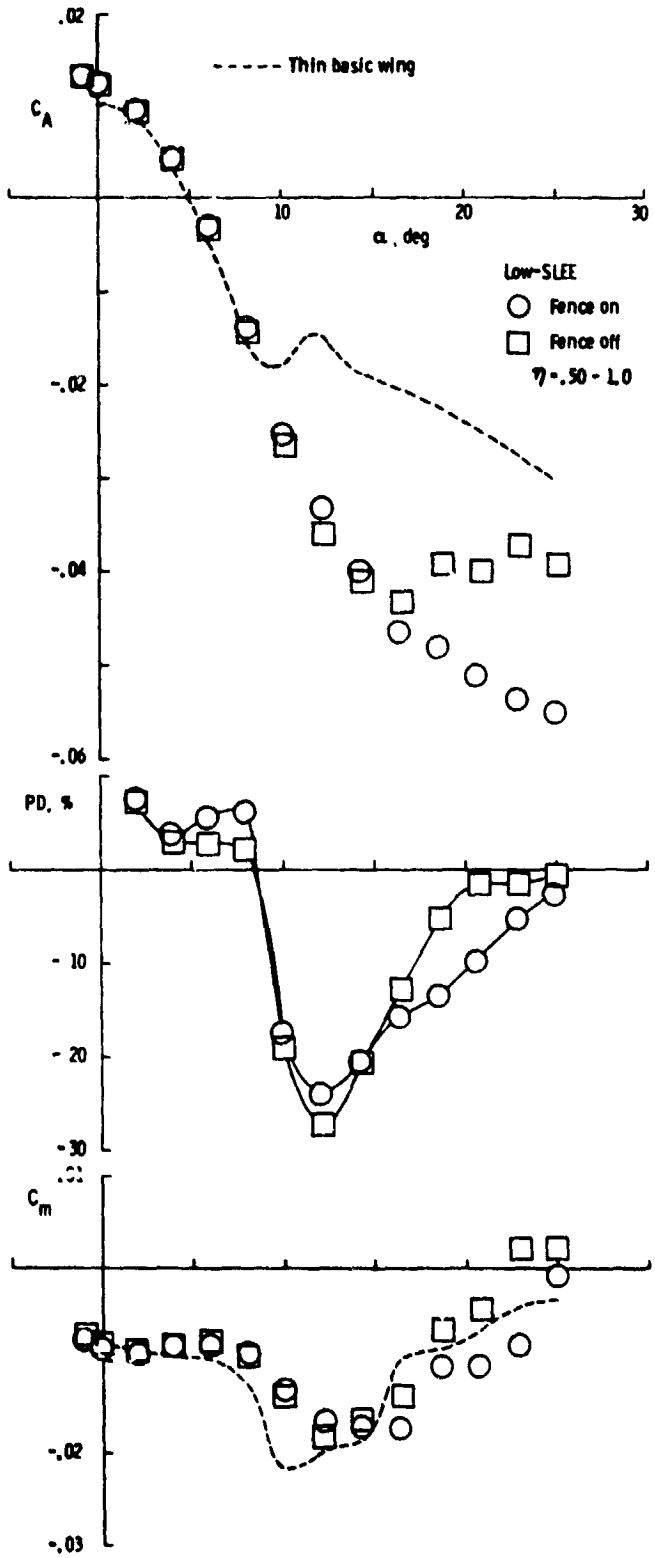

Figure 44.- Best SLEE fence performance.

the top of the figure show almost identical performance to about $\alpha \approx 14^{\circ}$ which is reflected by the PD curves in the center graph. However, beyond 14° α, the fence characteristics take effect to yield additional drag reduction which is similar to the performance achieved when the half-span SLEE (fence off) was extended to a full span, viz., the drag-reduction performance of a half-span low SLEE can be significantly improved by either adding a fence or extending the device to full span. The pitching-moment data in the last graph indicate that the fence has delayed the pitch-up phenomenon by about 4° α, although the strong pitch-down is still present.

The ability of the fence to improve the SLEE drag-reduction performance at the higher angles is noteworthy, especially in the presence of the SLEE induced vortex. This section will, therefore, be concluded with a discussion of the interaction between these two devices and a rationale for the flow mechanism.

To support this analysis, a SLEE fence combination was evaluated on the pressure instrumented thick LE. The pressure derived coefficients (C_p and C_T) and balance data are presented in figure 45 along with a drawing of the test configuration. A comparison of the C_p and C_T distributions for the fence off (fig. 42(a)) and fence on (fig. 45(a)) at angles of attack of 9°, 11°, and 16° show almost identical performance. This would seem logical in that the primary vortex system has not advanced sufficiently upstream for the fence characteristics to have a significant downstream effect. Also note in the η_s versus α plot (fig. 45(b)) that the fence has induced early LE separation inboard due to the "pseudo tip" effect which causes a

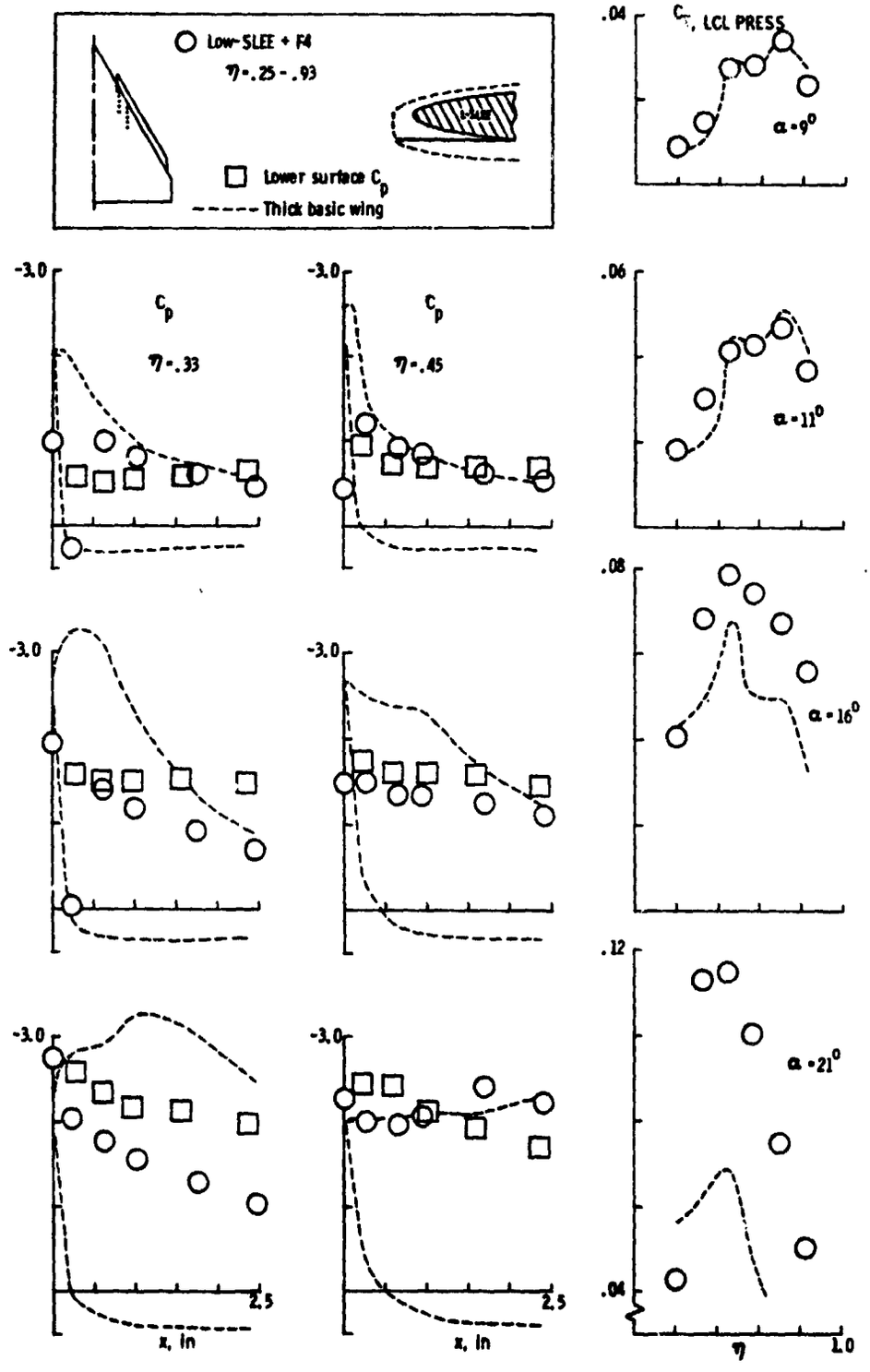

Figure 45(a).- Comparison of balance and pressure data obtained from the thick wing configured with L-SLEE and fence.

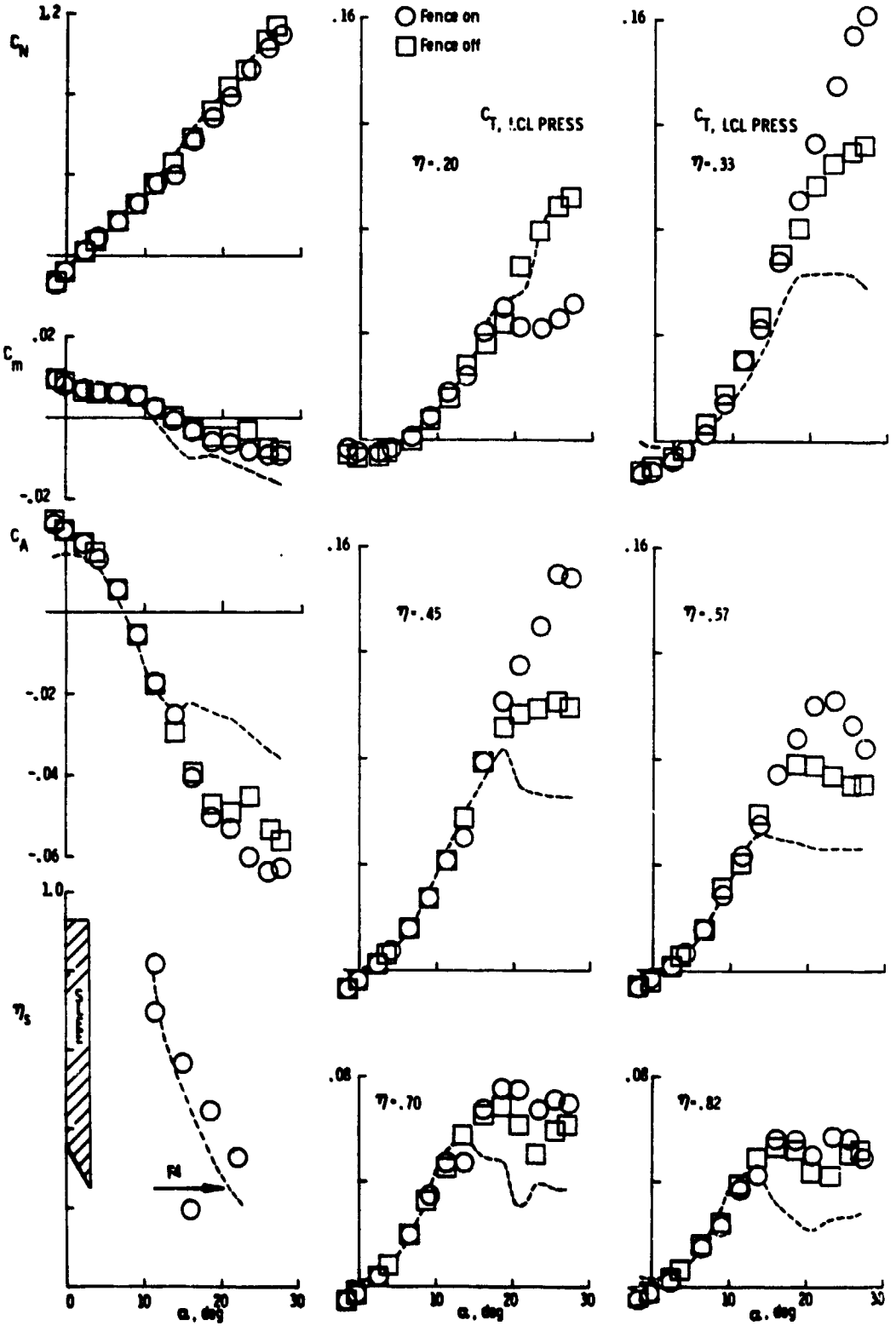

Figure 45(b).- Concluded.

subsequent loss in thrust at about 18° α. (See C_T data at η = 0.20 in the same fig.)

As the advancing vortex system approaches the fence, the "pseudo apex" effect takes place causing a delay in LE separation outboard along the blunt LE and, as a consequence, thrust levels continue to grow. These trends can be seen in the C_T distributions at η = 0.33, 0.45, and 0.57 in figure 45(b) at angles of attack greater than 16°. Also note that the fence has little effect at the two farthest downstream stations. This evidence supports the contention that the influence of the fence has been to lock the vortex on the SLEE which is also illustrated by the high negative C_p coefficients (fig. 45(a)) above and below the wing LE at 21° α.

From this information, it is suggested that the flow interaction between the two devices involves a two-fold mechanism. First, it is suspected that without the fence, a center-rotating vortex (due to SLEE apex geometry) acts to diffuse the vortex being generated along the LE of the SLEE, but with the fence installed, this adverse vortex is unable to form and, thus a stronger vortex is generated from the SLEE apex. This situation is depicted in figure 46.

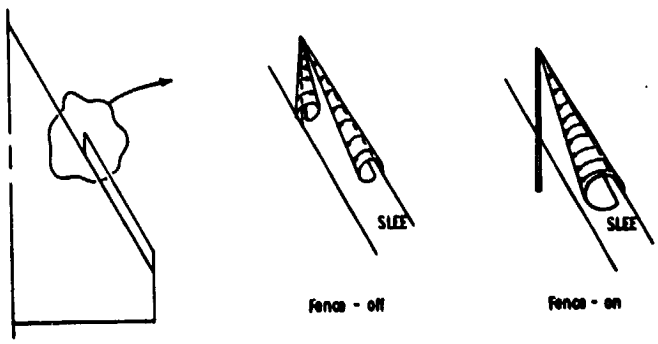

Figure 46.- Illustrations of suggested SLEE apex flow mechanism.

The second mechanism is manifested in the shielding effect of the fence downstream along the wing LE, i.e., once the primary vortex is formed upstream of the fence (approximately 16° α), it is forced inboard allowing the SLEE vortex to maintain effectiveness along the LE to higher angles of attack.

This effect is also reflected in the balance data (fig. 45(b)). Prior to 12° angle of attack, there is close agreement for the fence on and off cases; however, at higher angles, the fence-on data show less lift and drag (C_N and C_A) which implies that the vortex is acting primarily on the LE, and not on the upper surface of the wing. The C_m data indicated no pitch-up mode for the fence-on configuration and also a reduction in the severity of the pitch-down beyond 10° α.

To summarize, by positioning the fence at the SLEE apex, additional drag reduction was achieved as the result of the interaction of the SLEE fence flow mechanisms. The fact that this effect did not take place until the primary vortex system approached $\eta = 0.25$ (position of the fence), suggests that better results could be gained by positioning a second fence at $\eta = 0.50$, i.e., drag reduction should develop at a lower α. The success of this limited evaluation suggests that increased levels of LE thrust might be possible by combining the SLEE with the other devices tested, and perhaps, spanwise blowing.

6.7.2 Slots with VG

6.7.2.1 Performance and flow mechanisms.- In Section 6.4, it was shown that the slot devices on the thick wing had good drag-reduction performance up to approximately 19° angle of attack, at which point LE separation occurred outboard of the 50 percent semispan position. This

resulted in longitudinal instability and, therefore, was considered a limiting characteristic for the multi-slot configuration. The cause of this problem was thought to be flow separation in the outboard region of the wing - which suggested the use of the pylon-type VG. It will be shown in the following paragraphs that the individual shortcomings of the slots and VG are alleviated when used in combination, i.e., through the interaction of the individual flow mechanisms.

Figure 47 presents the data for: (1) four slots at η = 0.25, 0.375, 0.50, and 0.75 in combination with the VG4 at η = 0.625 (circle symbol); (2) the VG4 at η = 0.625 (square symbol); and (3) five slots (diamond symbol). The influence of the slot just inboard of the VG can be noted in the C_p distributions at η = 0.57 where the stalled flow condition for the "VG only" case (square symbol) has been delayed to approximately 21° angle of attack. This would indicate that the vortex emanating from the upstream slot (at η = 0.50) has created sufficient downwash to alleviate the early LE separation inboard of the VG and thus, additional thrust is developed.

At η = 0.70, a comparison of the C_p distributions for the slots with and without the VG (circle and diamond symbols, respectively) indicates that the presence of the VG degrades the thrust up to approximately 18° α (fig. 47(a)). This can also be noted in the C_T versus η distribution and in the C_T versus α distribution in figure 47(b), but at 21° angle of attack and above, the slot VG configuration develops significantly high thrust levels at the two outboard pressure stations. It is believed that the VG induced vortex positioned on the upper surface of the wing establishes a barrier to the spanwise flow and

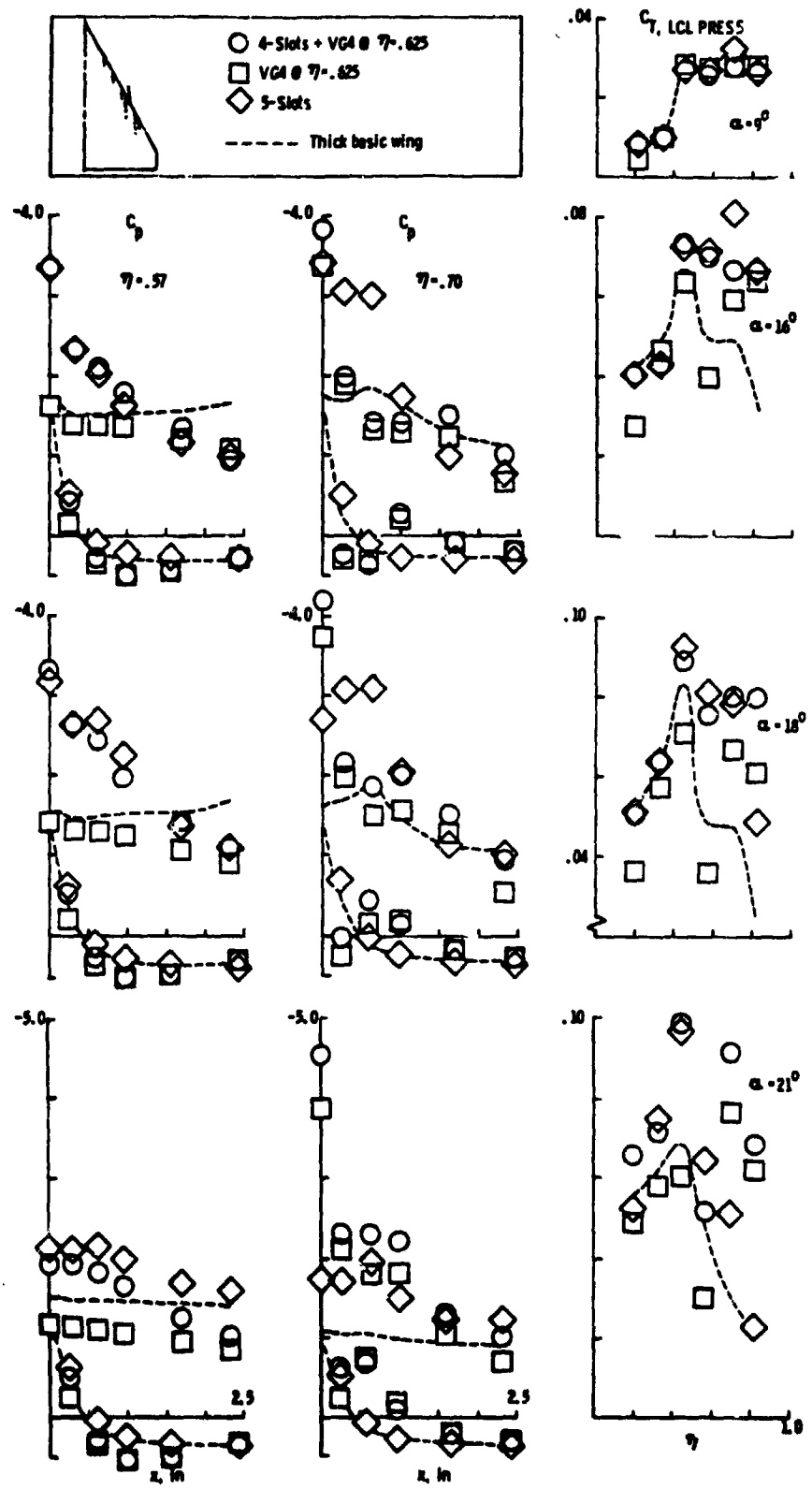

Figure 47(a).- Comparison of balance and pressure data obtained from the thick wing for three configurations: slot-VG, VG only, and slots only.

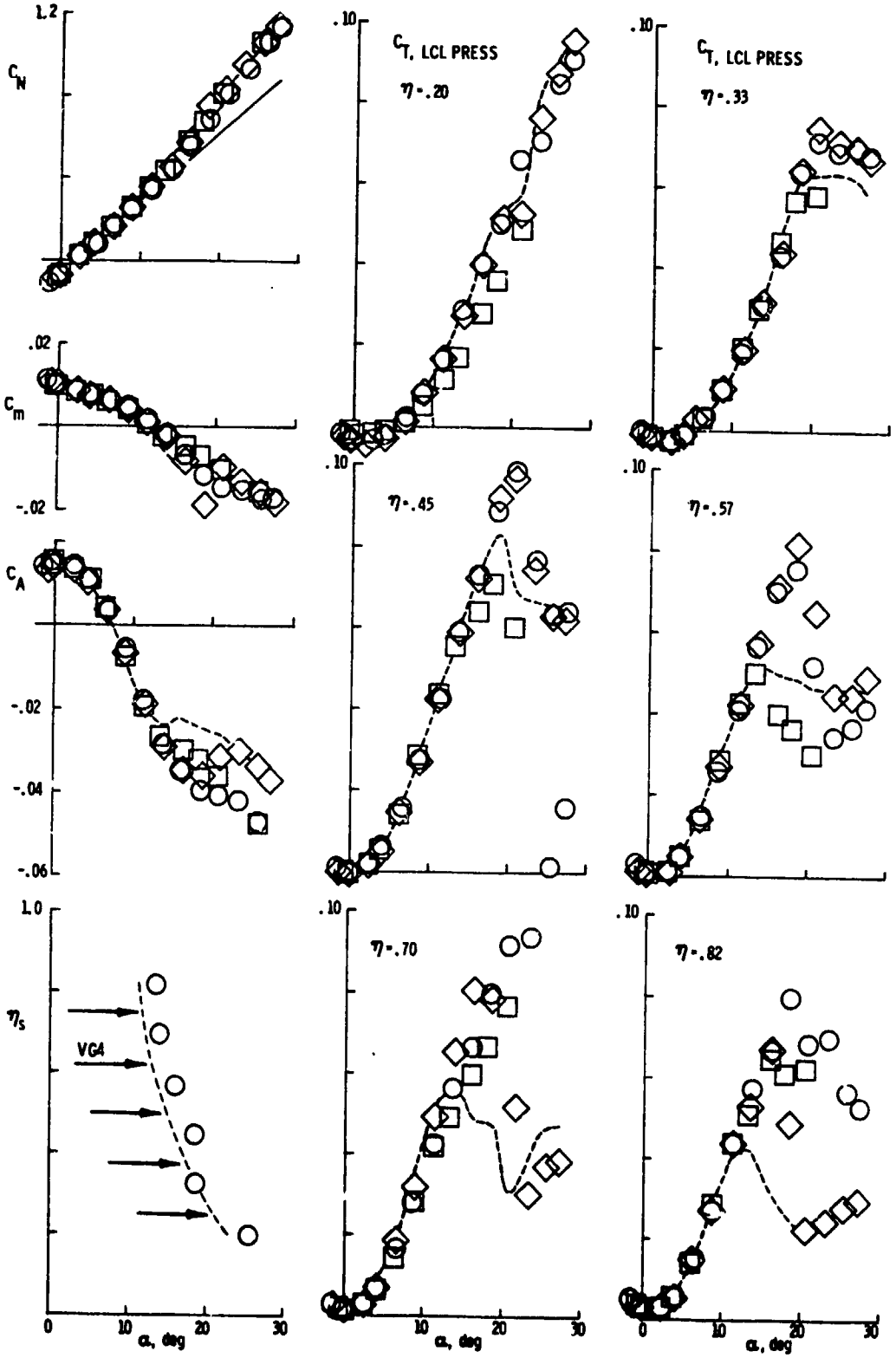

Figure 47(b).- Concluded.

thus, isolates the outboard portion of the wing from the influence of the inboard primary vortex. A comparison of the oil flow visualization picture in figure 48 (slots with VG) and in figure 31 (without the VG) supports this contention. This interaction of the flow mechanisms allows the outboard slots to remain effective, and in combination with the VG, the flow near the wing tip remains attached as opposed to the "slots alone" case where the flow becomes stalled.

The balance data in figure 47(b) also show this effect by the elimination of pitch-up at approximately 19° angle of attack (C_m vs α), i.e., the addition of the pylon-type VG has improved the longitudinal stability of the configuration. Also, the thrust gains beyond 19° α are confirmed in the C_A graph (circle versus diamond symbols), and consequently, the C_N data indicate a slight loss at the higher angles - as would be expected. The η_s versus α graph indicates that this combination of devices causes a slight delay in LE separation which does not really reflect the flow situation in the tip region, viz., beyond the 82 percent semispan position.

The conclusions of this test are that the "slots VG" configuration did improve the longitudinal stability as well as the drag-reduction performance. This was achieved through the interaction of the device flow mechanisms and the primary vortex system. Because of the success and limited scope of this test, it is suggested that an investigation of slots be conducted in combination with VG located at η = 0.50 and then two VGs at η = 0.375 and 0.625. In addition, the relative position of the slot upstream of the VG may very well have a strong impact on the effectiveness of the VG.

Figure 48.- Oil flow visualization picture of thick wing in the slots - VG configuration.

6.8 SUMMARY OF PERFORMANCE

This analysis will now be concluded with a summary of the best performing configuration within a family of devices. The parameters selected for this comparison are the lift coefficient (C_L), the lift-drag ratio (L/D), and the suction parameter (s), all plotted versus angle of attack.

At the top of figure 49, the C_L data show close agreement for all of the devices below $\alpha_D \approx 8^o$ - note that (1) the SLEE data have been area corrected, and (2) the solid line is an extension of the linear portion of the curve which represents attached flow. Beyond 8^o α, the devices show a more gradual increase in lift than the basic wing (dashed line) which is the result of the devices modifying the LE flow, i.e., the devices establish more LE thrust in lieu of additional vortex lift. To gain a better appreciation of the effectiveness of these devices, the characteristics at a C_L of 0.50 have been selected for discussion.

In figure 49, the C_L versus α plot indicates that the devices require approximately 1^o more α to generate the same lift, but dropping vertically, the other two graphs show a 12 percent increase in L/D and a 44 percent increase in suction (slightly less for the VG). At the higher angles of attack, the data tend to merge, with the SLEE showing a slightly higher suction level. It can be stated from this information that in the α range of interest, the drag-reduction potential of these devices are real and can be achieved without significant losses in lift.

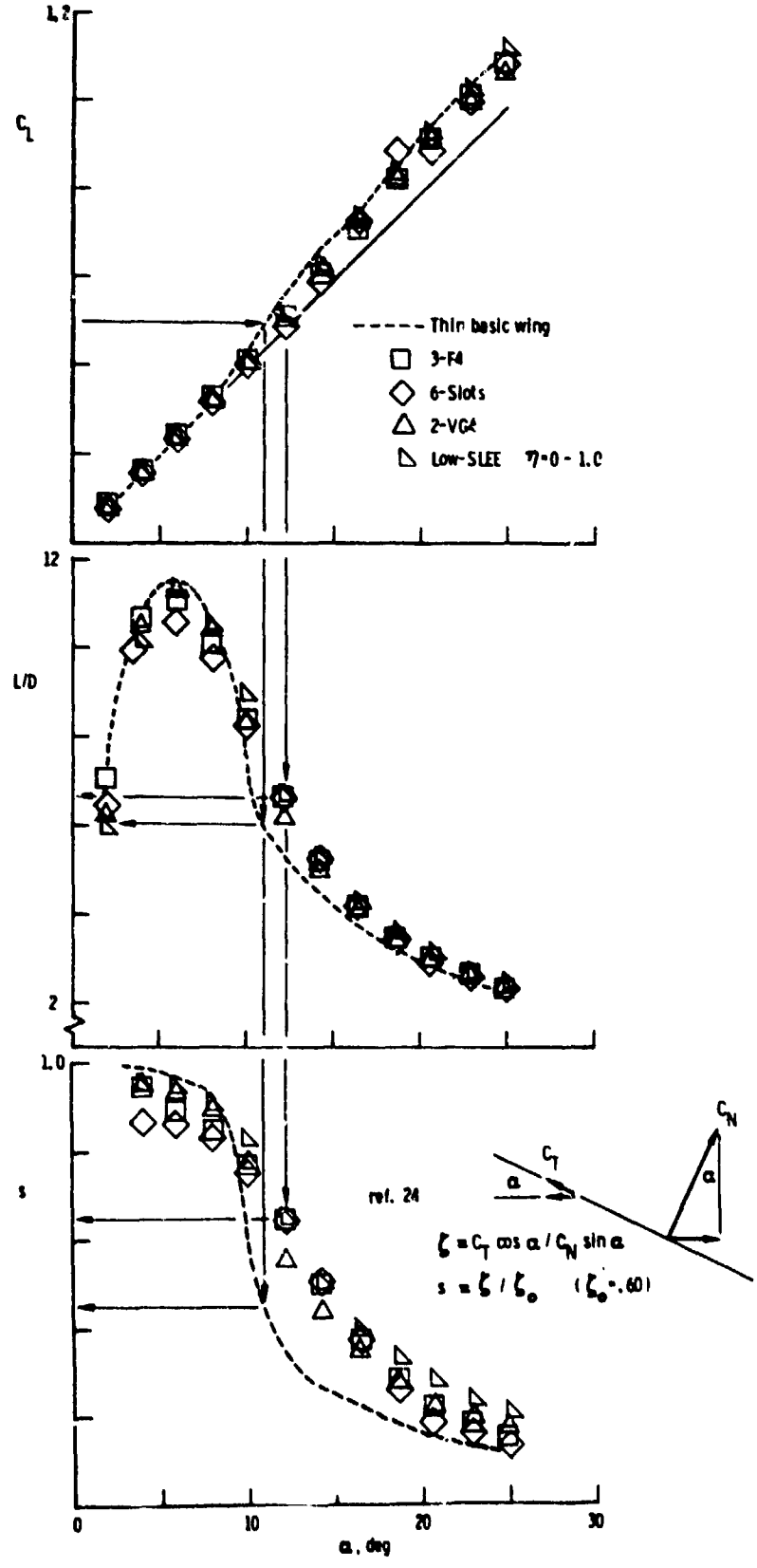

Figure 49.- Comparison of best performing configuration within a family of devices.

VII. CONCLUSIONS AND RECOMMENDATIONS

The findings of this experimental investigation are based on analyses of force and pressure measurements taken at low speed on a 60° cropped delta model in the Langley 7- by 10-foot high-speed tunnel. The purpose of this research was to evaluate the drag-reduction effectiveness of four types of devices in controlling LE flow at moderate to high angles of attack. The application of this research would be to enhance the maneuverability of high performance tactical aircraft. The results of this study indicate that the devices tested are able to favorably manipulate the flow at the wing LE and, as a consequence, will provide significant reduction in drag - as well as improving pitching-moment characteristics at higher angles of attack. It is believed that the data base established and the conclusions/recommendations reached will be a useful starting point for those aerodynamicists concerned with the problem of drag reduction for highly swept wings at high α.

7.1 GENERAL

This investigation has demonstrated that multiple arrangements of slots, fences, and pylon-type VGs were effective in delaying LE separation by compartmentation of wing LE, thus allowing discrete vortices (acting on the blunt LE) to generate aerodynamic thrust to high angles of attack. The SLEE, on the other hand, generated aerodynamic thrust by forcing LE separation that resulted in the formation of a coiled vortex just ahead of the wing LE. All four types of devices had several similar characteristics with respect to the basic wing: the onset of vortex lift was delayed; a small amount of lift was lost when significant drag reduction was achieved; drag reduction occurred following the formation of the primary vortex system; pitch-up was either alleviated or eliminated; and cruise drag was increased. Also, better drag-reduction performance was obtained on the thin wing which had earlier LE flow separation and a subsequent greater loss of LE suction, as compared with the thick wing.

7.2 FENCES

Analysis of the fence data indicated that height had relatively little effect on drag-reduction performance, and that fences flush with the LE performed better than those projecting forward. In addition, drag reduction was improved progressively by increasing the number of fences.

Further studies toward minimizing/tapering fence height, reducing the length of the fence on the underside of the wing, and optimizing fence spacing in multiple arrangements, should prove worthwhile. From this, it is thought that the cruise-drag penalty may be alleviated along with better high α performance.

7.3 SLOTS

This investigation showed that multiple chordwise slots effectively delayed LE separation by compartmentation of the wing LE; however, their effectiveness terminated rather suddenly causing a simultaneous abrupt increase in drag and strong pitch-down - followed by a severe pitch-up. Recall that this longitudinal instability was eliminated when one of the slots was fitted with a VG.

It is believed that the full drag-reduction potential of the slot can be gained by varying the slot geometry (i.e., width and length), determining the optimum spanwise spacing between multiple slots, and aligning the slot with the oncoming flow. Further the low α drag penalty, which is thought to arise from the positive pressure acting at the rear of the slot, may be relieved by internal contouring of the slot as shown in figure 50.

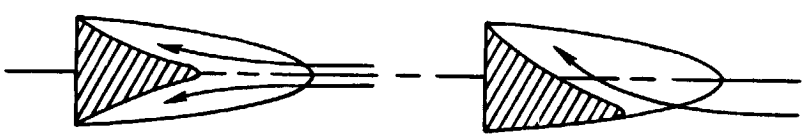

Figure 50.- Illustration of possible ways to internally contour slot to reduce low α drag.

An alternate solution would be to seal the slots during cruise flight.

It should be added that the slot offers the advantages of simple design and easy retrofit for existing airframes, e.g., F-106 aircraft.

7.4 PYLON-TYPE VORTEX GENERATORS (VG)

From the family of VGs, this study revealed that one set of 30° swept VGs with 10° of toe-in provided the best overall drag-reduction performance when positioned near the mid-semispan of the wing. Also, two sets of VGs increased performance at the higher angles of attack, but at the expense of increased low α drag. It is believed that the application of this concept would be quite attractive if the VGs also served as pylons for air-to-air and/or air-to-ground weapons - where the additional cruise drag created by the VGs would be inconsequential in comparison to the drag of the weapons.

It is believed that there is ample justification for further evaluation of the VG concept. Of primary interest would be reduction in size, spacing, and variable toe-in angle of multiple VGs, and the effect of wing sweep angle on VG performance. Also, data have been presented that showed that a slot inboard of the VG improved drag reduction by delaying inboard separation, and therefore, the slot VG combination should be investigated.

7.5 SHARP LEADING-EDGE EXTENSIONS (SLEE)

The SLEE was found to have little capability in the mid-position; however, in the low position, the half semispan SLEE showed significant drag-reduction performance which was increased by either extending the SLEE to full semispan or by adding an inboard fence at $\eta = 0.50$. At the higher angles of attack, the drag-reduction effectiveness of the SLEE diminished as the result of the vortex moving off the SLEE onto the wing upper surface. Also, the SLEE exhibited increased low α drag as was the case with the other devices in multiple arrangements.

It is firmly believed that the SLEE concept has extensive drag-reduction potential that warrants further investigation. The principal research effort should be toward developing ways of maintaining the vortex in front of the LE to higher angles of attack. Possible methods would include: tapering/twisting the SLEE; segmenting the SLEE with fences or slots; and selective spanwise blowing on the SLEE; or combinations of the foregoing. Further, it is felt that to fully exploit the potential of the SLEE, it should be developed as a retractable device to eliminate cruise drag.

7.6 CONCLUDING REMARKS

Since this research was conducted on a 60° flat plate model, it is recommended that future investigations use scale models of real configurations so that the effects of wing sweep and camber can be evaluated. It is thought that cambered/twisted wings may reduce the effectiveness of the devices which could be inferred to mean that the problems of designing and constructing this type of wing might not be necessary, viz., the performance of a simple flat plate wing with devices might perform as well as a more complicated wing. Also, tests should be run using realistic Mach numbers and sideslip angles.

Lastly, from unreported data collected during this study, there are strong indications that the devices tested will have a favorable effect on lateral stability and control characteristics; therefore, it is recommended that future research also include lateral characteristics.

VIII. REFERENCES

1. Hallion, R. P.; Lippisch, Gluhareff; and Jones: The Emergence of the Delta Planform and The Origins of the Sweptwing In the United States. Aerospace Historian, 1979.

2. Wilson, H. A., Jr.; and Lovell, J. C.: Full-Scale Investigation of the Maximum Lift and Flow Characteristics of an Airplane Having Approximately Triangular Plan Form. NACA RM L6K20, 1946.

3. Lovell, J. C.; and Wilson, H. A., Jr.: Langley Full-Scale Tunnel Investigation of Maximum Lift and Stability Characteristics of an Airplane Having Approximately Triangular Plan Form (DM-1 Glider). NACA RM L7F16, 1947.

4. Jones, R. T.: Properties of Low-Aspect-Ratio Pointed Wings at Speeds Below and Above the Speed of Sound. NACA Rep. 835, 1945.

5. Osborne, R. S.; and Wornom, D. E.: Aerodynamic Characteristics Including Effects of Wing Fixes of a 1/20-Scale Model of the Convair F-102 Airplane at Transonic Speeds. NACA RM SL54C23, 1954.

6. Osborne, R. S.: Effects of Wing Modifications on the Longitudinal Stability Characteristics of a 0.04956-Scale Model of the Convair F-102A Airplane at Transonic Speeds. NACA RM SL56J30a, 1956.

7. Keener, E. R.: Pressure Measurements Obtained in Flight at Transonic Speeds For a Conically Cambered Delta Wing. NASA TM X-48, 1959.

8. Harris, C. D.; and Bartlett, D. W.: Wind-Tunnel Investigation of Effects of Underwing Leading-Edge Vortex Generators on a Supercritical-Wing Research Airplane Configuration. NASA TM X-2471, 1972.

9. Bartlett, D. W.; and Harris, C. D.: Wind-Tunnel Development of Underwing Leading-Edge Vortex Generators on an NASA Supercritical-Wing Research Airplane Configuration. NASA TM X-2808, 1973.

10. Ridder, S.: On the Induced Drag of Thin Plane Delta Wings. An Experimental Study of the Spanwise Distribution of the Leading-Edge Forces at Low Speeds. KTH-AERO TN 57, Royal Institute of Technology (Stockholm), 1971.

11. Shevell, R. S.; and Schaufele, R. D.: Aerodynamic Design Features of the DC-9. J. Aircraft, vol. 3, no. 6, 1966.

12. Weil, J.; and Morrison, W. D., Jr.: A Study of the Use of Leading-Edge Notches as a Means for Improving the Low-Speed Pitching-Moment Characteristics of a Thin 45° Swept Wing of Aspect Ratio 4. NACA RM L53J27a, 1953.

13. Rao, D. M.; and Johnson, T. D., Jr.. Subsonic Wind-Tunnel Investigation of Leading-Edge Devices on Delta Wings (Data Report). NASA CR-159120, 1979.

14. Taylor, R. T.: Boundary Layer Transition Strips in Atmospheric Tunnels. NASA Memorandum, 1967.

15. Fox, C. H., Jr.; and Huffman, J. K.: Calibration and Test Capabilities of the Langley 7- by 10-Foot High Speed Tunnel. NASA TM X-74027, 1977.

16. Fox, C. H., Jr.: Real Time Data Reduction Capabilities at the Langley 7- by 10-Foot High Speed Tunnel. NASA TM 78801, 1980.

17. Crowder, J. P.: Fluorescent Mini-Tufts for Non-Intrusive Flow Visualization. McDonnell-Douglas Corp. Rep. MDC J7374, 1977.

18. Herriot, J. G.: Blockage Corrections for Three-Dimensional-Flow Closed-Throat Wind Tunnels, With Consideration of the Effect of Compressibility. NACA Rep. 995, 1950. (Supersedes NACA RM A7B28.)

19. Gillis, C. L.; Polhamus, E. C.; and Gray, J. L., Jr.: Charts for Determining Jet-Boundary Corrections for Complete Models in 7- by 10-Foot Closed Rectangular Wing Tunnels. NACA NR L-123, 1945. (Formerly NACA ARR L5G31.)

20. Bartlett, G. E.; and Vidal, P. J.: Experimental Investigation of Influence of Edge Shape on the Aerodynamic Characteristics of Low Aspect Ratio Wings at Low Speed. J. of the Aeronautical Society, vol. 22, no. 8, 1955.

21. Mirande, J., Schmitt, V.; and Werle, H.: Vortex Pattern Developing on the Upper Surface of a Swept Wing at High Angles of Attack. NASA TM 75377, 1979.

22. Henderson, W. P.: Effects of Wing Leading-Edge Radius and Reynolds Number on Longitudinal Aerodynamic Characteristics of Highly Swept Wing-Body Configurations at Subsonic Speeds. NASA TN D-8361, 1979.

23. Mehrotra, S. C.; and Lan, C.: A Theoretical Investigation of the Aerodynamics of Low-Aspect-Ratio Wings with Partial Leading-Edge Separation. NASA CR-145304, 1978.

24. Carlson, W. C.; and Mack, R. J.: Estimation of Leading-Edge Thrust for Supersonic Wings of Arbitrary Planform. NASA TP 1270, 1978.